



TEZ ŞABLONU ONAY FORMU
THESIS TEMPLATE CONFIRMATION FORM

1. Şablonda verilen yerleşim ve boşluklar değiştirilmemelidir.
2. **Jüri tarihi** Başlık Sayfası, İmza Sayfası, Abstract ve Öz'de ilgili yerlere yazılmalıdır.
3. İmza sayfasında jüri üyelerinin unvanları doğru olarak yazılmalıdır. Tüm imzalar **mavi pilot kalemle** atılmalıdır.
4. **Disiplinlerarası** programlarda görevlendirilen öğretim üyeleri için jüri üyeleri kısmında tam zamanlı olarak çalıştıkları anabilim dalı başkanlığının ismi yazılmalıdır. Örneğin: bir öğretim üyesi Biyoteknoloji programında görev yapıyor ve biyoloji bölümünde tam zamanlı çalışıyorsa, İmza sayfasına biyoloji bölümü yazılmalıdır. İstisnai olarak, disiplinler arası program başkanı ve tez danışmanı için disiplinlerarası program adı yazılmalıdır.
5. Tezin **son sayfasının sayfa** numarası Abstract ve Öz'de ilgili yerlere yazılmalıdır.
6. Bütün chapterlar, referanslar, ekler ve CV sağ sayfada başlamalıdır. Bunun için **kesmeler** kullanılmıştır. **Kesmelerin kayması** fazladan boş sayfaların oluşmasına sebep olabilir. Bu gibi durumlarda paragraf (¶) işaretine tıklayarak kesmeleri görünür hale getirin ve yerlerini **kontrol edin**.
7. Figürler ve tablolar kenar boşluklarına taşmamalıdır.
8. Şablonda yorum olarak eklenen uyarılar dikkatle okunmalı ve uygulanmalıdır.
9. Tez yazdırılmadan önce PDF olarak kaydedilmelidir. Şablonda yorum olarak eklenen uyarılar PDF dokümanında yer almamalıdır.
10. **Bu form aracılığıyla oluşturulan PDF dosyası arkalı-önlü baskı alınarak tek bir spiralli cilt haline getirilmelidir.**
11. Spiralli hale getirilen tez taslağınızdaki ilgili alanları imzalandıktan sonra, [Tez Jüri Atama Formu](#) ile birlikte bölüm sekreterliğine teslim edilmelidir.
12. Tez taslaklarının kontrol işlemleri tamamlandığında, bu durum öğrencilere METU uzantılı öğrenci e-posta adresleri aracılığıyla duyurulacaktır.
13. Tez yazım süreci ile ilgili herhangi bir sıkıntı yaşarsanız, [Sıkça Sorulan Sorular \(SSS\)](#) sayfamızı ziyaret ederek yaşadığınız sıkıntıyla ilgili bir çözüm bulabilirsiniz.
1. Do not change the spacing and placement in the template.
2. Write **defense date** to the related places given on Title page, Approval page, Abstract and Öz.
3. Write the titles of the examining committee members correctly on Approval Page. **Blue ink** must be used for all signatures.
4. For faculty members working in **interdisciplinary programs**, the name of the department that they work full-time should be written on the Approval page. For example, if a faculty member staffs in the biotechnology program and works full-time in the biology department, the department of biology should be written on the approval page. Exceptionally, for the interdisciplinary program chair and your thesis supervisor, the interdisciplinary program name should be written.
5. Write **the page number of the last page** in the related places given on Abstract and Öz pages.
6. All chapters, references, appendices and CV must be started on the right page. **Section Breaks** were used for this. **Change in the placement** of section breaks can result in extra blank pages. In such cases, make the section breaks visible by clicking paragraph (¶) mark and **check their position**.
7. All figures and tables must be given inside the page. Nothing must appear in the margins.
8. All the warnings given on the comments section through the thesis template must be read and applied.
9. Save your thesis as pdf and Disable all the comments before taking the printout.
10. **Print two-sided the PDF file that you have created through this form and make a single spiral bound.**
11. Once you have signed the relevant fields in your thesis draft that you spiraled, submit it to the department secretary together with your [Thesis Jury Assignment Form](#).
12. This will be announced to the students via their METU students e-mail addresses when the control of the thesis drafts has been completed.
13. If you have any problems with the thesis writing process, you may visit our [Frequently Asked Questions \(FAQ\)](#) page and find a solution to your problem.

Yukarıda bulunan tüm maddeleri okudum, anladım ve kabul ediyorum. / I have read, understand and accept all of the items above.

Name : _____
Surname : _____
E-Mail : _____
Date : _____
Signature : _____

ASSESSING THE PERFORMANCE OF A NOVEL HBV MODEL:
A COMPARATIVE ANALYSIS WITH EXISTING HBV-LIGHT MODEL AND
CLIMATE PROJECTIONS

A THESIS SUBMITTED TO
THE GRADUATE SCHOOL OF NATURAL AND APPLIED SCIENCES
OF
MIDDLE EAST TECHNICAL UNIVERSITY

BY

SENA YILMAZ

IN PARTIAL FULFILLMENT OF THE REQUIREMENTS
FOR
THE DEGREE OF MASTER OF SCIENCE
IN
CIVIL ENGINEERING

SEPTEMBER 2023

Approval of the thesis:

**ASSESSING THE PERFORMANCE OF A NOVEL HBV MODEL:
A COMPARATIVE ANALYSIS WITH EXISTING HBV-LIGHT MODEL
AND CLIMATE PROJECTIONS**

submitted by **SENA YILMAZ** in partial fulfillment of the requirements for the degree of **Master of Science in Civil Engineering, Middle East Technical University** by,

Prof. Dr. Halil Kalıpçılar
Dean, Graduate School of **Natural and Applied Sciences**

Prof. Dr. Erdem Canbay
Head of the Department, **Civil Engineering**

Assoc. Prof. Dr. M.Tuğrul YILMAZ
Supervisor, **Civil Engineering Dept., METU**

Examining Committee Members:

Prof. Dr. İsmail Yücel
Civil Engineering Dept., METU

Assoc. Prof. Dr. M.Tuğrul Yılmaz
Civil Engineering Dept., METU

Assoc. Prof. Dr. Ali Ercan
Civil Engineering Dept., METU

Assoc. Prof. Dr. Koray K.Yılmaz
Geological Engineering Dept., METU

Assoc. Prof. Dr. Sertaç Oruç
Civil Engineering Dept., ÇAKÜ

Date: 11.09.2023

I hereby declare that all information in this document has been obtained and presented in accordance with academic rules and ethical conduct. I also declare that, as required by these rules and conduct, I have fully cited and referenced all material and results that are not original to this work.

Name Last name : Sena Yılmaz

Signature :

ABSTRACT

ASSESSING THE PERFORMANCE OF A NOVEL HBV MODEL: A COMPARATIVE ANALYSIS WITH EXISTING HBV-LIGHT MODEL AND CLIMATE PROJECTIONS

Yılmaz, Sena
Master of Science, Civil Engineering
Supervisor: Assoc. Prof. Dr. M. Tuğrul Yılmaz

September 2023, 146 pages

Climate change and water resource investigations frequently use surface runoff as a key hydrometeorological metric. To meet these investigation objectives, an open-source hydrological model is necessary, where currently only a limited number of models are available. The main goal of this study is to create an open-source, new, and simple hydrological model called the HBV-R. To compare the performance of HBV-R, the benchmark model HBV-Light, which has no open-source code, is utilized. This study is performed over the Çoruh Basin of Türkiye, known for having significant hydropower potential. The HBV conceptual hydrological model is calibrated and validated using runoff observations from 30 different ground stations between 1980 and 2005. TRMM 3B42 and ERA5-Land precipitation data are used as forcing datasets in different simulations. To investigate the impact of climate change on the water resources potential of Çoruh Basin, precipitation and temperature projections originating from global climate model datasets HadGEM2-ES, MPI-ESM-MR, and GFDL-ESM2M under the RCP 4.5 and RCP 8.5 emission scenarios are used after being bias-corrected by QDM method. A comparative

analysis of HBV-Light and HBV-R models reveals mean NSE values of 0.51 and 0.61, respectively, validating daily simulations across thirty sub-basins. HBV-Light predicts a decline in surface runoff potential by approximately 3% (RCP 4.5) and 8% (RCP 8.5) from 2023 to 2098. Conversely, HBV-R projects an increase in surface runoff potential, estimating a rise of 20% (RCP 4.5) and 13% (RCP 8.5) during the same period. Results show the high potential of HBV-R in hydrological modeling and prediction.

Keywords: Climate Change, Surface Runoff, Çoruh Basin, HBV, Global Climate Model

ÖZ

YENİ BİR HBV MODELİNİN PERFORMANSININ DEĞERLENDİRİLMESİ: MEVCUT HBV-LIGHT MODELİ VE İKLİM PROJEKSİYONLARI İLE KARŞILAŞTIRMALI BİR ANALİZ

Yılmaz, Sena
Yüksek Lisans, İnşaat Mühendisliği
Tez Yöneticisi: Doç. Dr. M. Tuğrul Yılmaz

Eylül 2023, 146 sayfa

İklim değışikliği ve su kaynaklarının araştırılmasında yüzey akışı, önemli bir hidrometeorolojik ölçüt olarak sıkça kullanılır. Bu tür arařtırmaları gerçekleştirebilmek için açık kaynaklı bir hidrolojik model gereklidir, ancak řu anda sınırlı sayıda model bulunmaktadır. Bu çalışmanın temel amacı, HBV-R adında yeni ve basit bir açık kaynaklı hidrolojik model oluşturmaktır. Karşılaştırma amacıyla açık kaynaklı kod içermeyen referans model HBV-Light kullanılmıştır. Çalışma, büyük bir hidroelektrik potansiyele sahip olan Türkiye'nin Çoruh Havzası üzerinde gerçekleştirilmiştir. HBV kavramsal hidrolojik modeli, 1980 ile 2005 yılları arasında elde edilen 30 farklı yer istasyonundan alınan akış gözlemleri kullanılarak kalibre edilmiş ve doğrulanmıştır; farklı simülasyonlarda veri seti olarak TRMM 3B42 ve ERA5-Land yağış verileri kullanılmıştır. Çoruh Havzası'nın su kaynakları potansiyeline iklim değışikliğinin etkisini incelemek için, küresel iklim modeli veri setlerinden HadGEM2-ES, MPI-ESM-MR ve GFDL-ESM2M kaynaklı yağış ve sıcaklık projeksiyonları, QDM yöntemi ile yanlışlık düzeltilmesi yapıp RCP 4.5 ve RCP 8.5 emisyon senaryoları altında kullanılmıştır. HBV-Light ve HBV-R modellerinin karşılaştırmalı analizi sonuçları, sırasıyla 0.51 ve 0.61 olan ortalama

NSE deęerlerini gstermiř ve otuz alt havza boyunca gnlk simlasyonları doęrulamıřtır. HBV-Light, 2023 ile 2098 yılları arasında yzey akıřı potansiyelinde yaklaşık %3'lk bir azalma (RCP 4.5) ve %8'lik bir azalma (RCP 8.5) ngrrken; HBV-R, aynı dnemde yzey akıřı potansiyelinde %20'lik (RCP 4.5) ve %13'lk (RCP 8.5) bir artıř ngrmektedir. Sonular, HBV-R modelinin hidrolojik modelleme ve tahmin alanında yksek potansiyele sahip olduęunu gstermektedir.

Anahtar Kelimeler: İklım Deęiřiklięi, Yzey Suyu Akıřı, oruh Havzası, HBV, Kresel İklım Modeli

To my dear family,

ACKNOWLEDGMENTS

First and foremost, I am deeply indebted to my supervisor, Assoc. Prof. M. Tuğrul Yılmaz for his invaluable guidance, unwavering support, and insightful feedback. Their expertise and dedication have been instrumental in shaping this study.

I am also grateful to Dr. Süleyman Selim Çallı for the countless hours invested in developing and fine-tuning the code, which forms the backbone of this thesis.

I would also like to acknowledge the State Hydraulic Works (DSİ) for providing the necessary resources, which played a significant role in completing this study.

Finally, I sincerely thank my family and friends for their unwavering support, understanding, and patience. Your love and encouragement have been my driving force, and I am truly grateful for everything you have done for me.

This research would not have been possible without the collective efforts of all those mentioned above, and I am sincerely thankful for their contributions.

This work is partially funded by the Scientific and Technological Research Council of Türkiye under grant number TÜBİTAK 121Y456.

TABLE OF CONTENTS

ABSTRACT.....	v
ÖZ.....	vii
ACKNOWLEDGMENTS	x
TABLE OF CONTENTS.....	xi
LIST OF TABLES	xiv
LIST OF FIGURES	xv
LIST OF ABBREVIATIONS	xvii
CHAPTERS	
1 INTRODUCTION	1
2 LITERATURE REVIEW	5
2.1 Modelling Studies	5
2.1.1 Hydrological Models	5
2.1.2 Hydrological Modeling Studies in Türkiye	9
2.2 Climate Change	13
2.2.1 General Circulation Models (GCMs).....	15
2.2.2 Climate Change Effects on Water Resources	19
2.2.3 Climate Change in Türkiye	23
2.2.4 Climate Change in Çoruh Basin	31
3 STUDY AREA AND METHODOLOGY.....	33
3.1 Çoruh Basin.....	33
3.1.1 General Information About Çoruh Basin.....	33
3.1.2 Climate of Çoruh Basin	38

3.1.3	Sub-basins in Çoruh Basin	41
3.2	Datasets	43
3.2.1	Ground-Based Meteorological Stations	44
3.2.2	Runoff Observations.....	45
3.2.3	ERA5-Land.....	46
3.2.4	Climate Change Datasets (GCM).....	49
3.2.5	TRMM 3B42	49
3.2.6	Potential Evaporation	50
3.3	Bias Correction	51
3.4	The HBV Model	53
3.5	HBV-Light and HBV-R Models.....	61
3.5.1	HBV-Light Model	61
3.5.2	HBV-R Model	62
3.5.3	HBV-Light and HBV-R Parameters.....	63
3.6	Model Calibration and Validation	64
3.6.1	HBV-Light Calibration.....	65
3.6.2	HBV-R Calibration.....	67
3.7	Used Statistics.....	68
4	RESULTS AND DISCUSSION.....	71
4.1	Analysis of Dataset and Bias Correction	71
4.2	Analysis of Precipitation and Temperature	73
4.3	Historical Period Simulations of HBV Models	76
4.4	Future Projections of HBV Models	87
5	CONCLUSIONS AND RECOMMENDATIONS.....	95

REFERENCES	97
APPENDICES	111
A. Parameters of The Trained HBV Models.....	111
B. ERA5-Land Training and Validation with HBV-R and HBV-Light	116
C. GCM Training and Validation	124
D. TRMM 3B42 Validation	132
E. GCM Annual Future Graphs	139

LIST OF TABLES

TABLES

Table 2-1 Characteristics of the Models (Devia et al., 2015).....	6
Table 3-1 Dams In Çoruh Basin.....	36
Table 3-2 Meteorological Stations Used in Analysis	45
Table 3-3 Information About the Used Data in the Research	50
Table 3-4 Parameters of HBV-R and HBV-Light Model	63
Table 3-5 Calibration and Validation Periods for each Sub-Basin	65
Table 4-1 Annual Averages of The Temperature (°C)	74
Table 4-2 Annual Averages of The Precipitation (mm/year)	75
Table 4-3 Comparison of the Dataset with Other Study	76
Table 4-4 Calibration Statistics for HBV-Light and HBV-R Model for ERA5-Land	77
Table 4-5 Calibration Statistics for HBV-Light Model for GCMs	78
Table 4-6 Validation Statistics for HBV-Light and HBV-R Model for ERA5-Land	79
Table 4-7 Validation Statistics for HBV-Light Model for GCM	80
Table 4-8 Validation Statistics for HBV-LIGHT and HBV-R Model for TRMM3B42	82
Table 4-9 NSE Values of The Historical Datasets	83
Table 4-10 Historical and Future Projected Mean Runoff Values with HBV-R Model.....	88
Table 4-11 Historical and Future Projected Mean Runoff Values with HBV-Light Model.....	89

LIST OF FIGURES

FIGURES

Figure 2-1 Global Analysis Annual Mean River Flow Trends across Regions From 7250 Observatories (1971–2010) (Gudmundsson et al., 2021)	14
Figure 2-2 Schematic Structure of MPI-ESM Model (Cotronei & Slawig, 2020) .	16
Figure 2-3 CO2 emissions (top-left), concentrations (top-right), anthropogenic radiative forcing (bottom-left), and global mean temperature (bottom-right) for the 21st-century scenarios in the Scenario (O’Neill et al., 2016)	18
Figure 2-4 Alteration in the occurrence frequency of 100-year floods.....	21
Figure 2-5 Shift in the frequency of 100-year drought events.....	22
Figure 2-6 Alteration in the intensity of 100-year droughts (Lehner et al., 2006)..	22
Figure 2-7 Variation in seasons across 10-year intervals for average temperature anomaly values in the HadGEM2-ES Model under the RCP 4.5 scenario (SYGM, 2016)	29
Figure 2-8 Seasonal variation of 10-year intervals for total precipitation anomaly values in the HadGEM2-ES Model under the RCP 4.5 scenario (SYGM, 2016) ..	30
Figure 3-1 Location of the Çoruh Basin	34
Figure 3-2 Çoruh Basin Cities and Districts	34
Figure 3-3 The Topography and The Dams of the Çoruh Basin	35
Figure 3-4 Hypsometric Curve of Çoruh Basin	37
Figure 3-5 The Çoruh Basin Meteorological Observation Stations and Isohyetal (Equal Rainfall) Curves (SYGM, 2020)	40
Figure 3-6 Some of the sub-basins in Çoruh	41
Figure 3-7 Sub-Basins in Çoruh	42
Figure 3-8 Flow Chart.....	44
Figure 3-9 Map of Meteorological Stations.....	45
Figure 3-10 The Runoff Observation Stations and The Dams.....	46
Figure 3-11 Çoruh Basin's 31-Year Average Temperature (Top) and Precipitation (Bottom) Distribution from ERA5-Land	48

Figure 3-12 General Structure of HBV Model (Seibert, 2000).....	55
Figure 3-13 Soil Routine Graphs of the HBV Model (Seibert, 2005).....	57
Figure 3-14 Response Routine of the HBV Model (Seibert, 2005)	59
Figure 3-15 Routing Routine of the HBV Model (Seibert, 2005).....	60
Figure 3-16 HBV-Light Graphical User Interface	61
Figure 3-17 HBV-Light GAP Optimization Interface.....	66
Figure 4-1 Annual Temperature Graph of the Dataset	72
Figure 4-2 Graph of Annual Bias Corrected Temperature Data	72
Figure 4-3 Annual Precipitation Graph of the Dataset	73
Figure 4-4 Graph of Annual Bias Corrected Precipitation Data	73
Figure 4-5 E23A022 Sub-Basin Training Period	85
Figure 4-6 E23A022 Sub-Basin Validation Period	86
Figure 4-7 E23A022 Sub-Basin Interquantile Graph of Runoff	87
Figure 4-8 E23A022 Sub-Basin Future Surface Runoff Projections with HBV-R Model.....	90
Figure 4-9 E23A022 Sub-Basin Annual Surface Runoff Projections with HBV-R Model.....	91
Figure 4-10 E23A022 Sub-Basin Future Surface Runoff Projections with HBV- Light Model	92
Figure 4-11 E23A022 Sub-Basin Annual Surface Runoff Projections with HBV- Light Model	93

LIST OF ABBREVIATIONS

ABBREVIATIONS

ANN	Artificial Neural Network
ArcGIS	Geographic Information System
CERES	Clouds and the Earth's Radiant Energy System
CMIP	Coupled Model Intercomparison Project
CNRM-CM5	Centre National de Recherches Météorologiques - Climate Model version 5
CORDEX	Coordinated Regional Downscaling Experiments
CWH	Capillary Water Holding Capacity
DQM	Detrended Quantile Mapping
DSİ	Devlet Su İşleri (State Hydraulic Works)
ECMWF	European Centre for Medium-Range Weather Forecasts
ECHAM4	European Center Hamburg Model version 4
ECHAM6	European Center Hamburg Model version 6
ERA5	ECMWF Reanalysis 5
GAP	Genetic Algorithm and Powell
GCM	General Circulation Model
GFDL	Geophysical Fluid Dynamics Laboratory
GLDAS	Global Land Data Assimilation System
GWSA	Groundwater Storage Anomalies
GSAT	Global Surface Air Temperature
GSMaP	Global Satellite Mapping of Precipitation
GR4J	Hydrological daily rainfall-runoff model
GRACE	Gravity Recovery and Climate Experiment
HadCM3	Hadley Centre Climate Model version 3
HadGEM2-ES	Hadley Centre Global Environment Model version 2 - Earth System

HBV	Hydrologiska Byråns Vattenbalansavdelning
HEC-HMS	Hydrologic Engineering Center's Hydrologic Modeling System
IPCC	Intergovernmental Panel on Climate Change
JAXA	Japan Aerospace Exploration Agency
JSBACH	Jena Scheme for Biosphere-Atmosphere Coupling in Hamburg
LHS	Latin Hypercube Sampling
LIS	Land Information System
MCS	Monte Carlo Sampling
MGI	Meteoroloji Gözlem İstasyonları (Meteorological Observation Stations)
MGM	Meteoroloji Genel Müdürlüğü (Turkish State Meteorological Service)
MIKE SHE	Systeme Hydrologique European
MPI-ESM-MR	Max-Planck-Institute Earth System Model - Medium Resolution
MPI-ESMLR	Max-Planck-Institute Earth System Model - Low Resolution - Dynamic Vegetation
MPI-ESM-P	Max-Planck-Institute Earth System Model - Low-Resolution Paleo Mode - Static Vegetation
MPIOM	Max-Planck-Institute Ocean Model
NASA	National Aeronautics and Space Administration
NOAA	National Oceanic and Atmospheric Administration
NSE	Nash-Sutcliffe Efficiency
PEST	Parameter Estimation Tool
PR	Passive Microwave Rainfall Retrieval
QDM	Quantile Delta Mapping
QM	Quantile Mapping
QMCS	Quasi-Monte Carlo Sampling

Qdiff	Difference between Observed and Simulated Streamflow
RCM	Regional Climate Model
RCP	Representative Concentration Pathways
RMSE	Root Mean Squared Error
SCE	Shuffled Complex Evolution
SLZ	Saturated Lower Zone
SRTM	Shuttle Radar Topography Mission
STREAM	Spatial Tools for the Reservoir and Environmental Assessment Modeling
SUZ	Saturated Upper Zone
SWECLIM	Snow and Water Equivalent Climate Model
SWAT	Soil and Water Assessment Tool
SYGM	State Hydraulic Works
TMI TRMM	Microwave Imager
TOPMODEL	Topography-Based Hydrological Model
TWSA	Terrestrial Water Storage Anomalies
TT	Threshold Temperature
VIC	Variable Infiltration Capacity
VIRS	Visible and Infrared Scanner

CHAPTER 1

INTRODUCTION

Climate change significantly affects runoff dynamics, which leads to drought and flood occurrences across Türkiye. These runoff-related events have far-reaching consequences, affecting multiple sectors. They impact water resources, disrupt infrastructure like dams, affect energy generation, and lead to pollution-related health issues. Furthermore, it contributes to economic losses, spurs unemployment, and triggers a decline in tourism due to flood-induced damages. Climate change can worsen flood events and soil erosion, escalating into soil pollution. The compounding effects of unplanned urbanization and inadequacies in infrastructure further amplify the consequences of floods. The repercussions span ecosystems, biodiversity, and cultural heritage. Comprehensive climate change investigations carry great importance in the pursuit of reducing and managing these multifaceted flood impacts.

At the core of the hydrological cycle, runoff plays a pivotal component, orchestrating the movement of water across the Earth's surface and significantly affecting the distribution of freshwater, ecosystems, and water supply. Various factors, including rainfall patterns, changes in land use, topographical characteristics, soil properties, vegetation cover, and human activities influence runoff. These factors collectively determine how water moves through landscapes, impacting streamflow and river discharge. However, human actions and the looming impact of climate change disrupt this complex cycle, leading to shifts in runoff patterns and presenting challenges for water resources management. In light of Türkiye's diverse geographical attributes, fluctuating climate dynamics, and escalating water demands, implementing a hydrological model becomes imperative to foster sustainable water management, enhance disaster resilience, and facilitate well-informed policymaking.

Hydrological models with atmospheric data such as temperature and precipitation can simulate runoff. Mainly in climate change studies, these types of simulations are essential. There are three types of hydrological models: empirical, conceptual, and physically based. Empirical models overlook important system details and are not easily applied to other catchments. Physically based models, on the other hand, are challenging to run because they require extensive data encompassing soil properties, land use, weather, topography, and more. However, conceptual models are comparatively more straightforward, but there is a limited selection of open-source options.

Even though there are several studies to investigate the runoff, there is not a simple yet powerful model that also has an open-source code. There is an insufficient of existing models' transferability in different climate conditions. Therefore, there is a need for an easy-to-apply and open-source conceptual model that can represent basins accurately. For the advancement of models, it is valuable for them to be open-source. The availability of open source gives model development opportunities and is essential in topics such as data assimilation. This aspect is relevant to climate change studies, as models play a pivotal role in forecasting and projecting future scenarios.

This study examines the effects of climate change on runoff using an open-source and conceptual hydrological model applied to approximately 30 sub-basins within the Çoruh Basin. The Çoruh Basin's steep gradients and rapid streamflow make it crucial for hydropower, necessitating accurate drought and flood predictions and early warning systems due to numerous hydroelectric power plants and dams. Also, the application of conceptual models in studies conducted over the Çoruh Basin has yet to be explored.

In addition, a comparative analysis is conducted between the HBV hydrological model and a newly developed simplified model, HBV-R, which employs fewer parameters. These two models are compared using ERA5-Land, a reanalysis dataset. Furthermore, TRMM 3B42, a satellite dataset, is used to assess its potential enhancements compared to a reanalysis dataset as input.

Additionally, to investigate climate change using the newly developed model, we have generated future predictions for two scenarios, representative concentration pathways (RCP) 4.5 and 8.5, using General Circulation Models (GCMs). These predictions have undergone bias correction through the quantile delta mapping method. Moreover, a comparison is done to evaluate the performance of the newly developed hydrological model against an existing model that needs more open-source code availability.

The thesis comprises five chapters. The first chapter clarifies the research objectives and underscores the significance of investigating surface runoff, climate change, and open-source codes. The second chapter comprehensively reviews relevant literature, encompassing definitions of hydrological models, globally employed models, and their applications in Türkiye. Additionally, the chapter examines the importance of climate change, both globally and within Türkiye. The third chapter delineates the dataset specifics and the methodologies employed in this research. The fourth chapter summarizes the analysis' findings and extensively reviews them. Finally, the fifth chapter encapsulates the primary conclusions and implications of the study, topping in a set of recommendations for future exploration.

CHAPTER 2

LITERATURE REVIEW

2.1 Modelling Studies

Water continuously circulates through the Earth's atmosphere, evaporating from seas, lakes, and plants, then cooling and condensing to return as precipitation, shaping the land and forming streams, lakes, and rivers (Inglezakis et al., 2016). The hydrological cycle comprises numerous interconnected components, and runoff links precipitation and stream flow. Surface runoff occurs when a portion of precipitation does not penetrate the soil and instead flows over the land surface, eventually reaching surface waters such as streams, rivers, lakes, or reservoirs (USGS, 2022.).

Surface runoff is employed in investigating broader environmental problems, addressing water quality and quantity issues, including flood forecasting, and studying ecological and biological interactions within aquatic environments (Kokkonen et al., 2001). Modeling surface runoff is vital in various aspects of water resources management, including analyzing catchment yields and responses, assessing water availability, monitoring changes over time, and generating future forecasts (Vaze & Banerjee, 2012).

2.1.1 Hydrological Models

Rainfall-runoff models are categorized into three main types: empirical models, conceptual models, and physics-based models (M. B. Beck, 1991). Empirical models (e.g., Young, 2020) are highly focused on observations and aim to characterize system response by extracting information from existing data without considering the specific structure of the hydrological system (Kokkonen et al., 2001). Conceptual models (e.g., Bergström, 1995) aim to describe critical hydrological processes using

simplified conceptualizations, resulting in a system of interconnected stores recharged and depleted by relevant hydrological cycle fluxes. On the other hand, the governing partial differential equations of physics-based models (e.g., Abbott et al., 1986) can be numerically solved using finite difference or finite element numerical methods by using classical continuum mechanics concepts (Kokkonen et al., 2001).

Table 2-1 Characteristics of the Models (Devia et al., 2015)

Empirical Model	Conceptual Model	Physically Based Model
Data based or metric or black box model	Parametric or grey box model	Mechanistic or white box model
Involve mathematical equations, derive value from available time series	Based on modeling of reservoirs and Include semi empirical equations with a physical basis	Based on spatial distribution, Evaluation of parameters describing physical characteristics
Little consideration of features and processes of system	Parameters are derived from field data and calibration	Require data about initial state of model and morphology of catchment
High predictive power, low explanatory depth	Simple and can be easily implemented in computer code	Complex model. Require human expertise and computation capability
Cannot be generated to other catchments	Require large hydrological meteorological data	Suffer from scale related problems
ANN, unit hydrograph	HBV model, TOPMODEL	SHE or MIKESHE model, SWAT, NOAH, VIC, Mosaic
Valid within the boundary of given domain	Calibration involves curve fitting make difficult physical interpretation	Valid for wide range of situations

As can be seen from the table, there are different types of models based on their structure. Some of the models that are used widely in research are the Soil and Water Assessment Tool (SWAT) model, Hydrologiska Byrans Vattenavdelning (HBV) model, Systeme Hydrologique European (MIKE SHE) model, HEC-HMS and Variable Infiltration Capacity Model (VIC).

Utilizing the MIKE SHE model necessitates comprehensive model data and physical parameters, which may not always be readily accessible, posing challenges during model setup (Devia et al., 2015). Furthermore, the model's code remains unmodifiable by users; however, it boasts a higher processing capacity than other models (Devia et al., 2015). A significant advantage lies in the extensive graphical functionalities for pre-processing and post-processing, facilitating a more convenient modeling process.

The HBV model, applied in Slovenia for flash flood cases, underwent calibration and validation using historical rainfall-runoff events. The results were satisfactory, with Nash-Sutcliffe coefficients ranging from 0.82 to 0.96 (Grillakis et al., 2010).

A study conducted in Tanzania analyzed a data-scarce, high-humidity tropical catchment using three different models: HEC-HMS, HBV, and ANN (Tibangayuka et al., 2022). The HEC-HMS model demonstrated superior performance with NSE and R² values of 0.80 and 0.82 for calibration and 0.84 and 0.79 for validation. The HBV model also showed suitability with NSE and R² values of 0.73 and 0.74 for calibration and 0.64 and 0.64 for validation. The ANN model performed satisfactorily with NSE and R² values of 0.66 and 0.67 for calibration and 0.55 and 0.52 for validation. These results offer essential insights for effective water resources management in the face of climate change impacts in the region.

In a different examined study, the authors introduce the Groundwater for Ungauged Basins (GrUB) module, a significant component in the simulation of low flows within physically based land surface models (LSMs) and conceptual rainfall-runoff models (HBV) (Tashie et al., 2022). GrUB, designed for calibration-free operation and reliant on widely available physically based data, demonstrates computational simplicity and adaptability across various LSMs and rainfall-runoff models. The study's evaluation, conducted in 84 United States watersheds by integrating GrUB into the popular HBV rainfall-runoff model, reveals noteworthy results. Notably, GrUB's performance in predicting low flows consistently matches or surpasses that of the calibrated HBV groundwater module. The study also explores the module's robustness, subjecting it to extreme scenarios, with GrUB exhibiting remarkable resilience, resulting in only minimal increases in error metrics. The findings strongly indicate GrUB's potential to enhance low flow predictions in LSMs and rainfall-runoff models, especially in situations with limited calibration data.

A study assessed runoff estimates from 10 macro-scale hydrological models using the WFDEI dataset and data from 966 catchments worldwide (H. E. Beck et al., 2017). Key findings include significant variations in model performance,

highlighting the importance of model choice in hydrological studies. Model-based runoff trends in medium-sized catchments showed poor agreement with observed trends, emphasizing the need for cautious interpretation. In regions dominated by rainfall, global hydrological models (GHMs) performed similarly to land surface models (LSMs), but GHMs outperformed LSMs in snow-dominated areas. Calibrated models performed better, and despite gauge-based adjustments, biases in precipitation data persisted, affecting runoff simulations. Multi-model ensembles showed only a slight decrease in performance compared to the best model, suggesting the potential benefits of multi-parameterization ensembles. Many models generated early spring snowmelt peaks, likely due to precipitation underestimation and the absence of certain processes. Overall, this study underscores the significance of model uncertainty in hydrological modeling and the need for improved precipitation data in semi-arid regions.

A study on the Rhine basin compares hydrological models HBV and VIC, finding that the semi-distributed conceptual HBV model outperforms the distributed land surface model VIC (Te Linde et al., 2008). The paper emphasizes the need for reliable hydrological models to understand climate change impacts on large rivers like the Rhine in Europe. It highlights that complex modeling does not necessarily yield better results, and meteorological forcing data significantly influences model performance. The importance of ground-based meteorological measurements is emphasized.

Another study conducted in Kenya compares three different models, SWAT, STREAM, and HBV, and evaluated the model performance using statistical criteria (NSE and R2) and visual assessment of hydrographs (Birundu & Mutua, 2017). The HBV Light model outperformed the SWAT and STREAM models in simulating the Nyangores and Amala Rivers hydrograph. However, the STREAM model had a higher R2 efficiency during calibration and validation than HBV. Overall, the results demonstrate the effectiveness of the HBV model in simulating observed flow compared to other models.

Also, a study by Bizuneh et al. (2021) indicates that SWAT and HBV models need improvements to capture daily hydrographs during high and low-intensity rainfall events accurately. Refinements, including seasonal-based evaluations, can enhance their representation of extreme runoff and rainfall conditions.

The models are extensively employed for the modeling of both gauged and ungauged catchments, playing a crucial role in flood forecasting, efficient water resource management, and the evaluation of various water-related aspects such as water quality, erosion, sedimentation, nutrient and pesticide circulation, land use, and climate change impacts, among others (Devia et al., 2015).

The selection of rainfall-runoff models should align with project objectives, data accessibility, study scope, required outputs, and desired simplicity (Sitterson et al., 2018). Physically distributed models offer detailed insights into the rainfall-runoff process, aiding effective water system management. However, the model choice may be restricted by data availability. Due to this, simpler models are frequently employed since detailed catchment characteristics are either unknown or entail high investigation costs (Rinsema, 2014).

2.1.2 Hydrological Modeling Studies in Türkiye

There are different hydrological modeling studies done over Türkiye. One of them is SYGM (2020b), a detailed research investigating climate change's effects on precipitation, temperature, and runoff all over Türkiye. Also, there are different studies investigate such as flash floods (Saber & Yilmaz, 2018), streamflow predictions (Çolak, 2017; Kazezyılmaz-Alhan et al., 2021; Kumanlioglu & Fistikoglu, 2019; Mesta et al., 2019) and snow recharge (Çallı et al., 2022).

Türkiye serves as a geographical bridge between its Eastern and Western regions. It has approximately 3% landmass in Europe (Thrace), with the remaining area situated on the Asian continent (Anatolia) (DSI, n.d.). The nation encompasses 25 distinct river basins. Many of its rivers originate within Turkish borders and flow into

domestic seas. Particularly noteworthy among these domestically draining rivers are Kızılırmak (1,151 km), Sakarya (824 km), Büyük Menderes (584 km), Seyhan (560 km), Yeşilirmak (519 km), Ceyhan (509 km), Gediz (275 km), and Küçük Menderes (129 km) (DSI, n.d.). Conversely, Türkiye's rivers that begin within its territory but flow into seas bordering other countries include the Euphrates (1,263 km within Türkiye), Tigris (512 km within Türkiye), Çoruh (354 km within Türkiye), Kura (189 km within Türkiye), and Aras (548 km within Türkiye). On the other hand, the Asi (88 km within Türkiye) and Meriç (187 km within Türkiye) rivers originate in neighboring lands before converging along Türkiye's coastlines.

Türkiye's diverse precipitation patterns across different regions and seasons and varying riverbed gradients lead to dynamic changes in river flow rates, water volumes, sediment transport, and erosional capacities throughout the year (DSI, n.d.). The substantial riverbed gradients offer a promising potential for hydropower generation while simultaneously posing challenges for river transportation due to the intricate morphology of the riverbeds. These distinct hydrological characteristics underscore the significance of comprehending Türkiye's complicated river dynamics and their multifaceted implications across sectors. Such comprehension is pivotal in steering the nation's effective resource management and sustainable development endeavors.

Given Türkiye's varied geographical features, fluctuating climate, and increasing water requirements, a hydrological model is imperative for fostering sustainable water management, enhancing disaster resilience, and facilitating well-informed policymaking.

A thesis by Çolak, 2017 delves into the predictability of streamflow, a crucial aspect in water resources management and hydroelectric energy production. It explores a spectrum of hydrologic modeling approaches, spanning physically-based models reliant on future data sets and data-driven models harnessing inherent seasonality and autocorrelation in streamflow data. Focusing on the prediction of monthly streamflow data in the Çoruh Basin from 2000 to 2011, it leverages precipitation

data from TRMM and ground-based stations (MGM). It validates predictions against independent DSI streamflow measurements. Employing diverse modeling techniques, including Simple Linear Regression (SLR), Multiple Linear Regression (MLR), Artificial Neural Networks (MLP), and Copula Models (Normal Copula and Frank Copula), the study compares predictions against climatology- and persistence-based forecasts. Findings highlight the efficacy of climatology-based methods, exhibiting correlations exceeding 0.90 for complete data sets. Persistence-based predictions also demonstrate robust performance, while adding standardized anomaly components enhances predictions. In summary, this thesis advances our understanding of streamflow predictability, emphasizing the effectiveness of different modeling techniques and the pivotal role of climatology-based approaches in achieving accurate predictions.

A study (Saber & Yılmaz, 2018) aimed to assess the potential of GSMaP for flash flood simulation in Mediterranean catchments. The research followed a three-step process: comparing GSMaP estimates with gauge-based data, developing a bias correction scheme using a rain gauge network, and employing the Hydro-BEAM hydrologic model for flash flood simulation with corrected and uncorrected GSMaP data. The study highlighted GSMaP's tendency to underestimate heavy precipitation events and overestimate light ones, emphasizing the need for threshold-based analysis in satellite-based rainfall product evaluation. The developed correction scheme improved flash flood simulation performance, with further investigation recommended to incorporate local variables for enhanced accuracy.

A different study aimed to model rainfall-runoff processes in a 10,508 km² catchment using HEC-HMS by Mesta et al. (2019). It was part of a TÜBİTAK-funded project that developed a geographical information systems-based decision-making tool for water quality management in the Ergene watershed. Meteorological data (daily precipitation and temperature) and daily streamflow data were collected, alongside land use, hydrologic soil groups, and elevation data integrated into a GIS. The hydrological model, calibrated with 1997-2002 streamflow data and validated with 2003-2005 data, demonstrated favorable performance at the Yenicegözüce

stream gauge, with Nash-Sutcliffe Efficiency (NSE) values of 0.8 (calibration) and 0.75 (validation). Similar sub-catchment models were also developed, calibrated, and evaluated using NSE values and correlations, indicating successful model performance.

A study by Çallı et al. (2022) addresses the challenge of incorporating snow recharge into karst hydrological models, like KarstMod and Varkarst, which typically lack a snow routine to avoid model complexity. The absence of snow representation raises accuracy concerns, especially in high-altitude karstic aquifers. A novel pre-processing method called the Snow-Covered Area (SCA) routine is introduced to address this. Driven by temperature, precipitation, and satellite snow data, it classifies precipitation as rain, snow, or mixed based on temperature and distributes each phase across the catchment using SCA products. Coupling the SCA routine with the KarstMod model significantly improves spring discharge simulations. Comparisons show that SCA-enhanced simulations outperform models without a snow routine and the Degree-Day method, achieving a higher Nash-Sutcliffe Efficiency (NSE) value of 0.784. This approach offers a more physically realistic parameter set, benefiting snow-dominated karstic aquifers, as demonstrated in the Central Taurus region of Türkiye.

Kumanlioglu & Fistikoglu (2019) aimed to enhance a conceptual hydrological daily rainfall-runoff model (GR4J) by incorporating an artificial neural network (ANN) and genetic algorithm (GA). By integrating ANN, the model's performance was improved by eliminating routing parameters. The integration of GA allowed automatic calibration. Applied to the Gediz River Basin, Türkiye, the hybrid model showed superior predictive capabilities compared to both the original GR4J model and a standalone ANN-based model.

Another study focuses on the Ayamama watershed, aiming to develop a model using HEC-HMS, simulate a significant 2009 flood event, and evaluate the model's performance (Kazezyılmaz-Alhan et al., 2021). Dividing the area into subbasins, defining natural water channel features, and incorporating rainfall data, the study

emphasizes HEC-HMS's ability to capture watershed characteristics. Results match well with a previous method and underscore HEC-HMS's physical insights for flood management planning in high-risk areas. This work establishes HEC-HMS as a powerful tool in urban flood risk assessment and management.

2.2 Climate Change

Climate change refers to prolonged shifts in weather patterns and temperatures stemming from natural causes like solar fluctuations or volcanic activity (UN, n.d.). However, since the 1800s, human actions, especially burning fossil fuels like coal, oil, and gas, have become the primary driver of climate change (UN, n.d.). These fuels release greenhouse gases that create an insulating layer around the Earth, trapping solar heat and raising temperatures. Current warming, around 1.1°C above the late 1800s, surpasses recorded temperatures in the last 100,000 years (UN, n.d.). The most recent decade holds the warmest record, with the previous four decades consistently warmer since 1850 (UN, n.d.).

While many associate climate changes primarily with escalating temperatures, temperature increases represent only the initial aspect of the situation. As the Earth functions as an interconnected system, modifications in one facet can reverberate across all others, resulting in more frequent extreme events.

The consequences of climate change encompass a variety of issues; extensive evidence, combined with consistent trends worldwide, strongly indicate that observed changes in terrestrial and freshwater species' behaviors, ranges, and attributes are a result of regional and global climate shifts (Parmesan et al., 2022). These shifts are particularly noticeable in the escalation of extreme events. Recent studies, encompassing over 12,000 species globally, demonstrate changes that align with climate change.

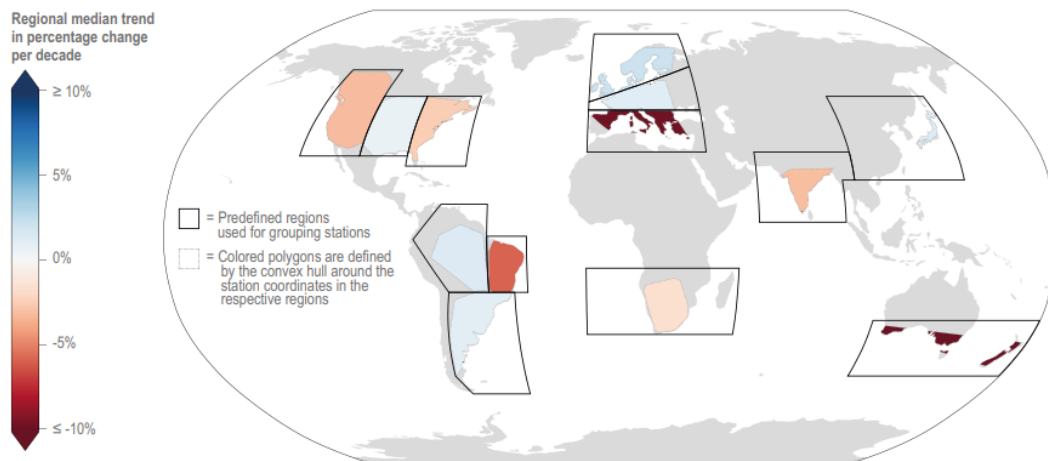


Figure 2-1 Global Analysis Annual Mean River Flow Trends across Regions From 7250 Observatories (1971–2010) (Gudmundsson et al., 2021)

It could also be observed from Figure 2-1 that various regions, including northeast Brazil, southern Australia, and the Mediterranean, are undergoing drying trends, whereas northern Europe is experiencing increased wetness. These shifts result from substantial changes in precipitation patterns, modifications in factors influencing evapotranspiration, and adjustments in the timing of snow accumulation and melting due to rising temperatures (Gudmundsson et al., 2021). These alterations are brought about by significant modifications in precipitation patterns, adjustments to the determinants of evapotranspiration, and changes to the time of snow buildup and melting due to warming temperatures.

Ecosystems are undergoing biome distribution and structure changes that align with climate change and the increasing presence of CO₂ (Parmesan et al., 2022). Climate change presents substantial risks to both terrestrial and freshwater ecosystems. If global mean surface air temperatures increase by five °C, the potential for species extinctions could rise to 60% (Parmesan et al., 2022). Changes in significant vegetation forms, known as biome shifts, could impact 15% (at 2°C warming) to 35% (at 4°C warming) of global land. Additionally, the area burned by wildfires could increase by 35% (at 2°C warming) to 40% (at 4°C warming) of global land (Parmesan et al., 2022).

The irreversible species loss becomes more pronounced with higher temperatures, affecting ecosystem integrity and resilience. Biome shifts could impact up to 35% of global land, leading to significant alterations in ecosystems like the Amazon rainforest and boreal forests (Parmesan et al., 2022). Warmer temperatures also elevate the risk of wildfires, projecting a 30% increase in frequency with 4°C GSAT warming (Parmesan et al., 2022). Moreover, climate change intensifies the potential release of stored carbon into the atmosphere due to factors such as wildfires, tree mortality, insect infestations, peatland drying, and permafrost thaw.

2.2.1 General Circulation Models (GCMs)

GCMs are mathematical representations that capture the physical interactions of the atmosphere and ocean, allowing them to simulate how the global climate responds to the growing emissions of greenhouse gases (IPCC, 2013). Some commonly used GCMs are MPI-ESM-MR, HadGEM2-ES, and GFDL.

The Max-Planck-Institute Earth System Model (MPI-ESM-MR) represents an extensive circulation model developed by Germany's Max Planck Institute. It is composed of interconnected sub-modules, which include the atmospheric ECHAM6 model (Stevens et al., 2013), the MPIOM ocean model (Jungclaus et al., 2013), the land and vegetation subsystem model JSBACH (Schneck et al., 2013), the ocean biogeochemistry model HAMMOCC5 (Ilyina et al., 2013) and the OASIS module facilitating concurrent functioning. The interaction among these models is depicted in Figure 2-2. ECHAM6, the atmospheric GCM, collaborates with the physical and biogeochemical soil and vegetation model JSBACH. The ocean's GCM MPIOM integrates with the underwater biogeochemistry model HAMOCC. The OASIS module ensures the synchronized operation of these central components, managing daily flows of water, energy, momentum, and CO₂ between models (Giorgetta et al., 2013). The MPI-ESM model is offered in three versions based on resolution: MPI-ESM-LR (Low Resolution - Dynamic Vegetation), MPI-ESM-MR (Medium Resolution - Dynamic Vegetation), and MPI-ESM-P (Low-Resolution Paleo Mode

- Static Vegetation) (Afshar et al., 2020). MPI-ESM-MR has an atmospheric grid resolution of 1.8653 degrees latitude by 1.875 degrees longitude, while the ocean grid employs a curvilinear coordinate system.

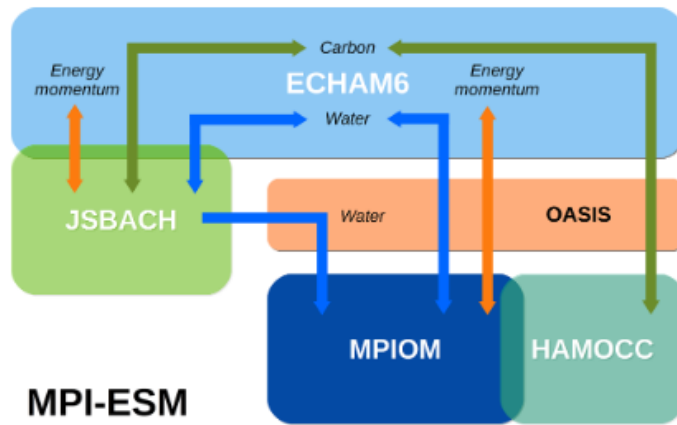


Figure 2-2 Schematic Structure of MPI-ESM Model (Cotronei & Slawig, 2020)

HadGEM2 (Hadley Centre Global Environment Model version 2) represents the second generation of global models, comprising a range of HadGEM2 models that focus on atmospheric, hydrological, and oceanographic cycles. The Hadley Centre Global Environment Model, or HadGEM2, is a collection of HadGEM2 models concentrating on atmospheric, hydrological, and oceanic cycles. It is a member of the second generation of global models. While sharing a common physical foundation, these models exhibit varying levels of detail. An integrated atmosphere-ocean setup unifies them and offers enhancements in stratospheric modeling and versatile surface system configurations encompassing dynamic vegetation, ocean biology, and atmospheric chemistry (Collins et al., 2008). The standard atmospheric model module is structured with approximately 38 layers that extend to about 40 km, utilizing a 192 x 145 global grid system with a horizontal resolution of 1.25 degrees latitude by 1.875 degrees longitude. In the extended vertical (atmospheric) version, 60 atmospheric layers stretch up to 85 km, which is crucial for investigating atmospheric processes and their global climate implications. The ocean model component employs a 1-degree latitude by 1-degree longitude grid resolution, transitioning smoothly to a 1/3-degree solution closer to the equator. This includes

360 x 216 grid points featuring 40 uneven vertical levels above the surface, with a spacing of 10 m (Martin et al., 2011).

Developed jointly by the NOAA and Princeton University's Geophysical Fluid Dynamics Laboratory, the GFDL Global Climate Model encompasses a sophisticated mathematical framework defining key climate elements (atmosphere, ocean, sea ice, land surface) and their intricate interactions. The equilibrium of energy exchange among these components on a long-term basis holds immense significance for accurate climate forecasting. The GFDL CM2.0 and 2.1 versions, introduced in 2004, provide output accessibility through an open data platform. These versions maintain an atmospheric model with a grid of 144 x 90 (approximately 2.5 degrees latitude by 2.5 degrees longitude), incorporating 24 vertical levels using a hybrid coordinate grid where sigma surfaces smoothly transition from the surface to pressure levels above 250 hPa. The lowest model level is situated around 30 meters above the surface.

Specific climate scenarios have been established in formulating climate projections to predict climate outcomes under varying global emissions levels. Two prominent scenarios, RCP 4.5 and RCP 8.5, represent moderate and high emission possibilities, respectively. RCP 4.5, developed by the Pacific Northwest National Laboratory, anticipates a stabilization of radiative forcing shortly after 2100 through global emission reduction policies. Its underlying assumptions include lower energy intensity, expanded forested areas, increased agricultural productivity, reduced cropland and grassland usage due to dietary changes, stable climate policies, constant methane emissions, and a CO₂ emission trajectory that rises until 2040 and then declines (SEI, 2017).

Conversely, the RCP 8.5 scenario, developed by the International Institute for Applied System Analysis, assumes that no significant policy changes will occur to reduce emissions. This scenario envisions a future where elevated greenhouse gas emissions increase atmospheric concentrations. Key assumptions of RCP 8.5 include a tripling of CO₂ emissions by 2100, rapid methane emission growth, expansion of

cropland and grassland usage due to population growth, a projected global population of 12 billion by 2100, slow technological advancements, heavy reliance on fossil fuels, high energy intensity, and the absence of substantial climate protection policies (SEI, 2017). Figure 2-3 shows the carbon dioxide emissions for different scenarios.

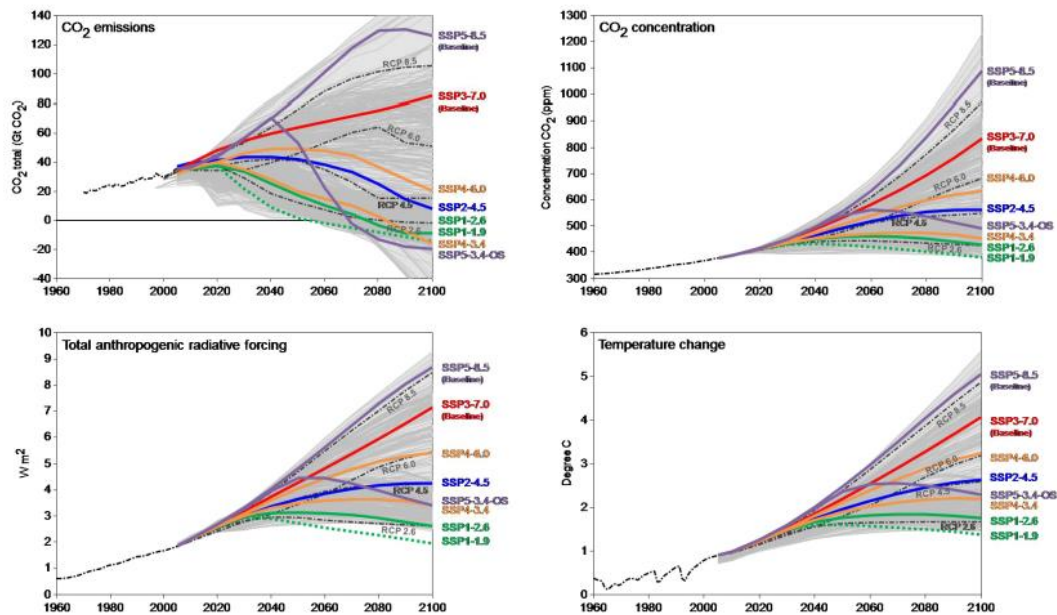


Figure 2-3 CO₂ emissions (top-left), concentrations (top-right), anthropogenic radiative forcing (bottom-left), and global mean temperature (bottom-right) for the 21st-century scenarios in the Scenario (O'Neill et al., 2016)

In this related topic, a study by Bayar et al. (2023) finds that the CMIP6 Earth System Models predict faster climate zone shifts due to more robust warming rates. Using advanced CMIP6 and earlier CMIP5 climate models, this study delves into how warming climate and precipitation changes impact climate zones and ecosystems. The models collectively indicate substantial climate zone changes, varying with ensemble subsets. By the century's end, 37.9%–48.1% of global land area is projected to shift climate zones, particularly in Europe (71.4%–88.6%) and North America (51.2%–65.8%) (Bayar et al., 2023).

The foundation of many studies concerning the impacts of climate change rests on predictions generated by global circulation models (GCMs). Initially developed to

evaluate the worldwide consequences of different emission trajectories and advocate for mitigation actions, these models have evolved into crucial tools for understanding the complexities of climate dynamics and their effects (OECD, 2013). To mitigate the impact of climate change and safeguard the planet's natural balance for future generations, emission mitigation aims to limit the amount of greenhouse gases released into the atmosphere. Concurrently, effective adaptation measures play a pivotal role in managing water risks, fortifying resilience, and minimizing the overall impacts of climate change on water resources and the ecosystems they support.

GCMs are critical tools for projecting precipitation in climate change scenarios, yet they cannot capture fine-scale spatial variations. Generating high-resolution precipitation scenarios using regional climate models (RCMs) nested within GCMs for specific regions is computationally intensive and warrants justification primarily when RCMs enhance the accuracy of regional climate projections compared to the driving GCMs (Eden et al., 2014). To obtain RCMs, the GCMs are dynamically downscaled. Dynamical downscaling is a technique that involves conducting high-resolution regional simulations to dynamically project the impacts of large-scale climate phenomena onto regional or local scales of concern (GFDL, n.d.).

2.2.2 Climate Change Effects on Water Resources

In the late 1980s, a significant shift occurred in natural sciences, with the Intergovernmental Panel on Climate Change (IPCC) assessments spotlighting climate change as a central focus for scientific endeavors (Seibert & Bergström, 2022). This shift also profoundly impacted hydrological modeling due to the recognition of climate change's influence on water resources, particularly in response to extreme hydrological events worldwide.

Climate change profoundly influences the entire water cycle, and water is the primary conduit through which climate change effects manifest. This phenomenon entails an ongoing intensification of the water cycle, characterized by escalated

evapotranspiration and precipitation, due to the impact of climate change (Huntington, 2006). Essentially, in a warmer atmospheric environment, the water cycle accelerates.

The repercussions of climate change on freshwater encompass a range of effects such as altered precipitation patterns, elevated water temperatures, deteriorating water quality, heightened evapotranspiration, and an increased frequency and intensity of extreme events (Kundzewicz et al., 2008; IPCC, 2007). These impacts are projected to grow more prominent over time, with their pace of change anticipated to escalate, leading to more severe consequences, particularly in the latter half of the century (OECD, 2013).

Climate change is projected to bring about significant shifts in precipitation patterns and increased variability, leading to global water resource changes (OECD, 2013). These changes are expected to impact runoff, groundwater recharge rates, and the occurrence of rainy seasons. Extreme weather events, such as intense precipitation, droughts, and floods, will likely become more frequent and severe due to climate change. These changes directly affect water quantity and quality, freshwater ecosystems, and various aspects of human society, including agriculture, energy, infrastructure, and biodiversity. Adapting to these changes is essential, and it calls for flexible and future-oriented strategies that consider uncertainties associated with climate predictions.

A study by Lehner et al. (2006) found that most climate change impact investigations on regional water resources primarily concentrate on average flows and overall water availability. Unfortunately, these studies often fail to consider the effects of human water consumption. While extreme events such as floods and droughts are typically analyzed on a smaller scale, climate change and human water use can affect these events on a broader regional level (Lehner et al., 2006). To address this, the study employs the WaterGAP model for a comprehensive analysis that assesses the potential consequences of global change – encompassing both climate change and altered water use – on the frequencies of floods and droughts in Europe. The findings

highlight critical regions that could experience significant shifts in flood and drought risks, underscoring the crucial need for continental-level strategies aimed at mitigation and adaptation.

Below is the figure from the study mentioned. Figure 2-4 is an alteration in the frequency of 100-year floods examined by comparing current climate and water use conditions (1961–1990) and simulations for the 2020s and 2070s.

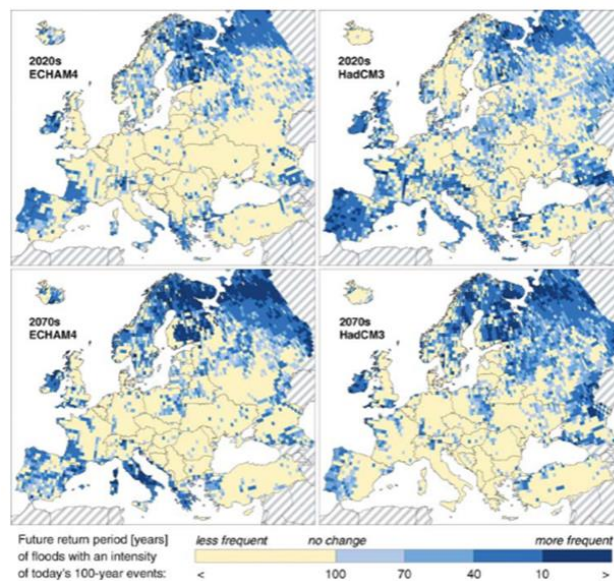


Figure 2-4 Alteration in the occurrence frequency of 100-year floods

(Lehner et al., 2006)

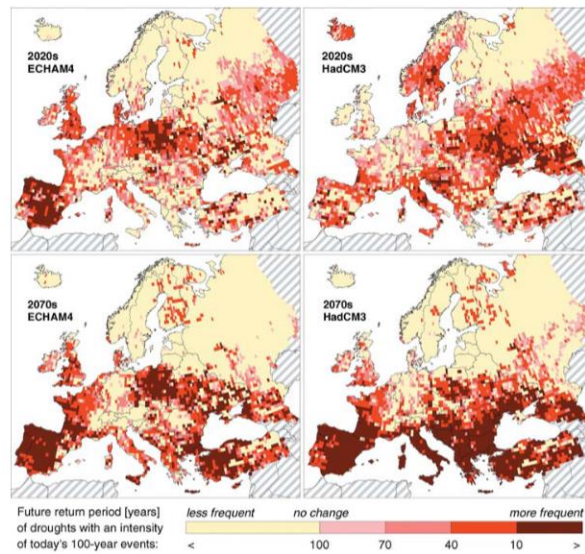


Figure 2-5 Shift in the frequency of 100-year drought events

(Lehner et al., 2006)

Figure 2-5 presents the change in the frequency of 100-year drought events assessed by comparing the present climate and water usage conditions (1961–1990) and simulations for the 2020s and 2070s. These two figures' analyses involved ECHAM4 and HadCM3 climate models and the Baseline-A water use scenario.

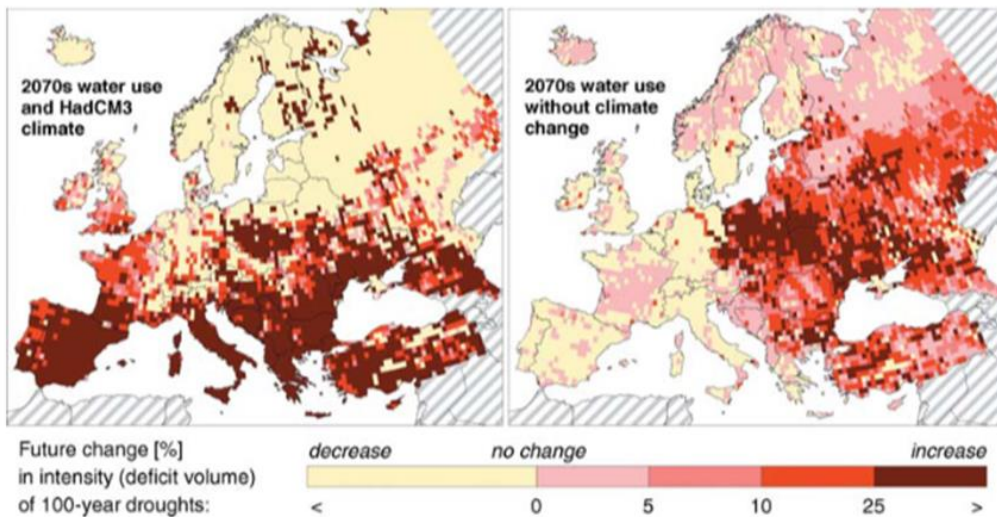


Figure 2-6 Alteration in the intensity of 100-year droughts (Lehner et al., 2006)

In the illustration presented above, the variation in the severity of 100-year droughts has been assessed by comparing the current climate and water utilization conditions (1961–1990) and simulations for the 2070s. The left map shows the results using the HadCM3 climate model and the Baseline-A water use scenario. In contrast, the correct map displays the results using only the Baseline-A water use scenario without climate change.

In these aspects, the Hydrologiska Byråns Vattenbalansavdelning (HBV) model assumed a new role in addressing climate change's effects, as seen in projects across Nordic and Baltic countries (Seibert & Bergström, 2022). Sweden's SWECLIM initiative and the establishment of the Rossby Centre further advanced regional climate scenario development, enabling interdisciplinary collaboration between meteorologists, hydrologists, and oceanographers. The HBV model is now widely used worldwide to assess how climate change may affect various regions' water resources (Seibert & Bergström, 2022). Despite successes, challenges remain, including the transferability of model applications across different climate conditions and the need for harmonization between various modeling concepts for the water cycle. Today, the HBV model is extensively employed worldwide to evaluate climate change effects on water resources in multiple regions (Seibert & Bergström, 2022). At the same time, ongoing efforts continue to refine modeling processes for the next generation of researchers.

2.2.3 Climate Change in Türkiye

Due to its geographical location, Türkiye is situated in the eastern Mediterranean, positioning it among the high-risk countries that will intensely experience the impacts of climate change (SYGM, 2020c). Similar changes to global climate shifts are already being observed in Türkiye's climate, and in the 21st century, more frequent, severe, and prolonged droughts, heatwaves, and forest fires are expected to occur in both Southern Europe and Türkiye. Additionally, an increase in the number of days with short but intense rainfall events is projected to increase sudden floods

significantly (SYGM, 2020c). According to a study cited in a report by (The World Bank, 2009), Türkiye will be one of the top three countries most exposed to extreme climate events in Europe and Central Asia by the end of the 21st century.

Numerous studies have been carried out in Türkiye focusing on climate change. Several prominent research areas within Türkiye's basins include drought, flood, renewable energy sources, forest fires, snowmelt, and agriculture. Such as elaborated research done by SYGM (2016), snowmelt runoff patterns investigated by Yucel et al. (2015), precipitation and temperature change investigated (Bağçacı et al., 2021; Gumus et al., 2023), climate change effect on drought characteristics (Afshar et al., 2020) and climate change affect on runoff (Nuri Balov & Altunkaynak, 2020; Ozkul, 2009).

One of the studies done by Yucel et al. (2015) examines snowmelt runoff patterns at 15 streamflow stations in the Euphrates, Tigris, Aras, and Çoruh basins in eastern Anatolia, Türkiye to understand their response to global climate changes. Data analysis from 1970 to 2010 reveals significant temperature increases (average 1.3°C), slight increases in annual precipitation (average 7.5%), and earlier snowmelt timings due to rising temperatures. Shifts in spring streamflow timing of up to 9 days earlier are observed. A high emissions scenario simulation projects significant decreases in annual surface runoffs for the Aras, Euphrates, and Tigris basins (11.6%, 23.5%, and 28.5%, respectively) and a slight increase for the Çoruh basin (about 4%) by the end of the century. These findings highlight the need to consider changing snowmelt patterns in dam reservoir planning and inform future regional water management policies.

In a different study done by Bağçacı et al. (2021), the performance of Global Circulation Models (GCMs) from the latest release of the Coupled Model Intercomparison Project phase 6 (CMIP6) was evaluated and compared with its predecessor, CMIP5, with a focus on monthly precipitation and temperature patterns over Türkiye, a climate change hotspot. The analysis revealed that CMIP6 models exhibited superior accuracy statistics, especially regarding precipitation, compared

to CMIP5. CMIP6 demonstrated reduced intermodel variability, indicating an improved climate signal compared to CMIP5. Specifically, CMIP6 reduced errors in precipitation and temperature by 11% and 6%, respectively, and increased precipitation correlation by 13%. Notably, the winter precipitation and autumn temperature projections showed substantial improvements. Overall, CMIP6 forecasts a slightly warmer climate (up to 0.35°C) with a 2.5% smaller decline in mean precipitation than CMIP5. However, CMIP6 captured more pronounced variations in precipitation, particularly in maximum decrease and increase, suggesting enhanced resolution of future climate variability. The study also highlighted significant summer warming (up to 6.5°C) and drying (up to -40%) trends in autumn across the country. Additionally, increased winter and spring precipitation projections in specific regions, such as the east of the Black Sea Region and northeast Anatolia, may heighten flood risks.

Another investigated topic is how climate change affects meteorological drought characteristics in Ankara, Türkiye (Afshar et al., 2020). By using observed rainfall data from local meteorological stations and downscaled data from three global climate models (GCMs) under different scenarios (RCP 4.5 and RCP 8.5), the study computed the Standardized Precipitation Index (SPI) for both historical (1986–2018) and future (2018–2050) periods. The analysis indicated a heightened probability of future drought events, potentially leading to longer durations of mild droughts and more severe and extended extreme droughts. Copula functions employed for joint return period analysis indicated a 12% decrease in the return period for extreme droughts, implying their increased occurrence. Notably, the study emphasized the need for more robust adaptation strategies to address severe drought conditions due to the anticipated rise in events with longer durations and higher severities. The results, rooted in various GCMs, showcased a significant surge in extreme droughts compared to the reference period. This underscores the necessity for broader assessments spanning more significant geographical regions to draw conclusive insights into the impact of climate change on drought characteristics.

A study by Nuri Balov & Altunkaynak, 2020) examines climate change's effects on total runoff volume in two Turkish watersheds: Melen and Munzur. Employing downscaled GCM outputs (GFDL-ESM2M, HadGEM2-ES, MPI-ESM-MR) under RCP 4.5 and RCP 8.5, the WASMOD-D hydrological model is utilized. Model parameters are optimized via a multi-objective genetic algorithm, and GCM uncertainties are mitigated using the quantile-mapping method with observed data from 1971 to 2000. Future periods of mid-century (2041–2070) and late-century (2071–2100) are assessed. The results reveal reduced water volume in both watersheds due to decreased precipitation and elevated temperatures in the mid-time and late future. By the end of the 21st century, runoff volume is projected to decline by approximately 15.42% in Melen and 26.65% in Munzur. Monthly runoff patterns remain relatively steady during the present century. While Melen experiences varying precipitation changes, Munzur generally faces decreased precipitation. Both watersheds anticipate warmer conditions throughout the year during the mid-time and late future. Despite occasional precipitation increases in certain months, decreasing runoff is expected due to temperature-induced evaporation effects. Runoff decline differs among GCMs and scenarios, with the Munzur watershed displaying more pronounced reductions.

Ozkul (2009) undertook a separate study that assessed the impact of potential climate change on water resources in the Gediz and Buyuk Menderes Basins, using various modeling analyses. The IPCC Fourth Assessment Report confirms global climate warming, affecting hydrologic systems and water resources. The study projects declining surface water potential in the basins due to decreased precipitation and increased temperature. The water budget model simulation reveals that surface waters will reduce by about 20% by 2030, rising to 35% by 2050 and over 50% by 2100. This leads to significant water stress issues, especially for agricultural, domestic, and industrial users. Rising potential evapotranspiration will also escalate irrigation water demand. The findings highlight the need for improved water management strategies and adaptation measures to mitigate the basins' vulnerability to climate change impacts.

A study done by Gumus et al. (2023) utilizes the latest CMIP6 climate models and two future scenarios (SSP2-4.5 and SSP5-8.5) to assess climate extremes in Türkiye from 2015 to 2100. Coarse-resolution climate models were downscaled to a finer $0.1^\circ \times 0.1^\circ$ (~9 km) resolution using the ERA5-Land dataset, employing three quantile mapping techniques. The findings consistently point to drier conditions, increased severe precipitation events, and rising temperatures across Türkiye under both scenarios. The SSP5-8.5 scenario indicates more pronounced water stress, with precipitation decreasing by up to 20% in the Aegean and Mediterranean regions. Precipitation extremes shift from heavy to very heavy rains, contributing to increased total precipitation from very heavy rain days. Temperature extremes, including coldest, warmest, and mean daily maximum temperatures, are expected to rise across all regions, with potential warming up to 7.5°C by the century's end. Certain regions, such as the Aegean, Southeastern Anatolia, Marmara, and the Mediterranean, exhibit higher variability in the coldest daily maximum temperatures. In contrast, the Black Sea, Central Anatolia, and Eastern Anatolia regions show greater sensitivity in mean daily maximum temperatures in response to climate change.

A study by SYGM (2016) suggests that climate change projections for Türkiye temperatures could rise by up to 3.4°C under the RCP 4.5 scenario and up to 5.9°C under the RCP 8.5 scenario by 2100. These temperature increases are expected to extend gradually from Türkiye's southern latitudes to the north over the century (SYGM, 2016).

Climate change projections for Türkiye indicate an expected increase in average temperatures across all model simulations and scenarios. Models used are the RegCM4.3 regional climate model, including HadGEM2-ES, MPI-ESM-MR, and CNRM-CM5.1 models under RCP 4.5 and RCP 8.5 scenarios, reveal temperature anomalies for each season during the 2015-2100 projection period (SYGM, 2016). The projections consistently demonstrate warmer conditions compared to the reference period. Despite some initial fluctuations, the impact of rising greenhouse gas concentrations is expected to dominate temperature increases over regional variability, resulting in significant warming across seasons and years. Winter

temperatures are projected to be at least 1°C warmer after 2050 compared to 1970-2000. By 2091-2100, temperature increases under RCP 4.5 scenario range from 2°C to 3.4°C, while RCP 8.5 predicts higher increases of 4.3°C to 5.9°C. RCP 8.5 demonstrates more significant temperature increases after the 2050s, especially in the summer and spring (SYGM, 2016).

The MPI-ESM-MR model indicates that the Eastern Black Sea, Western Black Sea, Çoruh, and Yeşilırmak Basins experience increased precipitation under RCP 8.5 compared to RCP 4.5. Conversely, 21 other basins expect reduced precipitation under RCP 8.5. CNRM-CM5.1 predicts increased precipitation in specific basins, including the Marmara Basin (SYGM, 2016). These changes suggest significant fluctuations, with winter and early spring experiencing more precipitation variations. Mediterranean coastal basins show dramatic shifts, with reduced precipitation totals projected by models like HadGEM2-ES and MPI-ESM-MR. Projections differ, indicating varying levels of drought and wetness across Türkiye's regions under RCP 4.5 and RCP 8.5 scenarios (SYGM, 2016).

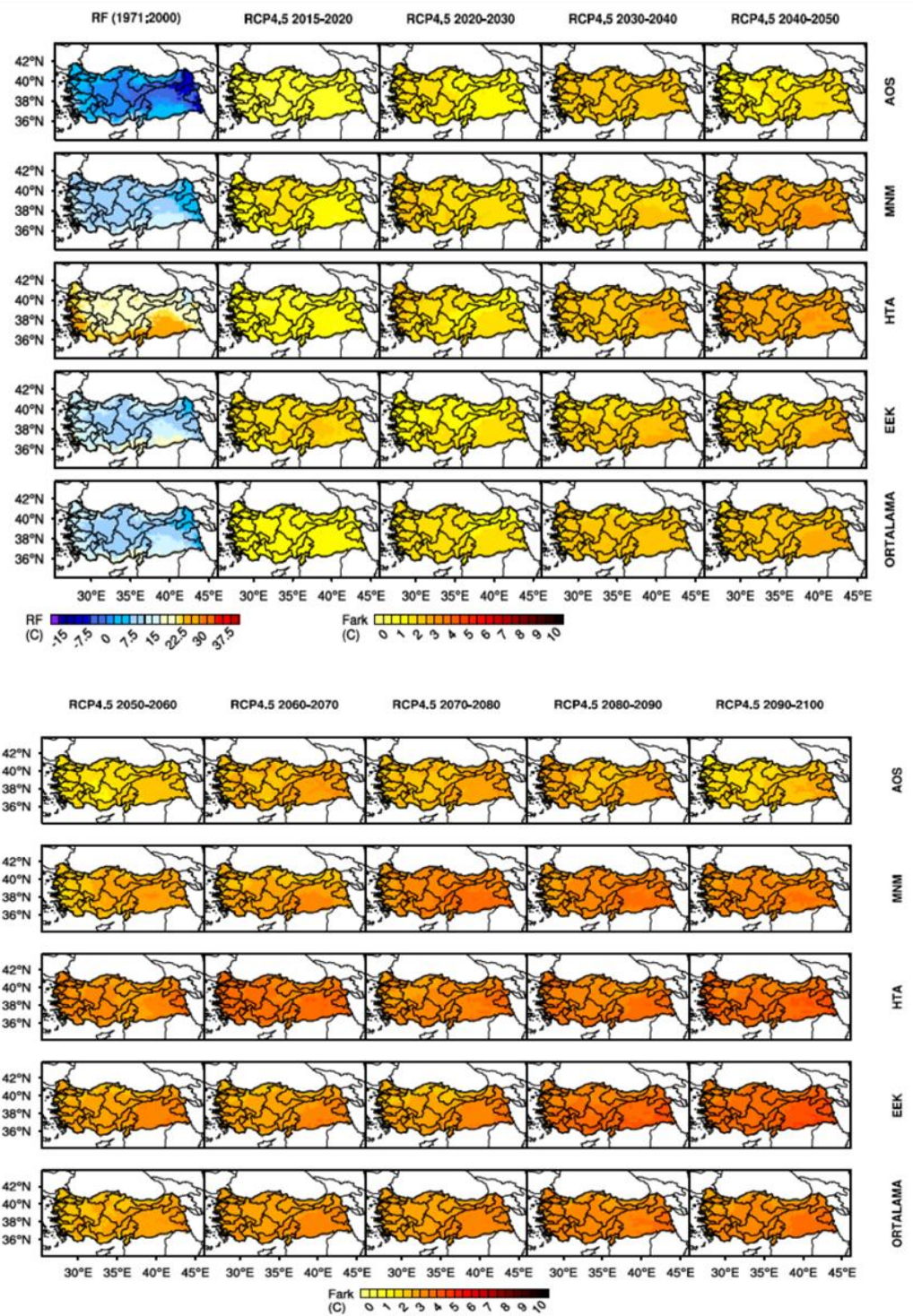


Figure 2-7 Variation in seasons across 10-year intervals for average temperature anomaly values in the HadGEM2-ES Model under the RCP 4.5 scenario (SYGM, 2016)

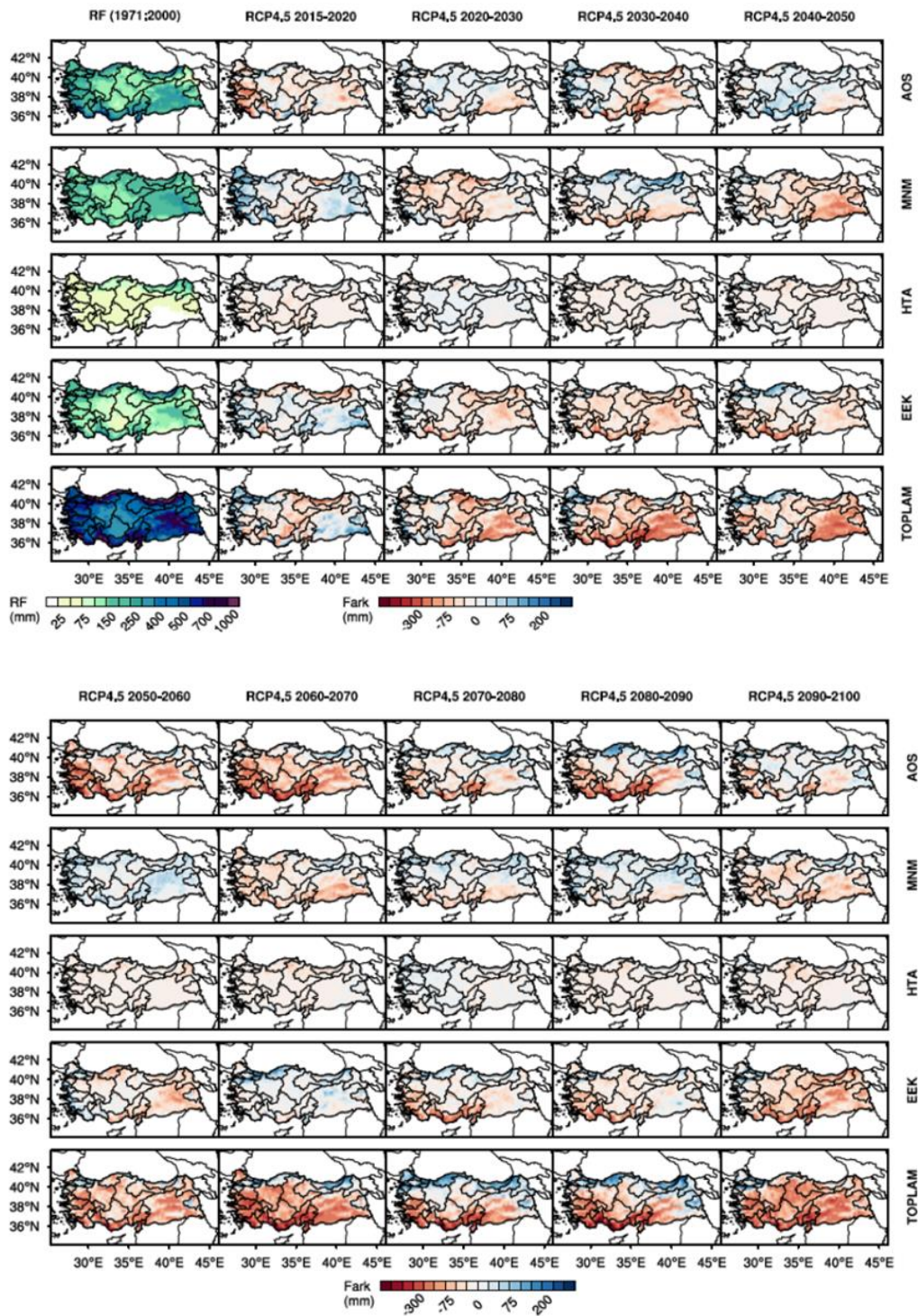


Figure 2-8 Seasonal variation of 10-year intervals for total precipitation anomaly values in the HadGEM2-ES Model under the RCP 4.5 scenario (SYGM, 2016)

2.2.4 Climate Change in Çoruh Basin

The SYGM (2020) study on the Çoruh basin's climate change projections analyzed from GCMs for 2015-2100 indicates a steady rise in average temperatures, with the basin's mean temperature expected to increase by 2°C to 5.4°C by 2071-2100, particularly pronounced in its southern regions. Precipitation patterns are also projected to shift, with a 10% increase in total precipitation during 2071-2100, mainly concentrated in the northern basin areas. Utilizing the SWAT hydrological model, the study forecasts a potential reduction of up to 20% in gross water potential by 2071-2100 due to climate change effects. Despite this, between 2015 and 2100, available water potential is anticipated to exceed total water demand in the basin, mitigating the risk of water deficit. The hydrogeological investigation reveals a groundwater hydrogeological reserve of 1 km³, with a usable reserve of 0.7 km³. Climate change is predicted to cause around 5% reduction in the hydrogeological reserve and approximately 7% reduction in the usable reserve by the end of the century. In summary, the study underscores the potential impact of climate change on rising temperatures, changing precipitation patterns, and shifting water reserves in the Çoruh basin, which could affect water resources and availability in the region.

A different study published by Yılmaz et al. (2022) investigates the analysis of forthcoming hydro-meteorological droughts by employing climate projections from a set of 13 European Coordinated Regional Downscaling Experiments (CORDEX) domain outputs. These projections were scrutinized across two distinct scenarios, namely the RCP 4.5 and 8.5, spanning the periods 2030–2059 and 2070–2099 within the Upper Çoruh Basin, Türkiye. To execute this analysis, the bias-corrected CORDEX climate projections were integrated into the Soil and Water Assessment Tool (SWAT) hydrological model. Two optimization algorithms were applied for parameter calibration: the sequential uncertainty fitting algorithm for SWAT calibration and the shuffled complex evolution (SCE) algorithm in the parameter estimation tool (PEST). Notably, the SCE algorithm yielded superior parameter solutions. This endeavor marked the inaugural comprehensive assessment of

anticipated drought occurrences in the Upper Çoruh Basin, involving the application of a standardized precipitation index and streamflow index for meteorological and hydrological drought evaluations, respectively. The study's outcomes projected changes in annual precipitation and temperature, with a range of -15.46% to 8.74%, 0.02 °C to 8.74 °C, and -2.69 °C to 5.27 °C, respectively. Moreover, it revealed an augmented likelihood of hydrological drought occurrences under RCP 4.5 and RCP 8.5 during 2030–2059. Additionally, the possibility of experiencing hydrological high-severity droughts ($>\sim 5$) and low-severity droughts ($<\sim 2$) varied between the two scenarios for the periods 2030–2059 and 2070–2099. Nevertheless, evidence remains inadequate to conclusively assert a heightened significance of hydrological and meteorological droughts in the twenty-first century.

CHAPTER 3

STUDY AREA AND METHODOLOGY

3.1 Çoruh Basin

3.1.1 General Information About Çoruh Basin

The Çoruh Basin is located within the Northeastern Anatolia Region of Türkiye. It lies between the geographical coordinates of 39°52' and 41°32' North latitudes and 39°40' and 42°35' East longitudes. Encompassing a land area of 20,265.48 km², the Çoruh Basin constitutes about 2.61% of Türkiye's overall land area (SYGM, 2020b). This basin covers portions or entire territories of provinces, including Artvin, Bayburt, Erzurum, Ardahan, Rize, Gümüşhane, Kars, and Erzincan, as it receives precipitation within its boundaries. From a settlement perspective, the basin incorporates districts from Artvin, Bayburt, and Erzurum provinces, along with villages from Erzincan and Gümüşhane provinces. The General Directorate of State Hydraulic Works (DSİ) has categorized the basin into nine sub-basins (SYGM, 2020b).

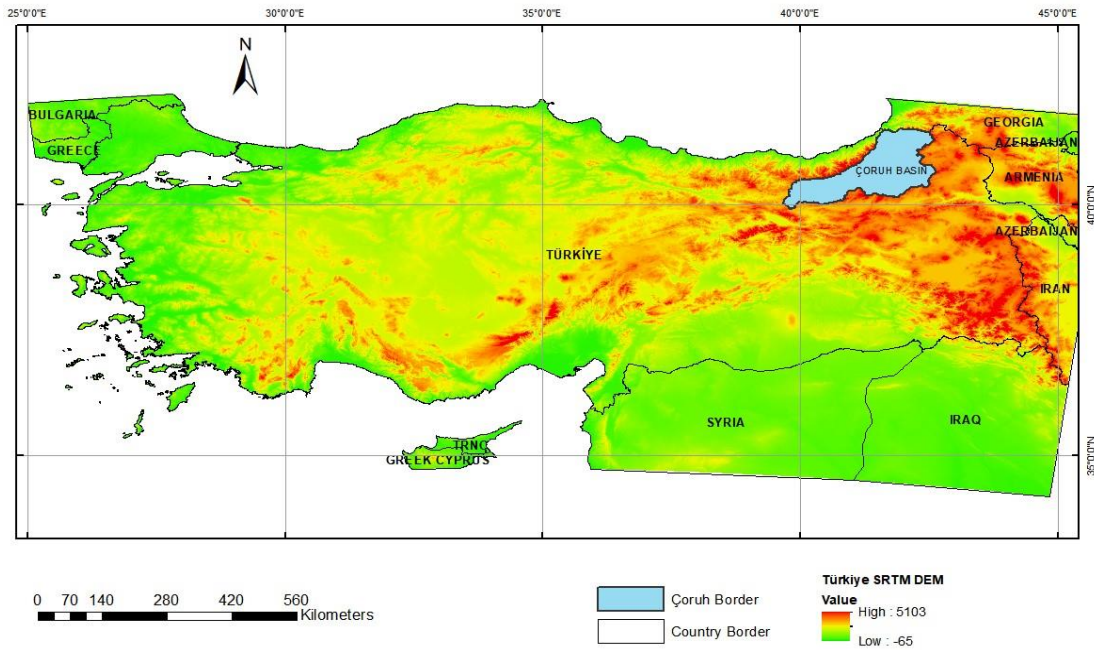


Figure 3-1 Location of the Çoruh Basin

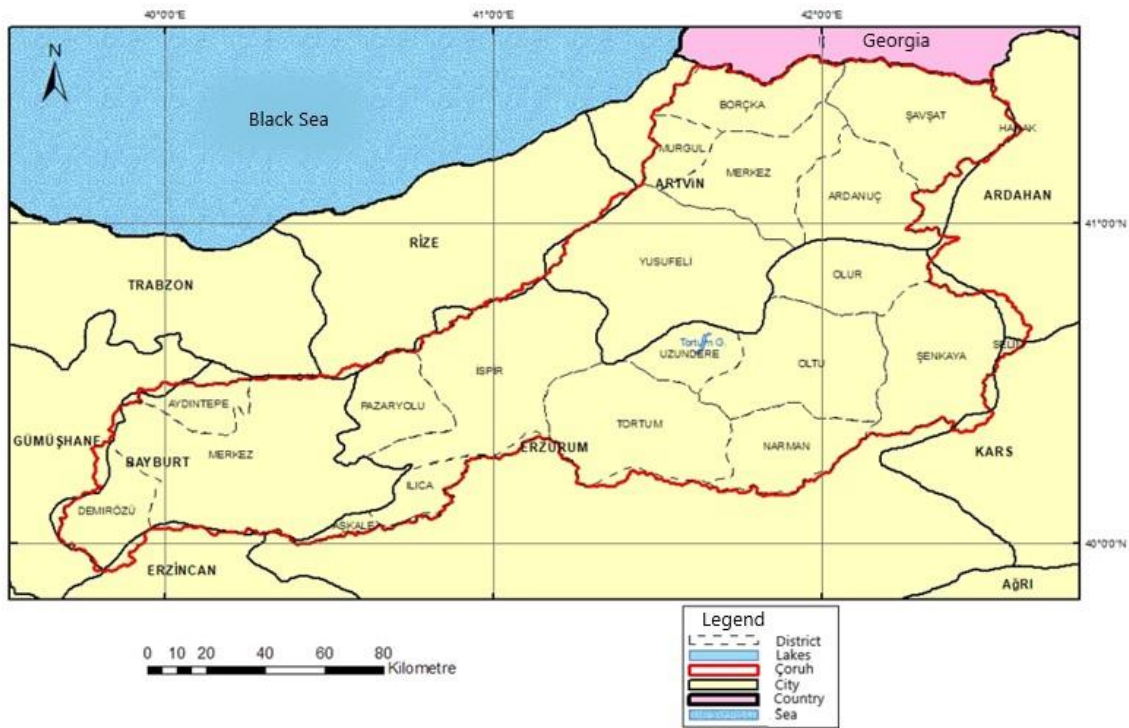


Figure 3-2 Çoruh Basin Cities and Districts

The topography of the basin is notably varied. According to the findings from the queries, the elevations span from 50 meters to an impressive 4,000 meters approximately (SYGM, 2020b). Settlements are primarily concentrated within the range of 1,800 to 2,000 meters. Beyond the 2,000-meter mark, the number of settlements experienced a significant decline. The lands between 1,800 and 2,000 meters encompass about 41% of the entire basin's area, leaving 59% outside this elevation range (SYGM, 2020b). This implies that a substantial part of the basin's surface consists of elevations unsuitable for human habitation. This rugged terrain limits the habitable areas within this region. Figure 3-3 displays a map of Türkiye with the position of the Çoruh Basin determined utilizing the digital elevation model with the Shuttle Radar Topography Mission, also known as (SRTM) (Farr et al., 2007).

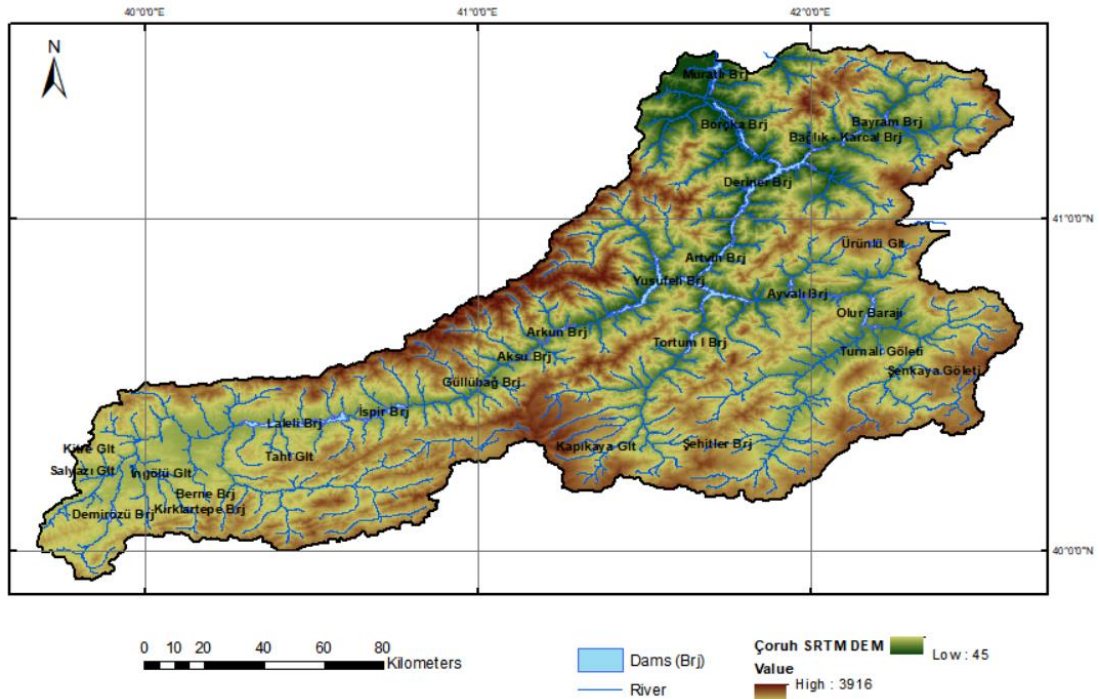


Figure 3-3 The Topography and The Dams of the Çoruh Basin

The Çoruh River, from which the basin derives its name, originates from the Mescit Mountains within the boundaries of Erzurum province. It merges with Kurt Stream in Bayburt province, becoming known as Masat Stream, and later joins Büyükçay

from the Bayburt plains, taking on the name Çoruh. After passing through Erzurum province, it enters Artvin province and leaves the country border at an altitude of approximately 50 meters. Finally, it flows from Batumi, Georgia, into the Black Sea. The main branch of the Çoruh River has a length of 296 km (SYGM, 2020b).

The Çoruh Basin's northern perimeter is framed by the Eastern Black Sea Mountains, its western side by the Giresun Mountains, and the southern edge bordered by Otlukbeli, Dumlu, Kargapazarı, Güllü, and Allahüekber Mountains. At the same time, the Yalnızçam Mountains and Georgia shape its eastern boundary. Within this basin, the lowest point is found at an elevation of 550 meters, while the highest point reaches 3,397 meters atop Mount Kaçkar (SYGM, 2020b).

The Çoruh Basin is one of the regions in Türkiye with the highest erosion rates. Approximately 500 million tons of soil are transported annually due to erosion. Currently, around 1.38% of Türkiye's electricity demand is met by dams on the Çoruh River. The Çoruh Basin holds significant importance as a vital hydropower resource in Türkiye. The fast-flowing currents of the Çoruh River have been effectively utilized to establish multiple hydroelectric power plants, playing a crucial role in augmenting the nation's renewable energy generation capacity. With projects planned by the General Directorate of State Hydraulic Works (DSİ), the total electricity generated, including hydroelectric power, from the Çoruh River is expected to contribute 8% of the total production and 34% of the hydroelectric power (SYGM, 2020b). Table 3-1 details these dams, and their locations are illustrated in Figure 3-10.

Table 3-1 Dams In Çoruh Basin

Sub-Basin	Dams and HESS	Annual Average Natural Flow (million m ³)	Drainage Area (Km ²)	Installed Capacity (MW)	Annual Total Energy (GWh)	Situation	Opening Year
Down Stream	Muratlı Dam and HESS	6060	19748	115	444	Operating	2005
	Borçka Dam and HESS	5645	19255	300	1039	Operating	2007
	Deriner Dam and HESS	4840	18389	670	2118	Operating	2012
Middle Stream	Artvin Dam and HESS	3837	15540	340	1026	Operating	2015
	Yusufeli Dam and HESS	3789	15250	540	1888	Operating	2022
Up Stream	Arkun Dam and HESS	1814	6853	237	779	Operating	2014
	Aksu Dam and HESS	1500	6338	160	383	In Construction	-
	Güllübağ Dam and HESS	1400	5915	96	280	Operating	2012
	İspir Dam and HESS	902	4915	97	272	In Construction	-
	Laleli Dam and HESS	936	4760	105	241	Operating	2017

Most of the basin occupies elevations surpassing 1,800 to 2,000 meters, resulting in a prevalence of regions characterized by heightened elevation and steep inclines (SYGM, 2020b). Evaluations of slope categories adhere to the standards outlined in the Soil and Land Classification Standards Technical Directive. In line with this classification, approximately 50% of the entire basin, covering an area of 1,015,063 hectares, falls within regions boasting slopes of 45% or more, signifying very steep slopes (SYGM, 2020b). An additional 30% of the basin's expanse, equivalent to 602,112 hectares, is designated as areas with slopes ranging from 20% to 45%, representing steep slopes.

A hypsometric curve, or cumulative height distribution, represents elevations or heights within a specific area, typically depicted on a topographic map or elevation data. It shows the cumulative land area or terrain percentage below each elevation value. A hypsometric curve illustrates how much of a region's area is located at or below a specific elevation. The Hypsometric curve of Çoruh Basin is given in Figure 3-4.

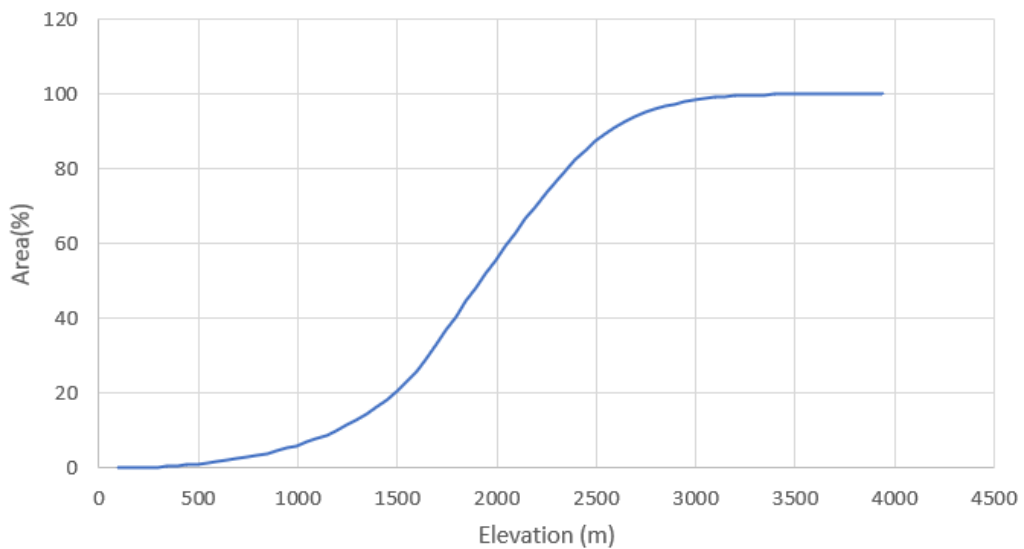


Figure 3-4 Hypsometric Curve of Çoruh Basin

The Çoruh River is one of the largest rivers in Northeastern Anatolia. Its source is derived from the spring waters on the western slopes of Çivilikaya Hill, located

southwest of the Mescit Mountains (3,239 m). Flowing between the Eastern Black Sea Mountains and the Mescit Mountains, it ultimately reaches the Black Sea south of Batumi Port. The river spans a length of 466 km from its source to its mouth (SYGM, 2020b).

The Çoruh Basin benefits from many small and large tributaries, originating at altitudes near 2,000 meters (Fakioğlu et al., 2009). Coupled with the Çoruh River's descent from 50 meters as it leaves Turkish territory, this geographical configuration allows for swift elevation changes across short distances. This unique terrain, coupled with restricted agricultural water consumption, establishes the basin as remarkably conducive for establishing dam and river-type power plants. As a result, the Çoruh Basin stands out as one of the most advantageous regions concerning hydropower potential. The combination of these factors positions the basin as highly favorable for harnessing hydropower resources.

The Çoruh River serves as the primary watercourse within the basin, wielding substantial influence over the geography and economy of the region. Renowned for its formidable characteristics, the Çoruh River stands among the world's top ten white-water rivers (T.C. KTB, n.d.). Its notable volume is predominantly fueled by the melting snow in the Eastern Black Sea mountains, a feature that contributes to its rapid and tumultuous currents. These dynamic qualities have earned the river a reputation that beckons adventure sports enthusiasts, making it a sought-after destination for activities like whitewater rafting and kayaking (T.C. KTB, n.d.).

3.1.2 Climate of Çoruh Basin

The Çoruh Basin's geographical location gives rise to a transitional climate that sits between the continental climate of Eastern Anatolia and the hinterland climate found behind the Black Sea. The northern stretch of the Çoruh Valley experiences the influence of moisture-laden air masses originating from the Eastern Black Sea Mountains, resulting in a milder climate. Conversely, the southwestern side is

sheltered from cold air masses by natural features such as the Otlukbeli and Dumlu Mountains and the Erzurum-Kars Plateau. This dynamic leads to a climatic spectrum ranging from the more rigorous Black Sea climate to the gentler Eastern Anatolia climate. Summers are warm and dry, while winters are cool and wet, with the highest precipitation typically occurring in spring. The elevated sections of mountains on the left bank behind the Black Sea receive substantial snowfall, which melts during spring, often causing flooding after April and May rainfall.

Southern regions like Oltu and Narman exhibit a continental climate. In contrast, the northern areas around Borçka and Muratlı are characterized by the milder, rainier climate typical of the Eastern Black Sea (SYGM, 2020b).

Meteorological stations, operated by the Turkish State Meteorological Service (MGM) and the State Hydraulic Works (DSİ), are spread throughout the project area. These stations measure rain and snowfall; some even monitor snow cover depth and density. The Çoruh Basin is separated from the Eastern Black Sea Basin by the Eastern Black Sea Mountains, resulting in lower average precipitation in the Çoruh Basin compared to coastal regions. Generally, annual rainfall declines downstream within the basin (SYGM, 2020b).

The melting of snow significantly influences the flow of the Çoruh River. Using the Thiessen Polygon and the isohyetal methods, the annual average precipitation in the project area is estimated at 561.84 mm and 551.94 mm, respectively (SYGM, 2020b). The distribution of precipitation throughout the year highlights the dominance of spring (30.7%) and is followed by summer (22.8%), autumn (24.5%), and winter (22.0%) (SYGM, 2020b). This pattern indicates that the highest total rainfall occurs during the spring season in the basin.

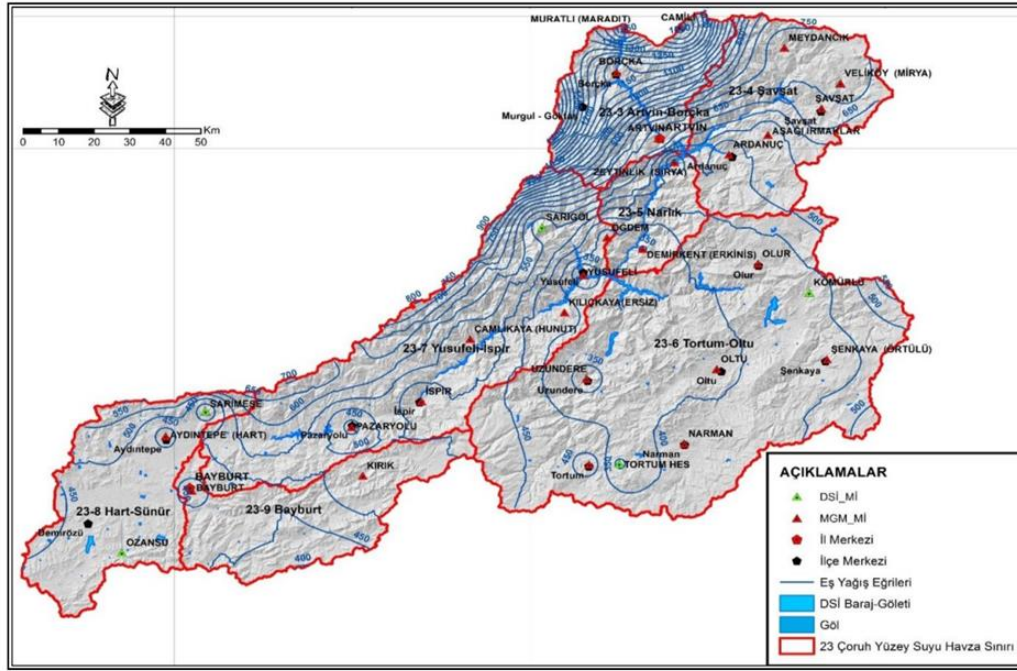


Figure 3-5 The Çoruh Basin Meteorological Observation Stations and Isohyetal (Equal Rainfall) Curves (SYGM, 2020)

The basin's average monthly and annual temperature across all stations is 9.4°C in the long term. Extreme temperatures range from -35.7°C at the Kırık Meteorological Observation Station to 45.5°C at the Ardanuç Meteorological Observation Station (SYGM, 2020b). Temperature patterns generally correspond with the area's elevation, with colder winters averaging around 0°C or lower and warming from spring onward.

Evaporation levels within the Meteorological Observation Stations (MGI) in the basin vary, with the highest recorded at the İspir station, measuring 1,102.61 mm, and the lowest at the Uzundere station, measuring 485.88 mm (SYGM, 2020b).

The climate within the Çoruh basin is influenced by the Black Sea region and Eastern Anatolia, resulting in a blend of continental and Black Sea climate characteristics.

3.1.3 Sub-basins in Çoruh Basin

There are a total number of 85 runoff observation stations. However, certain stations are utilized for short-term purposes and subsequently closed, while others exhibit missing values within their annual records. Consequently, stations that do not have a continuous time series are excluded from the analysis. As a result, the research is restricted to a subset of 30 stations. The sub-basins are created by using ArcGIS Desktop 10.7 with Arc Hydro tools. The digital elevation map employed in this study was derived from the Shuttle Radar Topography Mission (SRTM), which provides global coverage with a spatial resolution of 1 arc-second, corresponding to approximately 30 meters (Farr et al., 2007).

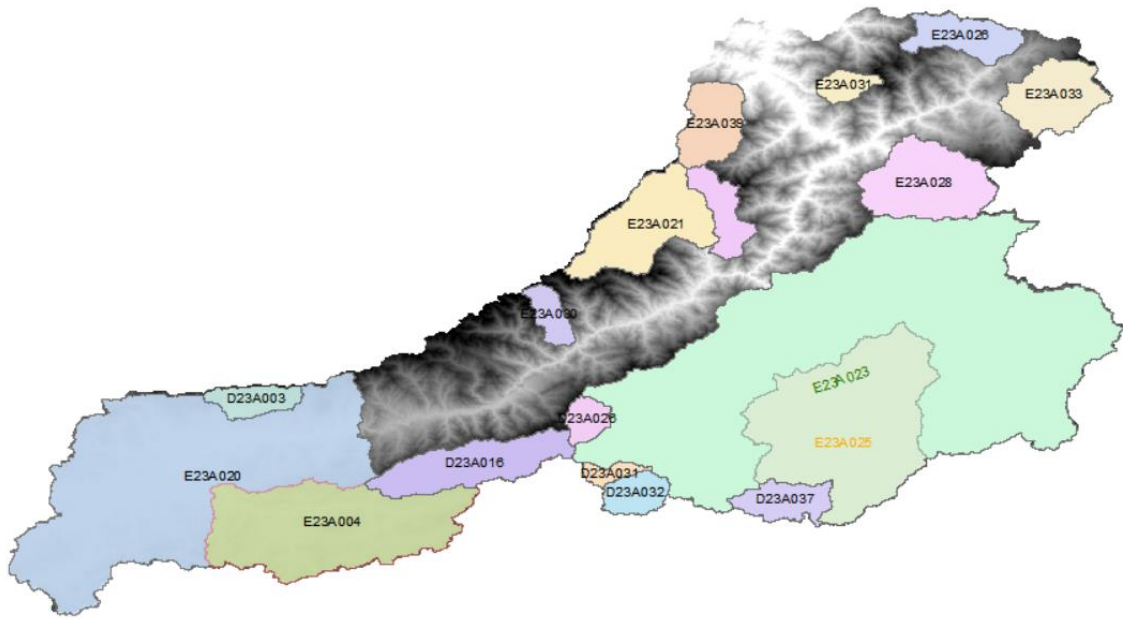


Figure 3-6 Some of the sub-basins in Çoruh

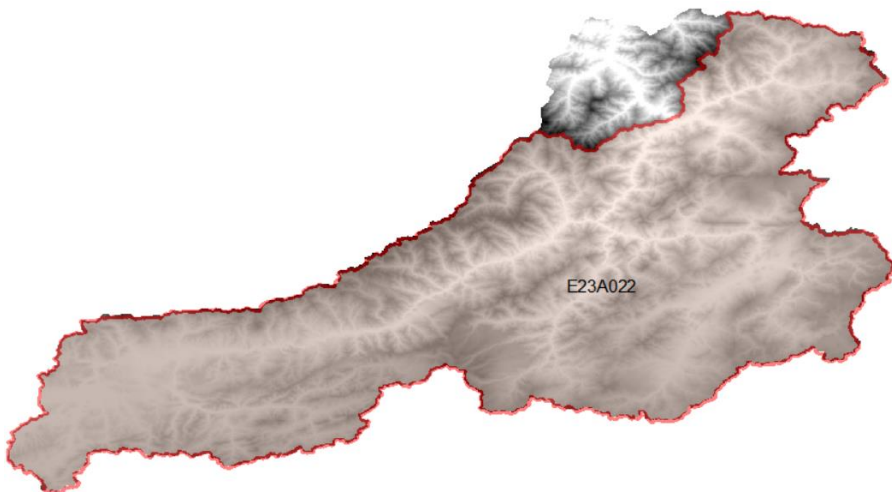
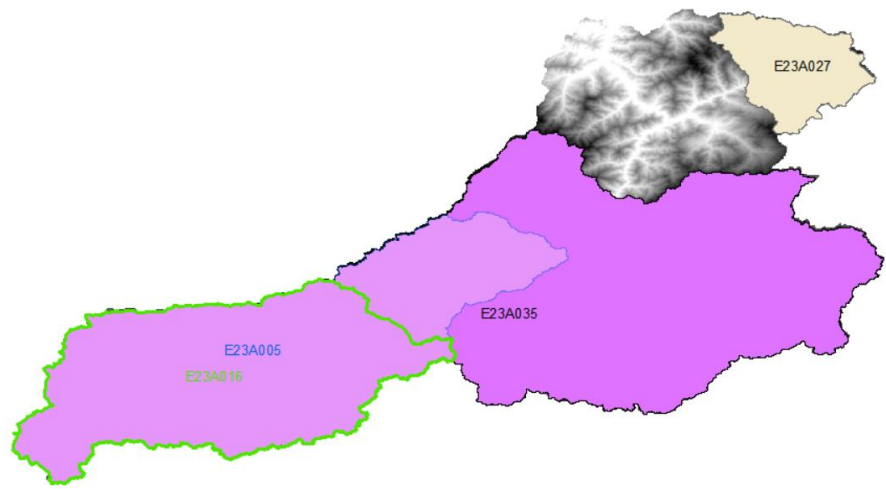
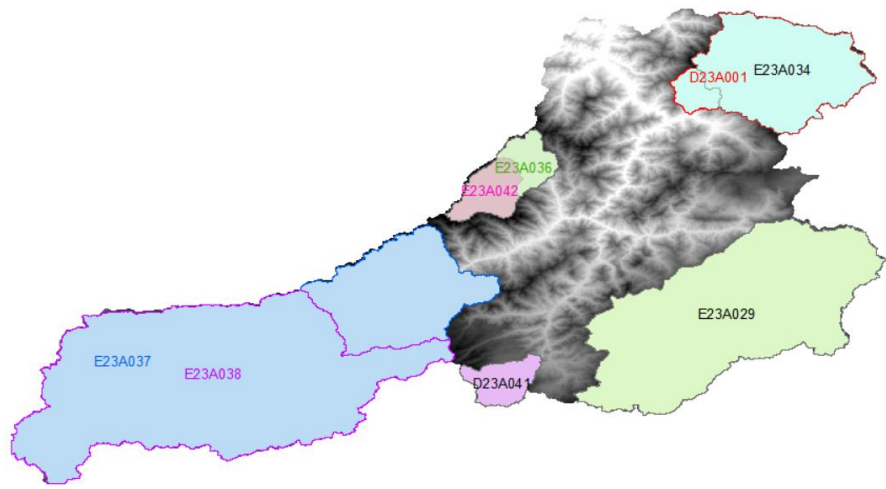


Figure 3-7 Sub-Basins in Çoruh

3.2 Datasets

This research aims to obtain accurate runoff predictions and calculate future runoff projections using the HBV model. For the study, Çoruh Basin is selected to investigate the developed model. Runoff, precipitation, and temperature data were needed to conduct the analysis. To calculate the future runoff, historical observations for runoff were used. These data were obtained from the Directorate General for State Hydraulic Works' runoff observation stations. For the temperature and precipitation data, ground-based meteorological stations were insufficient. A total of five stations were selected to represent the Çoruh basin. These data were not used directly in the analysis. Since enough data was unavailable, the ERA5-Land dataset was used for temperature and precipitation. Bias correction has been applied to the ERA5-Land dataset with the selected five representative ground-based meteorological stations. For the HBV model to be run, evapotranspiration must be used because no applicable data is observed in evapotranspiration. Thornthwaite's (Thornthwaite, 1948) formulation, which only needs the temperature and latitude of the station, was selected for the analysis. After analyzing these historical datasets, the parameters obtained were used to predict future runoff. Three GCMs with two different representative concentration pathway (RCP) scenarios were used for future predictions. In Figure 3-8, the flow chart of this study is shown.

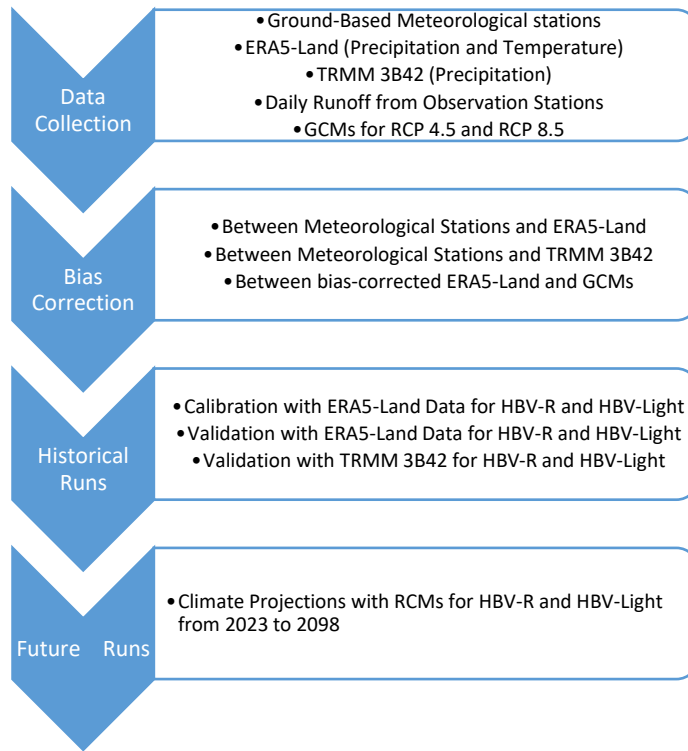


Figure 3-8 Flow Chart

3.2.1 Ground-Based Meteorological Stations

There are a total number of 63 meteorological stations in the Çoruh Basin. The temperature and precipitation data are from the Republic of Türkiye Ministry of Environment, Urbanization and Climate Change General Directorate of Meteorology. However, not all the stations have continuous data, and some have been observed only briefly. Because of these reasons, some stations had to be eliminated and choose the ones that could represent the basin best with an extended observation period. Five meteorological stations were selected for calculation in Çoruh Basin (17045, 17089, 17668, 17666, 17688) using these criteria, shown in purple in Figure 3-9. These meteorological stations were used for bias correction for ERA5-Land temperature and precipitation data.

Table 3-2 Meteorological Stations Used in Analysis

Station Id	Latitude	Longitude	Variable	Period	Variable	Period
17045	41.1752	41.8187	T (°C)	1970-2017	P (mm)	1979-2011
17089	40.2547	40.2207	T (°C)	1970-2017	P (mm)	1979-2011
17666	40.4868	40.9997	T (°C)	1970-2017	P (mm)	1979-2011
17668	40.5497	41.9951	T (°C)	1970-2017	P (mm)	1979-2011
17688	40.3013	41.5409	T (°C)	1970-2017	P (mm)	1979-2011

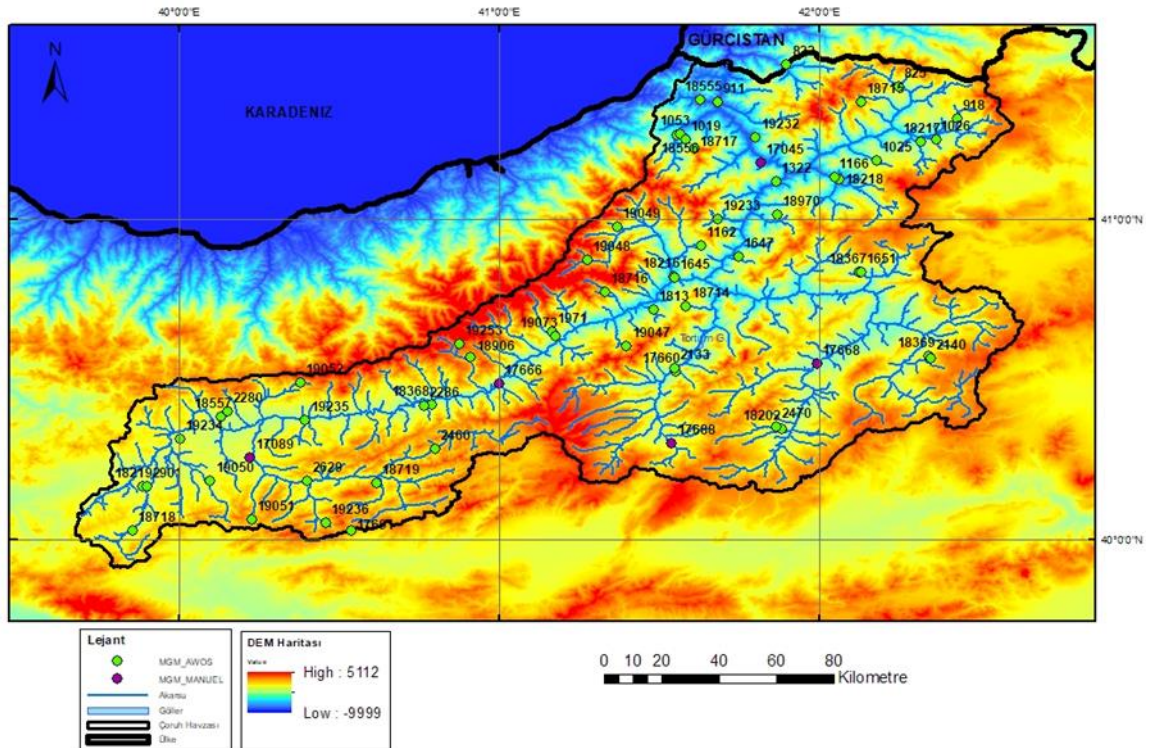


Figure 3-9 Map of Meteorological Stations

3.2.2 Runoff Observations

The annual runoff observation annuals of the General Directorate of State Hydraulic Works shared publicly, was used for runoff observation data. The annuals have daily runoff values of each located stream gauge station. There is runoff data from 1935 to 2015. However, the data length for each station is different. Some stations need more data, or the data needs to be more continuous to apply the HBV model. In Çoruh Basin, there are a total number of 85 stations. Nevertheless, by eliminating

the stations with insufficient data, 30 stations could be analyzed. In the Çoruh Basin, there are a total of six dams. Since these dams affect the natural runoff data, the data set used for the hydrological model is until the opening of the first dam in 2005. Because each station has different observation intervals, the years the model runs between differs.

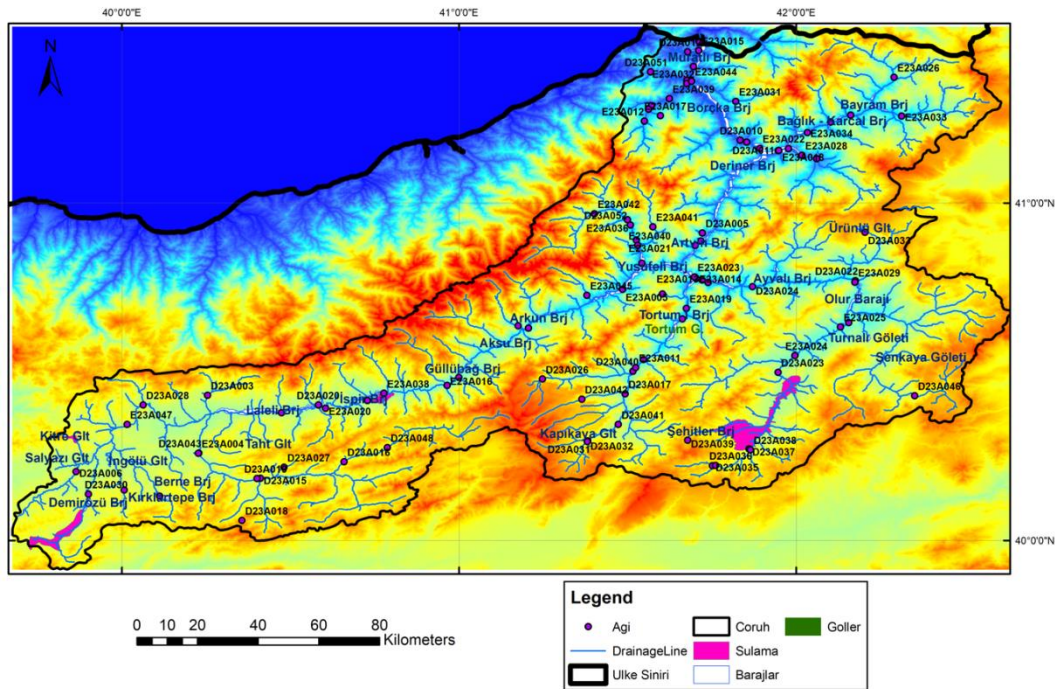


Figure 3-10 The Runoff Observation Stations and The Dams

3.2.3 ERA5-Land

ERA5-Land is a reanalysis dataset that offers an enhanced and consistent perspective on the evolution of land variables spanning several decades, surpassing the resolution of ERA5. Produced by re-running the land component of ECMWF ERA5 climate reanalysis, ERA5-Land merges model data and global observations using physical laws, yielding a comprehensive dataset portraying historical climate conditions. Employing atmospheric variables like air temperature and humidity from ERA5 as input, ERA5-Land ensures the accuracy of simulated land fields. Although not directly incorporating observations, the dataset indirectly accounts for them through

atmospheric forcing, preventing model-based estimates from straying from reality. Additionally, ERA5-Land corrects input variables to match its higher resolution grid, termed 'lapse rate correction.' Despite inherent uncertainties in model-based estimates, ERA5-Land is a valuable tool for various land surface applications like flood and drought forecasting due to its satisfactory temporal and spatial resolutions (Bell et al., 2023). Numerous studies also indicate that the ERA5-Land dataset gives good results, suggesting they could serve as substitutes for observations. (Ersoy, 2022; Gumus et al., 2023; Yilmaz, 2023a, 2023b).

In this thesis, temperature and precipitation data sets of ERA5-Land were used for HBV models because of few observation stations and insufficient data from the observation stations. ERA5-Land consists of hourly data from 1950 to the present year. The data set has a horizontal resolution of $0.1^{\circ} \times 0.1^{\circ}$ with a native resolution of 9 km.

The 2m air temperature, measured above land, sea, or inland waters, is determined by interpolating between the Earth's surface and the lowest model level while considering atmospheric conditions. The temperature unit is in Kelvin; it is converted to degrees Celsius ($^{\circ}\text{C}$) by subtracting 273.15. Additionally, since the runoff observations are daily to use the same time steps in the analysis, the hourly temperature dataset has been converted to daily by arithmetic average for 24 hours.

Precipitation, encompassing both liquid and frozen water in the form of rain and snow, descends to the Earth's surface, comprising the summation of large-scale precipitation originating from expansive weather patterns like troughs and cold fronts, as well as convective precipitation driven by warmer, less dense air ascending over more relaxed air. Excluded from precipitation variables are fog, dew, and the portion of rain that evaporates in the atmosphere before reaching the Earth's surface. This metric accumulates from the forecast's onset to its conclusion, measured in meters of depth—representing the hypothetical uniform water spread across the grid box. Because of the data compatibility, instead of hourly data, daily data is used. This parameter also accumulates precipitation in the last hour of the day. As a result,

the day's final hours were used for daily rainfall. The annual average of precipitation and temperature is shown in the figure below.

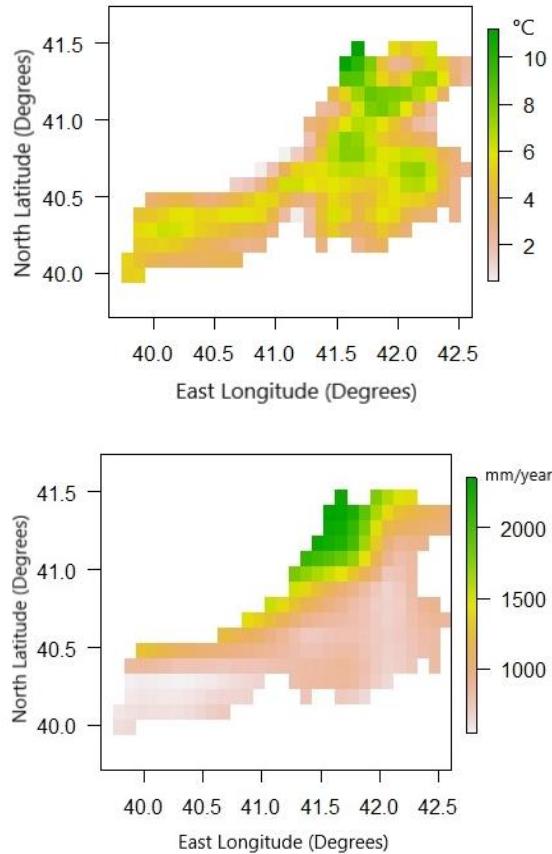


Figure 3-11 Çoruh Basin's 31-Year Average Temperature (Top) and Precipitation (Bottom) Distribution from ERA5-Land

ERA5-Land dataset is a gridded dataset for HBV analysis; a pre-process must be done. By using the observation stations, bias correction is conducted. Next, the data needs to be in a single continuous data format. To obtain the form, sub-basins are created for each station by using ArcGIS. The ERA5-Land dataset is cropped over the sub-basins, and the mean value is calculated for the area. This calculation is applied to both precipitation and temperature.

3.2.4 Climate Change Datasets (GCM)

Three different GCMs with two different RCPs are used in this study. A total of six different scenarios are conducted. Selected GCMs are HadGEM2-ES, MPI-ESM-MR, and GFDL-ESM2M. For these three models, RCP 4.5 and RCP 8.5 scenarios are used. Temperature with Celsius and total precipitation in mm parameters are obtained from the Republic of Türkiye Ministry of Environment, Urbanization and Climate Change, General Directorate of Meteorology Department of Climate and Agricultural Meteorology. The dataset is for Çoruh Basin and is in daily time step. The time series is between 1971-2000 for the reference period and 2020-2098 for the future. Bias correction is also applied to these datasets.

3.2.5 TRMM 3B42

The collaborative Tropical Rainfall Measuring Mission (TRMM) undertaken by NASA and the Japan Aerospace Exploration Agency (JAXA) investigated rainfall patterns to advance weather and climate research. The satellite was equipped with five instruments: a comprehensive three-sensor suite for rainfall assessment (PR, TMI, VIRS) alongside two complementary tools (LIS and CERES). The resultant TRMM dataset, capturing global tropical rainfall and lightning trends, emerged as a definitive standard for precipitation measurement in space (*TRMM*, n.d.). The dataset, derived from the TMPA (TRMM Multi-satellite Precipitation Analysis) Algorithm, furnishes precipitation estimates in TRMM regions characterized by the negligible bias of the "TRMM Combined Instrument" precipitation estimate. This dataset combines the advantages of minimal bias with dense, high-quality microwave data and fill-in utilizing microwave-calibrated infrared assessments. The temporal coverage of each granule is set at 3 hours (*GES DISC*, n.d.). These data supported practical applications, including flood and drought surveillance and advancements in weather forecasting techniques. A study by Çolak (2017) highlights

the importance of the TRMM (Tropical Rainfall Measuring Mission) dataset for precipitation data, which is crucial for streamflow predictions in the region.

The TRMM 3B42 rainfall dataset is converted to a daily time step for the analysis in the study. The TRMM 3B42 dataset used is years between 1998-2015. The starting period of the dataset does not cover the historical data, which runoff starts from the 1980s. Also, the ending date was in 2005. The short period makes it insufficient to run a model. Because of this reason, the dataset is only used for validation from the calculated parameter set from ERA5-Land.

Table 3-3 Information About the Used Data in the Research

Data Name	Source	Data Type	Temporal Resolution	Spatial Resolution	Time
ERA5-Land	Copernicus CDS	Precipitation, Temperature	Hourly	0.1° x 0.1°	1980-2022
TRMM-3B42	NASA-USGS	Precipitation, Temperature	3 Hourly	0.25° x 0.25°	1998-2015
HadGEM2-ES (RCP4.5, RCP8.5)	WCRP-CMIP	Precipitation, Temperature	Daily	1.25°x1.875°	1971-2000, 2020-2098
MPI-ESM-MR (RCP4.5, RCP8.5)	WCRP-CMIP	Precipitation, Temperature	Daily	1.8653°x1.875°	1971-2000, 2020-2098
GFDL-ESM2M (RCP4.5, RCP8.5)	WCRP-CMIP	Precipitation, Temperature	Daily	2.5°x2.5°	1971-2000, 2020-2098
Meteorological observation station	MGM	Precipitation, Temperature	Daily	-	1979-2021
Runoff Observation Station	DSI	Runoff	Daily	-	1980-2005

3.2.6 Potential Evaporation

Four data are needed to run the HBV model—precipitation, temperature, runoff, and potential evaporation. Because there is not any gauge to observe the latter parameter, an empirical approach is used. The selected method is the Thornthwaite equation, in which the only inputs are temperature and the station's latitude (Thornthwaite,

1948). Thornthwaite developed this methodology to estimate the potential evaporation. In the study, because the GCM dataset is in 360 days for a year, the analysis is performed based on the assumption that one year is 360 days. Due to that, the potential evapotranspiration is daily of 360 days per year. The formulation used in the analysis approximates the original method proposed by Willmott by using the $T > 26$ equation. (Willmott et al., 1985) The formulas for calculating potential evaporation are below (Wikifire, n.d.).

$$PET_{Thorn} = \begin{cases} 0, & \text{if } T < 0 \\ 16 \cdot \frac{N}{360} \cdot \left(\frac{10 \cdot T}{I}\right)^\alpha, & \text{if } 0 \leq T \leq 26 \\ \frac{N}{360} \cdot (-415.85 + 32.25 \cdot T - 0.43 \cdot T^2), & \text{if } T > 26 \end{cases}$$

N is the duration of the sunlight in hours calculated as:

$$N = \frac{24}{\pi} \cdot w_s$$

Where w_s is the sunset hour angle in radians calculated as below:

$$w_s = \arccos [-\tan\varphi \cdot \tan\delta]$$

δ stands for the solar declination in radians and the φ stands for latitude in radians.

Solar declination is calculated as:

$$\delta = 0.409 \cdot \sin\left(\frac{2\pi}{360} \cdot J - 1.39\right)$$

Here, J represents Julian's date as the day number within the year, ranging from 1 (1 January) to 365 or 366 (31 December). In the study, a year is assumed as 360 days as Julian's date.

3.3 Bias Correction

Climate model projections of precipitation and temperature often exhibit discrepancies in their statistical properties compared to the observed time series

during the control period. To mitigate these errors, bias correction methods are applied. These methods help to align the climate model outputs more closely with the statistical properties of the observed data (Soriano et al., 2019).

These methods encompass various techniques, such as linear scaling, variance scaling, power transformation, and quantile delta mapping. The choice of a bias correction algorithm plays a prominent role in assessing hydrological change (Teutschbein & Seibert, 2012).

The exploration of bias correction methods for precipitation projections has been instrumental in identifying the optimal approach for precipitation frequency curves, which may differ from the most effective way for flood frequency curves (Soriano et al., 2019). The research done by Soriano et al. (2019) underscores the pronounced significance of bias correction for precipitation time series, outweighing the importance of temperature correction. This observation is relevant for hydrological modeling, as precipitation plays a pivotal role in influencing streamflow outputs in the HBV model (Soriano et al., 2019).

The QDM for precipitation preserves model-projected relative changes in quantiles while at the same time correcting systematic biases in quantiles of a modeled series concerning observed values. The QDM for precipitation corrects systematic biases in quantiles of a modeled series with respect to observed values while preserving relative changes in quantiles that the model projected. The algorithm involves a sequential two-step process: first, future model outputs undergo detrending and bias correction using quantile mapping, aligning them with observed data; second, model-projected relative quantile changes are incorporated into the bias-corrected model outputs. Quantile mapping algorithms are widely utilized to bias correct daily precipitation series from climate models, aiming to closely align their distributional properties with those of historical observations (Cannon et al., 2015). This approach enhances the credibility of the model projections and ensures their compatibility with real-world data, which is crucial in the context of this thesis.

Various bias correction algorithms examined, the quantile delta mapping (QDM) method demonstrates marginally better performance compared to quantile mapping (QM) and detrended quantile mapping (DQM) when applied to precipitation-based extreme indices (Gumus et al., 2023). However, in the study by Gumus et al. (2023), no notably superior method was identified for extreme indices based on temperature.

In this study, two distinct approaches are employed. Firstly, the TRMM and ERA5-Land datasets are bias-corrected by proportioning the average gauge station observations (limited to five for precipitation and temperature) with average grids at the stations. Following our evaluation, it has opted to utilize the quantile delta mapping (QDM) method, as it exhibits superior performance in bias-correcting GCMs when employing the ERA5-Land dataset. This informed choice enhances the accuracy and reliability of our climate model projections, bolstering the credibility of our study.

$$\hat{x}_{m,p}(t) = \hat{x}_{o:m,h:p}(t) * \Delta_m(t)$$

$$\hat{x}_{o:m,h:p}(t) = F_{o,h}^{-1}\{F_{m,p}[x_{m,p}(t)] * \Delta_m(t)\}$$

$$\Delta_m(t) = \frac{x_{m,p}(t)}{F_{m,h}^{-1}\{F_{m,p}^{(t)}\{x_{m,p}(t)\}\}}$$

Within the context of these equations, $\hat{x}_{o:m,h:p}(t)$ denotes the bias-corrected historical period data, and $\Delta_m(t)$ signifies the relative change in the model data across both the historical and forecast periods.

3.4 The HBV Model

The Hydrologiska Byråns Vattenbalansavdelning (HBV) was developed by Sten Bergström in 1973 (Bergström & Forsman, 1973). HBV model is a widely used hydrological model in hydrology and watershed management. It is preferred owing to its inherent simplicity, ease of comprehension, and applicability. The model requires a moderate amount of input data, such as precipitation, temperature, runoff,

and evaporation. In addition, it demonstrates commendable performance across a multitude of applications. Consequently, it finds extensive application within Nordic regions and beyond international boundaries. The HBV model has different versions; investigations indicate its potential compatibility with other models.

HBV model is a conceptual model for continuous runoff simulations of stream flow and other variables. It is a mathematical model which has a simple bucket-type structure. The model is non-linear, time-variant, and dynamic. HBV model is a deterministic hydrological model, enabling the projection of future events without relying on randomness. The deterministic nature is due to the physics-based equations, deterministic input data, and single-path simulations. HBV model could be performed as a lumped model or semi-distributed model. A lumped model is typically employed for simulating diverse hydrological processes within a specific location or region. The parameters utilized in this model encapsulate spatially averaged attributes of a hydrological system and are frequently not directly comparable to field measurements (Ranit et al., 2014). A variant of the lumped technique is semi-distributed modeling. A basin is divided up into smaller sub-basins using this method. Runoff amounts obtained from methods like the unit hydrograph are used to evaluate streamflow coming from these separated sub-basins. The HBV model could be semi-distributed by dividing the catchment into sub-basins, elevation, and vegetation zones.

This study uses HBV Light Version 4.0.0.24 (Seibert, 2005) to compare a novel hydrological model. The model initialization in HBV Light should be done using a warming-up time, and a routing parameter that can accept any actual values instead of only integer values is the only two changes between HBV Light and the HBV model (Seibert, 2005).

The HBV model depicts the water balance utilizing three storage reservoirs: a soil moisture zone, an upper zone storage (for sub-surface stormflow), and a lower zone storage, as shown schematically in Figure 3-12. The general water balance equation

for the HBV model is as follows, including an algorithm for snow accumulation and melt (based on the degree-day technique) and an algorithm accounting for lakes:

$$P - E - Q = \frac{d}{dt}(SP + SM + UZ + LZ + Lakes)$$

P refers to precipitation, E to evaporation, and Q to discharge. UZ and LZ refer to the upper and lower groundwater zones, whereas SP and SM stand for snowpack and soil moisture. The lakes-term refers to the storage in lakes. The regional distribution of temperature and precipitation can be represented using a subroutine for meteorological interpolation (Driessen et al., 2010).

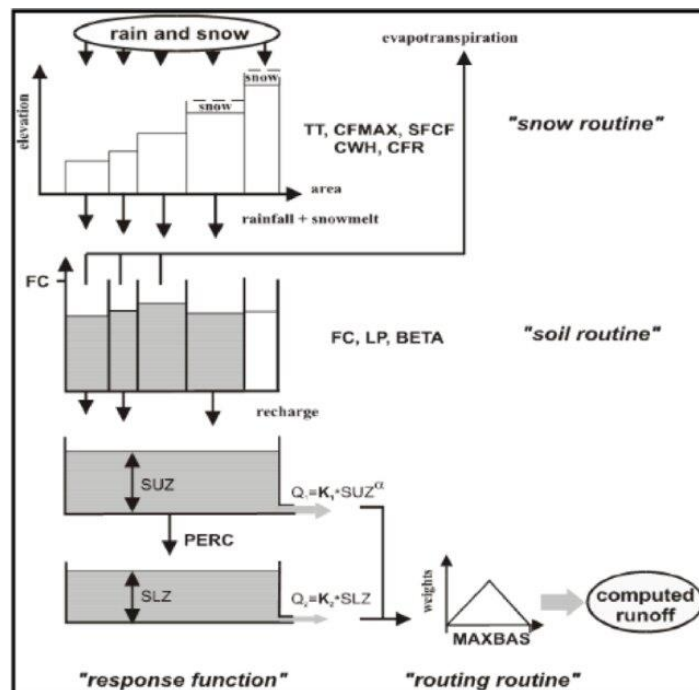


Figure 3-12 General Structure of HBV Model (Seibert, 2000)

As illustrated in the figure 3-12, the equations comprise a range of parameters. Some delineate the properties of the catchment, while others pertain to parameters associated with vegetation zones.

The model simulates discharge using rainfall, temperature, and potential evaporation as input variables. Precipitation is differentiated as snow or rain based on a threshold temperature, denoted as TT [°C]. If the temperature remains below TT, precipitation

accumulation becomes in the form of snow. Snowmelt occurs when the temperature rises above the threshold temperature. Snowfall, occurring when the temperature is below TT , is modified by a snowfall correction factor, $SFCF$ [-], which accounts for systematic errors in snowfall measurements and the unaccounted-for evaporation from the snowpack. Snowmelt follows a degree-day approach (degree- Δt for non-daily time steps) as depicted below (Bergström, 1995).

The calculation of meltwater is governed by the following equation:

$$Melt = CFMAX * (T - TT)$$

$CFMAX$ represents a coefficient characterized by a dynamic range. Notably, regions with forest cover tend to adopt lower values for $CFMAX$, commonly approximating values of 2 for forested terrain and 3.5 for open landscapes. (Seibert, 2005)

Accumulated meltwater and rainfall within the snowpack are retained until they surpass a specific fraction, expressed as CWH [-], of the snow's water equivalent. The liquid water within the snowpack undergoes refreezing according to a refreezing coefficient, CFR .

The equation governing the process of refreezing meltwater is expressed as follows:

$$Refreezing = CFR * CFMAX * (TT - T)$$

An important observation is that when the Snowpack factor (SP), which serves as an adjustment parameter, assumes a value lower than 1, the degree- Δt factor undergoes seasonal variability. Specifically, during winter, it ranges between $SP \cdot CFMAX$, while during summer, it corresponds to $CFMAX$. Notably, all simulated instances of snowfall undergo multiplication by the correction factor $SFCF$.

It is crucial to emphasize that these computations are performed independently for each elevation and vegetation zone, thereby ensuring the model's capacity to adapt to various environmental conditions. (Bergström, 1995)

The partitioning of rainfall and snowmelt (P) into soil box water content and groundwater recharge hinges on the relationship between the soil box's water content

(SM [mm]) and its maximum value (FC [mm]). Beta is the shape parameter that determines the shape of the curve. If it has higher values, the model will be transformed into a simple bucket model, meaning the soil moisture would be closer to the maximum capacity for any water that goes into the groundwater. The equation of this process is as follows:

$$\frac{recharge}{P(t)} = \left(\frac{SM(t)}{FC}\right)^{BETA}$$

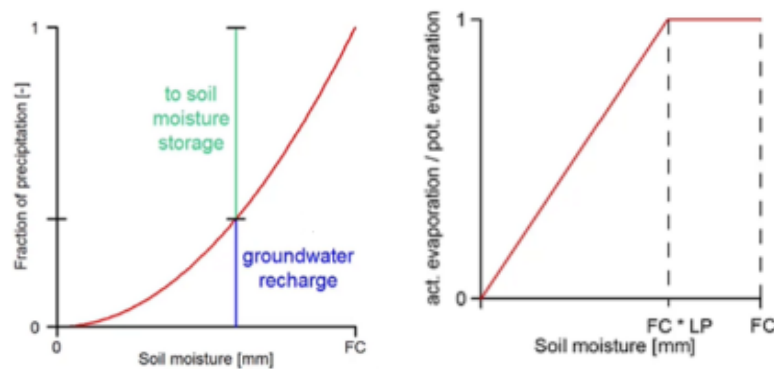


Figure 3-13 Soil Routine Graphs of the HBV Model (Seibert, 2005)

If SM/FC exceeds the limit LP [-], actual evaporation from the soil box equates to potential evaporation; otherwise, a linear reduction ensues. The value of β plays a crucial role in shaping the curve. When β equals 1, the curve appears as a straight line, as shown in the left graph in Figure 3-13. However, when β takes on higher values, typically ranging from 7 to 10, the model undergoes a transformation resembling a simplified bucket model. In this scenario, the soil moisture tends to remain closer to its maximum capacity, indicating that any water input will quickly infiltrate the groundwater. β , LP, and FC influence the amount of evaporation. They are slightly different in timing when essential, but all three influence how much water goes to runoff and how much leaves the catchment as evaporation. The flood soil box is filled in spring, so the β does not matter. Summer, the value of β is much more critical. The more significant value of β means the curve is more bent; for the same soil moisture content in the soil box, the less water will go to groundwater and

eventually to the runoff, and more water will stay in the soil box, and evaporation can happen. So, the value of β also controls the water split between evaporation and runoff. Higher values of β less water will go runoff. Different values of LP affect evaporation and, therefore, runoff. Invisible in summer flood but essential in the summer. When some water is missing in the soil box, the evaporation is reduced. It leads to a higher runoff because evaporation is negligible. Higher value in LP and FC means evaporation is more diminutive and consequently more minor runoff. As given in the equation below.

$$E_{actual} = E_{potential} * \min\left(\frac{SM(t)}{FC * LP}, 1\right)$$

In the HBV model, groundwater is represented by two boxes. The lower box represents slowly reacting groundwater, which feeds into baseflow. The upper box is the shallower groundwater that responds quickly to precipitation or snow melt input, creating higher runoff values. Groundwater recharge is introduced to the upper groundwater box (SUZ [mm]). The maximum percolation rate from the upper to the lower groundwater box (SLZ [mm]), denoted as PERC [mm Δt^{-1}], is defined. In the case of lakes, precipitation and evaporation are directly incorporated into and deducted from the lower box. Runoff stemming from the groundwater boxes is evaluated by combining two or three linear outflow equations contingent on whether SUZ surpasses a predetermined threshold, UZL [mm]. Where the outflow is dependent on the water level of the box multiplied by the constant. As soon as more water comes in as mms per day, the water level in the upper box starts to rise, and first, Q1 is activated; if the level goes higher than UZL, the Q0 also gets activated. Moreover, all three outflows contribute to runoff; all individually are linear, but the combination is non-linear. The equation is as follows:

$$Q_{GW}(t) = (K_2 * SLZ) + (K_1 * SUZ) + K_0 * \max(SUZ - UZL, 0)$$

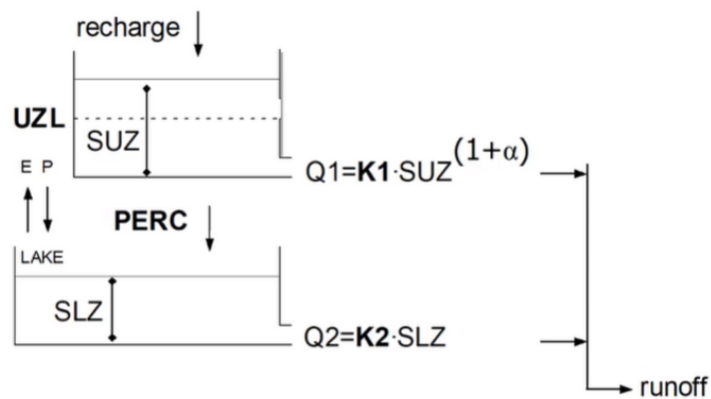


Figure 3-14 Response Routine of the HBV Model (Seibert, 2005)

Different K values influence the shape of the hydrograph. The water will eventually come to runoff when it reaches the response function. The time will change, so the area under the curve will always be the same. However, the question is when the water will come to runoff. With a lower value of K0, runoff will have less peak, and the water will last longer. If the UZL threshold is lower, it earlier activated higher runoff values for a short time, and the water will be gone rapidly, so there will be a shift in timing. The runoff is mainly affected by K0 and UZL parameters. K1 is most effective between the runoff events; lower values mean less peaky but more prolonged recession. PERC parameter controls how much water goes from the upper bucket to the lower bucket and the baseflow level. With larger values of PERC, more water goes to the lower box, contributing to an extended baseflow period. K2 affects the baseflow and is less dynamic; slower values baseflow continues constant for a long time. For higher values, there is more recession during baseflow.

Water has reached the stream network with the routines followed but has yet to reach the catchment outlet. So, there is a need to transform the water to the catchment outlet. A triangular weighting function determined by the parameter MAXBAS is applied to this runoff, culminating in the derived simulated runoff [mm Δt-1]. Transformation of the runoff as simulated by the response function is damped, and the peak is shifted slightly in time. The equation is presented as follows:

$$Q_{sim}(t) = \sum_{i=1}^{MAXBAS} c(i) * Q_{GW}(t - i + 1)$$

$$c(i) = \int_{i-1}^i \left(\frac{2}{MAXBAS} \right) - \left| u - \frac{MAXBAS}{2} \right| * \frac{4}{MAXBAS^2} du$$

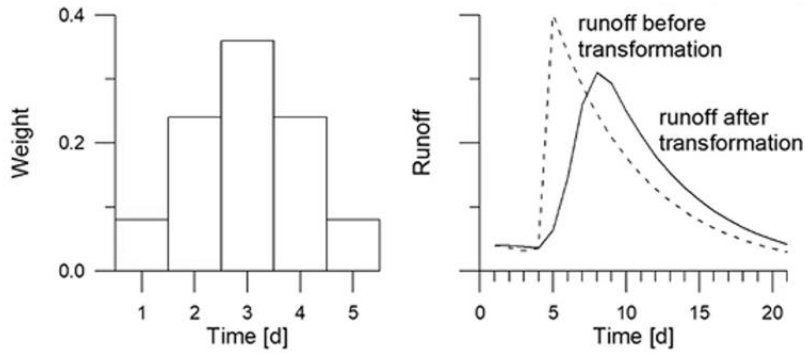


Figure 3-15 Routing Routine of the HBV Model (Seibert, 2005)

In scenarios involving distinct elevation zones, changes in precipitation and temperature corresponding to elevation alterations are calculated through the utilization of two parameters: PCALT [%/100 m] and TCALT [°C / 100 m].

$$P(h) = P_0 * \left(1 + \frac{PCALT(h - h_0)}{10000} \right)$$

$$T(h) = T_0 - \frac{TCALT(h - h_0)}{100}$$

The long-term mean of potential evaporation, $E_{pot,M}$, for a specific day of the year, can be adjusted to its value at timestep t, $E_{pot}(t)$, by considering the deviations of temperature, T(t), from its long-term mean, T_M , alongside a correction factor, CET [°C-1].

$$E_{pot}(t) = (1 + C_{ET}(T(t) - T_M))E_{pot,M} \quad \text{but } 0 \leq E_{pot}(t) \leq 2 * E_{pot,M}$$

3.5 HBV-Light and HBV-R Models

3.5.1 HBV-Light Model

The HBV-Light program can simultaneously utilize various model structures, elevation, and vegetation zones. For this study, the standard structure and basic model were adopted. The graphical interface, as depicted in Figure 3-16, enables manual adjustment of parameters, with immediate observation of the ensuing effects upon program execution. Moreover, the NSE (Nash-Sutcliffe Efficiency) value and mean difference are provided, offering valuable assistance during the manual calibration.

The interface also presents informative graphs, showcasing simulated and observed runoff, simulated snow, measured precipitation, temperature, and Qdiff (difference between observed and simulated streamflow). These graphical representations enhance the understanding and evaluation of the model's performance.

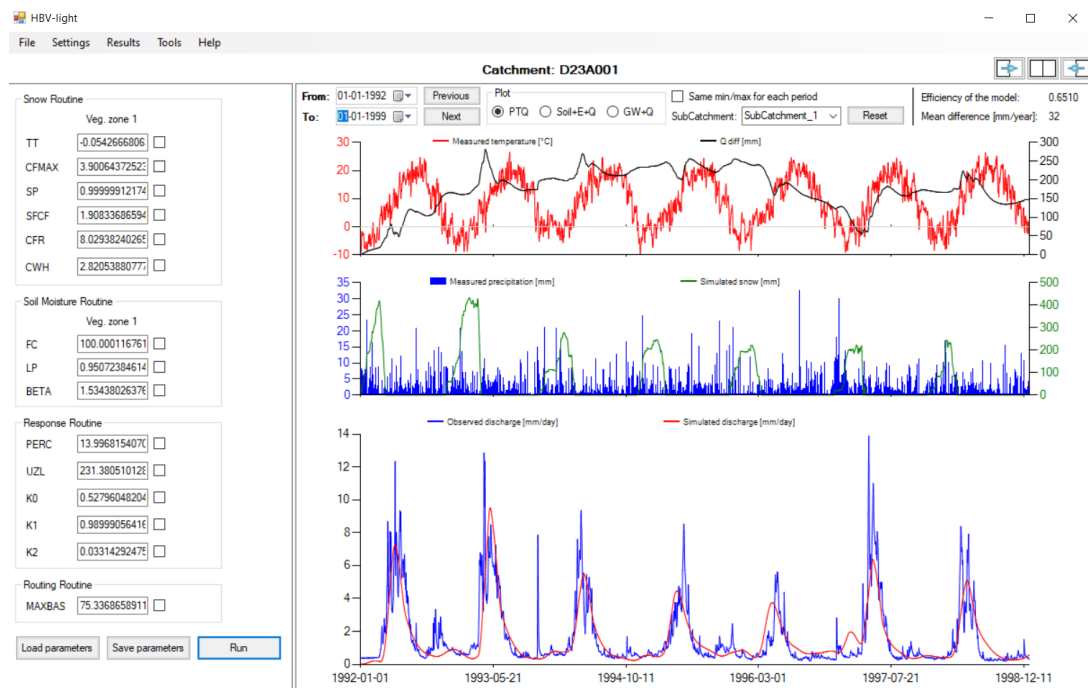


Figure 3-16 HBV-Light Graphical User Interface

3.5.2 HBV-R Model

The novel-developed HBV-R model represents a simplified version of the original HBV model translated from (Aghakouchak et al., 2013), adhering to similar principles. There are a total number of 12 parameters employed in its model. Given that the HBV model uses the Degree Day snow routine, which overlooks the transitional phase between rain and snow, a distinct approach becomes necessary (Çallı et al., 2022). This new snow routine was developed by Çallı et al. (2022) and Çallı (2023). Unlike the mentioned study, in this research, MODIS snow cover data is not used in the snow routine.

The total hydrological response to precipitation is computed by summing the snowmelt and rainfall. Subsequently, the actual evapotranspiration is determined using the permanent wilting point as the threshold, with the same equation as the HBV model.

Moving on to the soil and groundwater routines, vertical percolation from soil to shallow groundwater storage is evaluated based on the k_0 , k_1 , k_2 , and k_p parameters. The initial parameter, k_0 , manages the rapid response mechanism at the reservoir's upper portion. The second parameter, k_1 , dictates the flow from the intermediate reservoir to the runoff, while the third parameter, k_2 , governs the flow from the deep reservoir to the runoff. Lastly, the K_p parameter signifies the vertical percolation's conductivity from the upper to the deep reservoir.

Unlike the HBV model, the HBV-R model lacks a routing routine, and neither vegetation nor elevation factors are incorporated. However, it differentiates by including a mixed phase of precipitation, using Latin Hypercube Sampling (LHS) instead of Genetic Algorithm and Powell (GAP) optimization. Most importantly, the HBV-R model has open-source code.

3.5.3 HBV-Light and HBV-R Parameters

The HBV-light model encompasses 14 parameters dedicated to the catchment and an additional 11 parameters specific to vegetation zones. Whereas the HBV-R model only has 12 parameters. The details of the parameters are given below.

Table 3-4 Parameters of HBV-R and HBV-Light Model

HBV-Light	HBV-R	Unit	Valid Range	Description	Function	Calibrated	Parameter Type
PERC	-	mm/ Δt	[0,inf)	Threshold parameter	Response Function	Yes	Catchment Zone
Alpha	-	-	[0,inf)	non-linearity coefficient	Response Function	No	Catchment Zone
UZL	L	mm	[0,inf)	Threshold parameter	Response Function	Yes	Catchment Zone
K0	K0	1/ Δt	[0,1)	storage(or recession) coefficient 0	Response Function	Yes	Catchment Zone
K1	K1	1/ Δt	[0,1)	storage(or recession) coefficient 1	Response Function	Yes	Catchment Zone
K2	K2	1/ Δt	[0,1)	storage(or recession) coefficient 2	Response Function	Yes	Catchment Zone
-	Kp	1/ Δt	[0,1)	Percolation Conductivity	Response Function	Yes	Catchment Zone
MAXBAS	-	Δt	[1,100]	length of triangular weighting function	Routing Routine	Yes	Catchment Zone
Cet	-	1/ $^{\circ}$ C	[0,1)	potential evaporation correction factor	Evaporation	No	Catchment Zone
PCALT	-	%/100m	(-inf,inf)	increase of precipitation with elevation	Height Increment Variables	No	Catchment Zone
TCALT	-	$^{\circ}$ C/100m	(-inf,inf)	decrease of temperature with elevation	Height Increment Variables	No	Catchment Zone
Pelev	-	m	(-inf,inf)	elevation of precipitation	Height Increment Variables	No	Catchment Zone
Telev	-	m	(-inf,inf)	elevation of temperature	Height Increment Variables	No	Catchment Zone
PART	-	-	[0,1)	portion of the recharge which is added to groundwater box 1	Response Routine with Delay	No	Catchment Zone
DELAY	-	Δt	[0,inf)	time period over which recharge is evenly distributed	Response Routine with Delay	No	Catchment Zone
TT	Ts	$^{\circ}$ C	(-inf,inf)	Threshold Temperature	Snow Routine	Yes	Vegetation Zone
-	Tm	$^{\circ}$ C	(-inf,inf)	Snowmelt Temperature	Snow Routine	Yes	Vegetation Zone
-	Tr	$^{\circ}$ C	(-inf,inf)	Minimum Rain Temperature	Snow Routine	Yes	Vegetation Zone
CFMAX	DDF	mm/ Δt $^{\circ}$ C	[0,inf)	degree - Δt factor	Snow Routine	Yes	Vegetation Zone
SP	-	-	[0,1)	seasonal variability in degree- Δt factor	Snow Routine	Yes	Vegetation Zone
SFCF	-	-	[0,inf)	snowfall correction factor	Snow Routine	Yes	Vegetation Zone
CFR	-	-	[0,inf)	refreezing coefficient	Snow Routine	Yes	Vegetation Zone
CWH	-	-	[0,inf)	Water holding capacity	Snow Routine	Yes	Vegetation Zone
CFGlacier	-	-	[0,inf)	glacier correction factor	Glacier Model	No	Vegetation Zone
CFslope	-	-	(0,inf)	Slope correction factor	Aspect Model, Glacier Model	No	Vegetation Zone
FC	FC	mm	(0,inf)	maximum soil moisture storage	Soil Moisture Routine	Yes	Vegetation Zone
LP	-	-	[0,1)	soil moisture value above which AET reaches PET	Soil Moisture Routine	Yes	Vegetation Zone
-	pwp	-	[0,1)	Permanent Wilting Point	Soil Moisture Routine	Yes	Vegetation Zone
BETA	BETA	-	(0,inf)	Parameter that determines the relative contribution to runoff from rain or snowmelt	Soil Moisture Routine	Yes	Vegetation Zone

3.6 Model Calibration and Validation

The HBV model's parameters cannot be measured in the field. They must be determined by calibration. To find the correct parameters to best fit the measured runoffs to represent the study area accurately. Calibration could be done manually by trial and error or automatically. There are different criteria used while calibrating. One is a visual inspection of the observed and simulated plots, and the other uses statistical criteria. In this study, automatic calibration is done, and Nash-Sutcliffe's (Nash & Sutcliffe, 1970) efficiency coefficient is used.

The calibration process necessitates including various hydrological events within the calibration period. A split-sample test is conducted for this process, evaluating the model's performance using calibrated parameters in an independent period. In the study, data is split into two: the calibration period and the validation period. Each phase plays a crucial role in ensuring the reliability and accuracy of the model's predictions. Each stage is essential to guarantee the dependability and accuracy of the model's predictions. Seibert (2005) suggests that a calibration period of 5 to 10 years is adequate for the model. In the research, a year is assumed to be 360 days, and all the datasets start on the 1st of January and end on the 30th of December. The calibration and validation periods for each dataset used in the research are given in Table 3-5.

Table 3-5 Calibration and Validation Periods for each Sub-Basin

Sub-Basin	MODELS WITH ERA5 -LAND		MODELS WITH GCMs		MODELS WITH TRMM 3B42	Elev. (m)	Area (km ²)
	Training Period	Validation Period	Training Period	Validation Period	Validation Period		
D23A001	1992 - 1999	2000 - 2005	1992 - 1997	1998 - 2000	1998 - 2005	310	1680
D23A003	1998 - 2002	2003 - 2005	-	-	1998 - 2005	1562	162
D23A016	1999 - 2002	2003 - 2005	-	-	1999 - 2006	1805	481.2
D23A026	1980 - 1995	1996 - 2001	1980 - 1994	1995 - 2000	2004 - 2015	1850	110
D23A031	1986 - 1999	2000 - 2005	1986 - 1996	1997 - 2000	1998 - 2007	1740	60.01
D23A032	1986 - 1999	2000 - 2005	1986 - 1996	1997 - 2000	1998 - 2006	1740	153.5
D23A037	1991 - 1999	2000 - 2005	1991 - 1997	1998 - 2000	1998 - 2005	1625	207.6
E23A004	1980 - 1999	2000 - 2005	1980 - 1994	1995 - 2000	1998 - 2010	1545	1734
E23A005	1980 - 1999	2000 - 2005	1980 - 1994	1995 - 2000	1998 - 2010	654	7272
E23A016	1980 - 1999	2000 - 2005	1980 - 1994	1995 - 2000	1998 - 2015	1170	5505.2
E23A020	1993 - 2001	2002 - 2005	1993 - 1997	1998 - 2000	1998 - 2010	1365	4759.2
E23A021	1980 - 1999	2000 - 2005	1980 - 1994	1995 - 2000	1998 - 2010	705	586
E23A022	1980 - 1991	1992 - 1999	1980 - 1993	1994 - 1999	-	201	18326
E23A023	1980 - 1991	1992 - 2002	1980 - 1994	1995 - 2000	1998 - 2002	572	6854
E23A025	1991 - 2000	2001 - 2005	-	-	-	1129	1762
E23A026	1982 - 1993	1994 - 1997	1982 - 1992	1993 - 1997	1998 - 2010	875	250.7
E23A027	1982 - 1993	1994 - 1997	1982 - 1992	1993 - 1997	2006 - 2015	570	1216.4
E23A028	1982 - 1999	2000 - 2005	1982 - 1994	1995 - 2000	1998 - 2009	365	546.8
E23A029	1982 - 1999	2000 - 2005	1982 - 1994	1995 - 2000	1998 - 2011	1004	3518.5
E23A030	1982 - 1999	2000 - 2005	1982 - 1994	1995 - 2000	1998 - 2010	995	113.6
E23A031	1988 - 1995	1996 - 1999	1988 - 1995	1996 - 1999	1998 - 1999	560	99.7
E23A033	1994 - 2001	2002 - 2005	1994 - 1997	1998 - 2000	1998 - 2010	830	367.5
E23A034	1990 - 2000	2001 - 2005	1990 - 1997	1998 - 2000	1998 - 2010	366	1472.6
E23A035	1993 - 2001	2002 - 2005	1993 - 1997	1998 - 2000	1998 - 2010	435	15687
E23A036	1993 - 2001	2002 - 2005	1993 - 1997	1998 - 2000	1998 - 2006	805	541.3
E23A037	1990 - 2000	2001 - 2005	1990 - 1997	1998 - 2000	1998 - 2010	892	6634.2
E23A038	1993 - 2001	2002 - 2005	1993 - 1997	1998 - 2000	1998 - 2010	1265	5168.1
E23A039	1991 - 1994	1995 - 1998	-	-	-	213	297.7
E23A040	1992 - 2000	2001 - 2005	1992 - 1997	1998 - 2000	1998 - 2010	682	202
E23A042	1993 - 2000	2001 - 2005	1993 - 1997	1998 - 2000	1998 - 2010	1122	318.4

3.6.1 HBV-Light Calibration

The automatic calibration could be done using Monte Carlo simulation, batch simulation, and GAP optimization methods. These methods also could be found in the HBV-Light program. In this study, GAP optimization is conducted. The calibration process employs the GAP optimization tool, which combines a genetic algorithm for approximating the optimization solution (Seibert, 2000) and Powell's

quadratically convergent method for local optimization(Press, 1992). One or more populations of 50 randomly generated parameter sets within specified ranges are created initially. These parameter sets undergo evaluation by running the model, and their goodness of fit is determined based on the objective function. Sets with better performance are assigned a higher probability of generating new sets, while those yielding poorer results are less likely to generate new sets (Seibert, 2000).

The screenshot displays the 'GAP optimization' interface with the following sections and values:

- Population Settings:**
 - Number of parameter sets: 50
 - Number of populations: 1
 - Frequency of exchange: 0
 - Number of PSs which exchange: 0
- Reproduction Settings:**
 - Probability for optimization between sets: 0.01
 - Probability for mutation: 0.02
 - Probability for optimized value: 0
 - Probability for random value between the old values: 0.16
 - Probability for taking one of the old values: 0.82
 - Portion of range for small change (if random between and both values equal): 0
 - Value of C: 2
- Model Settings:**
 - No of model runs: 5000
 - No of runs for local optimization (Powell): 1000
 - Calibrate 100 times
- Goodness of Fit Measure:**
 - Population: Population_1
 - Table:

Obj. Function	Weight
Reff	0.9
LogReff	0.1
- Vegetation zone parameters:**

Parameter	Lower Limit	Upper Limit
TT	-1	5
CFMAX	0.01	4
SP	0	1
SFCF	0.1	5
CFR	0	0.05
CWH	0	5
FC	100	400
LP	0.1	1
BETA	1	8
- Catchment parameters:**

Parameter	Lower Limit	Upper Limit
PERC	0	100
UZL	0	700
K0	0.0001	0.99
K1	0.0001	0.99
K2	0.0001	0.99
MAXBAS	1	100
PCALT	10	10
TCALT	0.6	0.6
Elev. of P	310	310
Elev. of T	310	310

Figure 3-17 HBV-Light GAP Optimization Interface

The figure above shows the inputs that could be edited with the HBV-Light program. Parameter ranges for each sub-basin are adjusted manually. Model settings are 5000 model runs, which create sets for the genetic algorithm, and 1000 runs for fine-tuning for all calibrations. The reproduction settings for the genetic algorithm are left default, as shown in the figure. The objective function to be optimized is a combination of model efficiency (Reff), which is the Nash-Sutcliffe equation, and efficiency for Log(Q) (LogReff).

3.6.2 HBV-R Calibration

A distinct calibration strategy is adopted within this methodology, using the LHS method. While Monte Carlo Sampling (MCS) and Quasi-Monte Carlo Sampling (QMCS) offer robust ways to quantify uncertainty, their computational demands can be substantial (Dutta & Gandomi, 2020). To tackle this computational challenge, LHS provides a practical approach to reduce the requisite number of simulations while still capturing the uncertainty in responses. LHS employs a stratified sampling scheme involving dividing the input space into distinct "strata" or intervals and selecting a representative value from each interval. These representative values are combined to ensure comprehensive coverage of the simulation space, thereby minimizing redundancy.

According to the LHS method, a uniform probability distribution consists of 5 million rows for each parameter set for its ranges. The generated values are recorded, and NSE values are calculated for each parameter set. The parameter set with the highest NSE value is selected for the specific basin.

The process of generating random samples using the LHS scheme involves the following steps in detail:

Step 1: Partition the sample space of each random variable (RV) into L intervals, each with an equal probability of $1/L$. The division should not be based on equal probabilities; intervals can have varying probabilities.

Step 2: Generate one representative random sample from each interval. Occasionally, instead of a purely random sample, the midpoint value within the interval is selected as the representative.

Step 3: Randomly choose one value from the L values of each RV to create the first sample, denoted as s_1 .

Step 4: Randomly select one value from the remaining L-1 values of each RV to generate subsequent samples (s2 and beyond), repeating this process up to L samples (sL).

Step 5: Reiterate Steps 1 to 4 for all the RVs in the analysis.

Step 6: The subsequent sampling process remains consistent with the methodology employed in MCS.

LHS offers efficient sampling by capturing a broad spectrum of variability across input parameters using a comparatively smaller number of simulations than traditional MCS. This approach proves particularly advantageous when computational resources are constrained, rendering it a valuable tool for quantifying uncertainty in diverse scientific and engineering domains (Li & Yang, 2023). Different studies agree that LHS performs better than MCS (Abyani & Bahaari, 2020; Kucherenko et al., 2015).

3.7 Used Statistics

In the study, the results of the analysis are evaluated by statistical accuracy equations. These are Nash-Sutcliff equation, Root Mean Squared Error (RMSE), Coefficient of Determination (R^2) and Percent Bias.

$$RMSE = \sqrt{\frac{\sum_{i=1}^n (Q_i^{obs} - Q_i^{sim})^2}{n}}$$

$$R^2 = 1 - \frac{\sum_{i=1}^n (\hat{y}_i - y_i)^2}{\sum_{i=1}^n (y_i - \bar{y})^2}$$

$$PBIAS = \frac{\sum_{i=1}^n (Y_i^{obs} - Y_i^{sim})}{\sum_{i=1}^n (Y_i^{obs})}$$

$$NSE = 1 - \frac{\sum_{i=1}^n (Q_i^{obs} - Q_i^{sim})^2}{\sum_{i=1}^n (Q_i^{obs} - \bar{Q}^{obs})^2}$$

Q^{obs} stands for observed surface runoff, Q^{sim} is for simulated surface runoff and \bar{Q}^{obs} is the observed mean surface runoff.

According to Motovilov et al. (1999), a Nash-Sutcliffe Efficiency (NSE) value between 0.36 and 0.75 indicates a satisfactory model performance. An NSE value exceeding 0.75 signifies a well-performing model, while a value below 0.36 suggests less satisfactory performance. However, more than relying solely on one criterion is required to ensure the adequacy of the model's performance. Therefore, it is imperative to consider additional metrics such as Root Mean Square Error (RMSE), Coefficient of Determination (R^2), and bias.

The coefficient of determination, R^2 , approaching 1, signifies a stronger correlation within the data. Typically, RMSE values fall within the 0 to 1 range when dealing with datasets of more minor scales. If the RMSE value surpasses 1, it may indicate that the model's errors are relatively higher than the data's range. Nevertheless, given the larger scale of our dataset, an RMSE above one could be deemed acceptable if the errors remain within a reasonable range.

Regardless of the situation, more than relying solely on RMSE is required to interpret the model's performance definitively. Thus, it is also essential to compute the percentage bias. A percentage bias approximating 0 implies that the model's predictions are consistently balanced and unbiased on average.

CHAPTER 4

RESULTS AND DISCUSSION

4.1 Analysis of Dataset and Bias Correction

In this study, ERA5-Land is preferred due to the limited number of meteorological stations representing the sub-basins. Since the HBV model requires daily temperature and precipitation data, ERA5-Land obtains a continuous dataset, a reanalysis dataset combining observations and the law of physics: water and energy balance. Additionally, TRMM 3B42 data is utilized to assess the impact of remote-sensing data on the model. TRMM 3B42 data is selected as the primary source for remote sensing data due to its extensive long-term observation history. This research involves constructing, calibrating, and executing the HBV model using remote sensing data and ground observation stations.

The dataset has undergone bias correction using five well-established long-term gauge stations. First, normalization is carried out using the mean of the observations and corresponding values within the grid of the ERA5-Land and TRMM 3B42 datasets. The TRMM 3B42 and ERA5-Land datasets are adjusted through division by 1.973 and 1.98, respectively. Additionally, a value of 4.07 is added to the ERA5-Land temperature data.

Next, the GCMs are bias-corrected, with a bias-corrected ERA5-Land dataset. The graphs given below show before and after the bias correction.

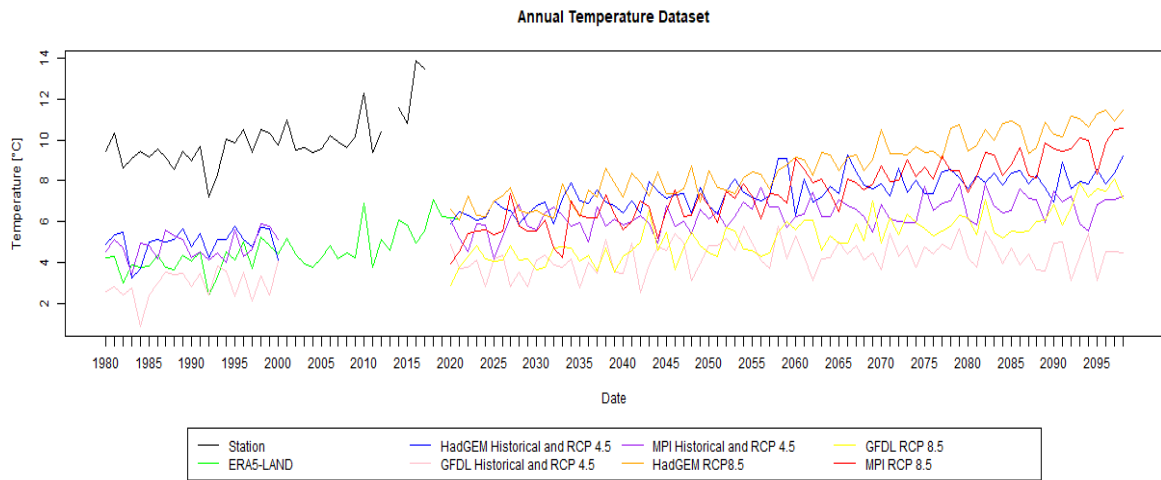


Figure 4-1 Annual Temperature Graph of the Dataset

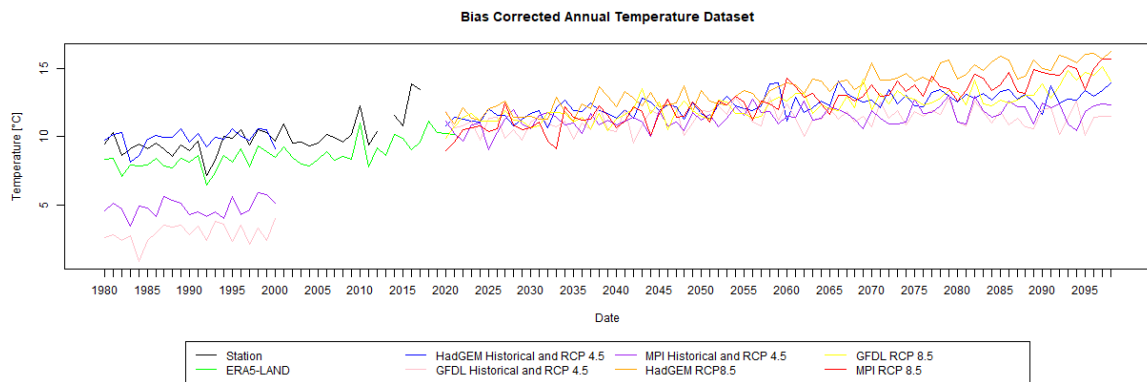


Figure 4-2 Graph of Annual Bias Corrected Temperature Data

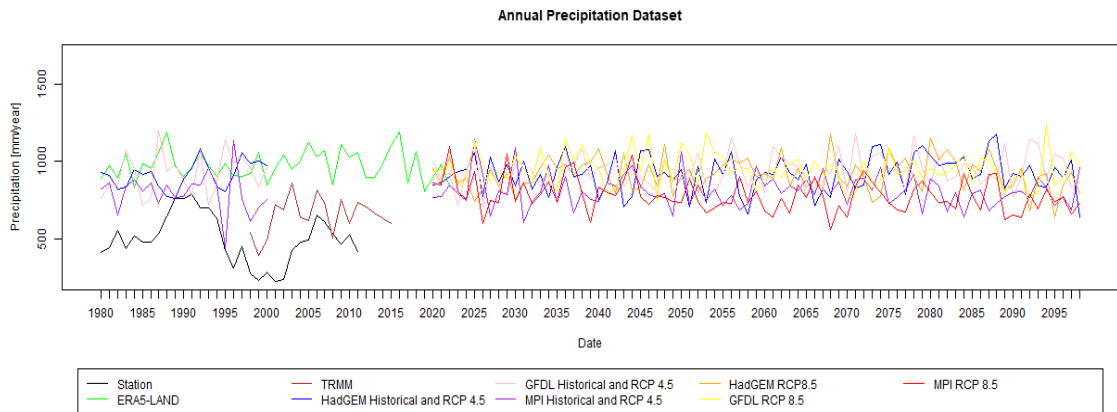


Figure 4-3 Annual Precipitation Graph of the Dataset

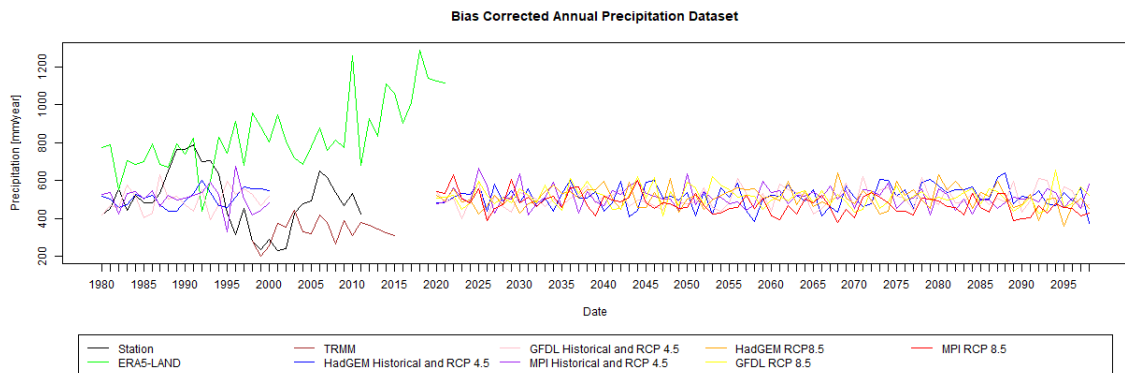


Figure 4-4 Graph of Annual Bias Corrected Precipitation Data

4.2 Analysis of Precipitation and Temperature

To enhance the dataset comprehension used in the model, annual averages of ERA5-Land, historical values of GCMs, TRMM 3B42, and future datasets of GCMs are calculated for each sub-basin. For this calculation, bias-corrected data is used. The precipitation and temperature variables are annually calculated as the GCMs ensemble mean is calculated for historical data, RCP 4.5 and RCP 8.5 separately for each sub-basin and divided into two periods between 2023-2060 (F1) and 2061-2098 (F2). The results are in Table 4-1 and Table 4-2 below.

The temperature increases significantly from the table comparing the values with Era5-Land data (E5L) and future projections. RCP 8.5 shows a more dramatic increase in temperature with a rise of around 3°C for the first 38 years and 5°C for the second half. On the other hand, RCP 4.5 increases around 2.5°C and 3°C, respectively.

Table 4-1 Annual Averages of The Temperature (°C)

Sub-Basin	RAW						CORRECTED						Change with ERA5-Land			
	E5L	GCM-Ensemble Mean					E5L	GCM-Ensemble Mean					(°C)			
		Hist	F1-4.5	F1-8.5	F2-4.5	F2-8.5		HIST	F1-4.5	F1-8.5	F2-4.5	F2-8.5	F1-4.5	F1-8.5	F2-4.5	F2-8.5
D23A001	5.1	5.0	6.6	7.0	7.2	9.0	9.2	7.9	9.5	10.0	10.1	11.9	0.3	0.8	0.9	2.7
D23A003	3.4	4.2	5.8	6.2	6.4	8.2	7.4	11.8	13.4	13.9	13.9	15.8	6.0	6.5	6.5	8.4
D23A016	1.5	2.4	4.1	4.6	4.7	6.6	5.5	10.4	12.1	12.5	12.7	14.6	6.6	7.0	7.2	9.1
D23A026	3.2	2.4	4.1	4.5	4.7	6.6	7.3	10.0	11.7	12.1	12.2	14.1	4.4	4.8	4.9	6.8
D23A031	4.1	3.4	5.1	5.5	5.7	7.6	8.1	9.9	11.6	12.0	12.2	14.2	3.4	3.8	4.1	6.0
D23A032	4.0	3.4	5.1	5.5	5.7	7.6	8.1	9.9	11.6	12.0	12.2	14.2	3.5	3.9	4.1	6.1
D23A037	2.2	3.5	5.1	5.6	5.7	7.6	6.2	8.4	10.0	10.4	10.7	12.6	3.8	4.2	4.5	6.4
E23A004	2.4	2.9	4.6	5.1	5.2	7.1	6.4	11.1	12.8	13.2	13.3	15.2	6.3	6.8	6.9	8.8
E23A005	0.1	3.5	5.1	5.6	5.7	7.6	4.2	10.8	12.5	12.9	13.0	14.9	8.3	8.7	8.8	10.7
E23A016	4.0	3.4	5.0	5.5	5.6	7.5	8.1	11.2	12.9	13.4	13.5	15.4	4.8	5.3	5.4	7.3
E23A020	3.7	3.5	5.2	5.6	5.8	7.7	7.8	11.4	13.1	13.5	13.6	15.5	5.3	5.7	5.8	7.7
E23A021	4.1	4.4	5.9	6.4	6.5	8.4	8.2	10.0	11.7	12.1	12.2	13.9	3.5	4.0	4.0	5.8
E23A022	4.0	3.7	5.3	5.7	5.9	7.8	8.0	9.7	11.4	11.8	11.9	13.8	3.4	3.8	3.9	5.8
E23A023	3.1	3.6	5.2	5.7	5.9	7.7	7.2	8.5	10.2	10.6	10.8	12.7	3.0	3.4	3.6	5.5
E23A025	3.0	3.9	5.6	6.0	6.2	8.1	7.1	8.1	9.8	10.2	10.4	12.3	2.7	3.1	3.3	5.2
E23A026	4.2	5.0	6.6	7.0	7.2	9.0	8.3	7.9	9.5	10.0	10.1	11.9	1.3	1.7	1.8	3.6
E23A027	4.0	5.0	6.6	7.0	7.2	9.0	8.1	7.9	9.5	10.0	10.1	11.9	1.5	1.9	2.0	3.8
E23A028	4.5	4.3	5.8	6.3	6.4	8.3	8.6	7.8	9.4	9.8	10.0	11.8	0.8	1.2	1.4	3.3
E23A029	4.1	3.3	4.9	5.4	5.5	7.4	8.1	8.0	9.7	10.1	10.3	12.2	1.5	1.9	2.1	4.0
E23A030	5.0	2.8	4.4	4.9	5.1	6.9	9.1	10.0	11.7	12.2	12.3	14.1	2.6	3.1	3.2	5.0
E23A031	4.1	5.3	6.9	7.3	7.4	9.2	8.1	8.6	10.1	10.5	10.7	12.5	2.0	2.4	2.5	4.3
E23A033	3.1	5.0	6.6	7.0	7.2	9.0	7.2	7.9	9.5	10.0	10.1	11.9	2.4	2.8	2.9	4.7
E23A034	4.0	5.0	6.6	7.0	7.2	9.0	8.1	7.9	9.5	10.0	10.1	11.9	1.5	1.9	2.0	3.9
E23A035	4.1	3.6	5.2	5.6	5.8	7.7	8.1	9.9	11.6	12.0	12.1	14.0	3.5	3.9	4.0	5.9
E23A036	4.9	4.4	5.9	6.4	6.5	8.4	9.0	10.0	11.7	12.1	12.2	13.9	2.7	3.1	3.2	5.0
E23A037	6.5	3.2	4.9	5.3	5.5	7.4	10.5	11.0	12.6	13.1	13.2	15.1	2.1	2.6	2.7	4.5
E23A038	1.1	3.4	5.0	5.5	5.6	7.5	5.2	11.2	12.9	13.4	13.5	15.4	7.7	8.2	8.3	10.2
E23A039	3.3	6.6	8.1	8.5	8.6	10.3	7.3	10.0	11.5	11.9	12.0	13.8	4.2	4.6	4.7	6.4
E23A040	4.7	4.4	5.9	6.4	6.5	8.4	8.7	10.0	11.7	12.1	12.2	13.9	2.9	3.4	3.4	5.2
E23A042	4.8	3.8	5.5	5.9	6.1	7.9	8.9	10.0	11.7	12.2	12.2	14.0	2.8	3.3	3.4	5.2
Çoruh	4.8	4.1	5.7	6.2	6.3	8.2	8.9	9.8	11.4	11.8	12.0	13.8	2.5	2.9	3.1	4.9

A comparison between the Era5-Land dataset and the ensemble mean of historical GCMs reveals subtle variations in rainfall patterns. Specifically, it indicates a modest increase in precipitation levels within the context of RCP 4.5 scenarios. In contrast, under the RCP 8.5 scenario, there is a slight increase during the initial period, followed by a notable decline in the subsequent period. In the RCP 4.5 scenario with

the corrected values, the growth is approximately 2.4%. However, the RCP 8.5 method shows a similar increase in rainfall in the Çoruh Basin, with a 2.4% in the first half and a 2.8% decrease in the second half of future projections. Comparing the historical precipitation dataset, TRMM 3B42 is comparatively lower.

Table 4-2 Annual Averages of The Precipitation (mm/year)

Sub-Basin	RAW								CORRECTED								Change with ERA5-Land (mm/year)			
	ESL	TRMM	GCM-Ensemble Mean						ESL	TRMM	GCM-Ensemble Mean						F1-4.5	F1-8.5	F2-4.5	F2-8.5
			Hist	F1-4.5	F1-8.5	F2-4.5	F2-8.5	HIST			F1-4.5	F1-8.5	F2-4.5	F2-8.5						
D23A001	1402	1176	1025	1046	1088	1114	1086	708	605	644	655	670	689	664	-53	-39	-19	-44		
D23A003	962	461	792	803	803	823	798	486	237	432	438	429	445	421	-47	-56	-41	-65		
D23A016	1511	922	712	700	719	719	695	763	474	350	343	349	351	335	-420	-415	-412	-428		
D23A026	1230	922	743	735	726	724	692	621	474	471	462	448	456	426	-159	-173	-165	-196		
D23A031	693	553	744	743	739	729	698	350	285	397	396	388	390	367	46	38	40	17		
D23A032	679	556	744	743	739	729	698	343	286	397	396	388	390	367	53	45	47	24		
D23A037	738	922	763	765	764	774	743	373	474	315	316	312	319	301	-57	-61	-54	-72		
E23A004	714	632	741	726	739	742	709	361	325	324	318	321	324	306	-43	-40	-37	-54		
E23A005	784	922	770	763	771	773	744	396	474	430	426	423	429	405	30	27	33	9		
E23A016	755	677	745	738	747	756	725	382	348	369	366	364	372	351	-16	-17	-9	-30		
E23A020	1494	444	754	748	755	766	731	755	229	371	368	366	374	352	-387	-389	-380	-403		
E23A021	766	634	648	668	672	669	668	387	326	587	602	594	599	580	215	207	212	193		
E23A022	786	544	810	809	821	827	800	397	280	434	433	432	440	418	36	35	42	21		
E23A023	649	573	805	804	815	823	799	328	295	379	377	377	384	366	50	50	57	39		
E23A025	664	584	790	794	804	815	787	335	300	336	338	338	346	329	3	3	10	-7		
E23A026	863	563	1025	1046	1088	1114	1086	436	290	644	655	670	689	664	219	234	253	228		
E23A027	744	665	1025	1046	1088	1114	1086	376	342	644	655	670	689	664	279	294	313	288		
E23A028	1105	449	1245	1257	1299	1307	1274	558	231	513	515	525	532	514	-43	-33	-26	-44		
E23A029	880	536	848	841	857	870	841	445	276	371	367	370	378	360	-78	-75	-67	-85		
E23A030	1798	1176	1480	1451	1455	1428	1379	908	605	691	672	656	660	619	-236	-252	-248	-289		
E23A031	818	584	1376	1387	1434	1447	1409	413	301	814	819	827	843	809	406	414	430	396		
E23A033	1554	444	1025	1046	1088	1114	1086	785	229	644	655	670	689	664	-130	-116	-96	-121		
E23A034	751	548	1025	1046	1088	1114	1086	379	282	644	655	670	689	664	275	290	310	284		
E23A035	686	556	776	773	782	786	760	347	286	419	417	415	422	400	71	68	75	53		
E23A036	1557	922	648	668	672	669	668	786	474	587	602	594	599	580	-184	-193	-187	-206		
E23A037	2274	359	827	817	824	827	794	1148	185	416	410	406	413	389	-738	-742	-735	-759		
E23A038	763	609	745	738	747	756	725	385	313	369	366	364	372	351	-20	-21	-13	-34		
E23A039	1083	526	1787	1785	1813	1846	1739	547	271	1084	1076	1066	1102	1025	528	519	554	478		
E23A040	1103	449	648	668	672	669	668	557	231	587	602	594	599	580	45	36	42	22		
E23A042	1136	435	882	880	888	875	856	574	224	605	605	597	601	572	31	23	27	-2		
Çoruh	994	662	878	879	894	902	871	502	341	505	507	507	517	491	5	5	15	-11		

The table below presents a comparative analysis with a prior study. This study predicts an increase in both precipitation and temperature for future periods. Although the findings align with the previous research regarding temperature trends, it's worth noting that the projected precipitation increase in this study is comparatively lower.

Table 4-3 Comparison of the Dataset with Other Study

Source	Precipitation				Temperature			
	Historical Period	mm/year	Future period	Change	Historical Period	°C	Future period	Change
SYGM (2020)	1971-2000	616.8	2071-2100	+ 10%	1971-2000	8.5	2071-2100	min +2 °C max +5.4°C
This Study (2023)	1980-2022	502	2023-2099	+ 2.4%	1980-2022	8.9	2023-2099	min +2.5 °C max +5 °C

4.3 Historical Period Simulations of HBV Models

HBV models have been configured based on the availability of runoff observations. Moreover, to mitigate potential external influences on the model, such as those posed by dam operations, the validation period has been limited until 2005, coinciding with the starting year of the first dam's operation within the Çoruh Basin. Due to data limitations within specific basins, there exists variability in both the training and validation dates. GCMs historical dataset is between 1971 and 2000. However, the runoff data in that period is unavailable for each sub-basin, so some sub-basins are disregarded in GCM historical HBV modeling. The divided periods for each sub-basin can be seen in Table 3-5.

According to the periods ERA5-Land data and three different GCM, GAP optimization has been calibrated using HBV-Light. HBV-R model calibration is only conducted on the ERA5-Land dataset with the Latin Hypercube Sampling method. The parameters obtained from the analyses are given in appendices.

After calibrating the models, the simulated and observed runoff values were subjected to statistical analysis for verification. Statistical accuracy measures the Nash-Sutcliffe Equation, Coefficient of Determination, and Percentage Bias, calculated for each sub-basin. A comparative view of HBV-Light and HBV-R calibration statistics is given in Table 4-4.

Table 4-4 Calibration Statistics for HBV-Light and HBV-R Model for ERA5-Land

Sub-Basins	HBV-LIGHT ERA5-LAND CALIBRATION						HBV-R ERA5-LAND CALIBRATION					
	Qobs (m ³ /s)	Qsim (m ³ /s)	NSE	RMSE (m ³ /s)	R ²	Bias (%)	Qsim (m ³ /s)	NSE	RMSE (m ³ /s)	R ²	Bias (%)	
D23A001	30.58	28.86	0.65	1.14	0.65	-5.61	28.69	0.71	20.10	0.72	-6.20	
D23A003	2.49	2.17	0.62	1.25	0.63	-13.14	1.97	0.74	1.93	0.76	-20.99	
D23A016	4.56	4.44	0.62	0.46	0.62	-2.64	3.76	0.47	3.06	0.52	-17.56	
D23A026	1.90	1.88	0.65	1.05	0.65	-1.03	1.85	0.75	1.14	0.75	-2.69	
D23A031	1.25	1.19	0.73	1.29	0.73	-5.07	1.04	0.74	0.88	0.75	-16.61	
D23A032	2.33	2.32	0.52	1.07	0.52	-0.46	2.31	0.63	1.65	0.63	-0.97	
D23A037	1.50	1.43	0.82	0.44	0.82	-4.66	1.25	0.77	1.20	0.78	-16.78	
E23A004	15.82	15.35	0.58	0.60	0.59	-3.00	14.89	0.73	9.65	0.73	-5.91	
E23A005	71.10	69.47	0.71	0.53	0.71	-2.29	67.48	0.80	36.68	0.81	-5.08	
E23A016	39.73	38.39	0.64	0.45	0.64	-3.36	37.65	0.76	23.57	0.76	-5.24	
E23A020	27.60	29.02	0.57	0.43	0.58	5.14	24.95	0.65	21.44	0.66	-9.63	
E23A021	13.96	12.49	0.67	1.23	0.68	-10.53	11.23	0.70	7.97	0.73	-19.56	
E23A022	162.83	158.71	0.72	0.45	0.72	-2.53	159.23	0.79	81.08	0.80	-2.22	
E23A023	34.83	35.05	0.55	0.36	0.56	0.64	33.37	0.67	24.86	0.68	-4.20	
E23A025	6.67	6.58	0.55	0.31	0.55	-1.48	6.20	0.67	5.44	0.67	-7.15	
E23A026	8.85	6.71	0.62	2.75	0.68	-24.15	6.77	0.57	8.51	0.60	-23.59	
E23A027	22.75	20.80	0.57	1.25	0.58	-8.56	21.60	0.62	16.73	0.62	-5.07	
E23A028	6.10	5.89	0.65	0.75	0.65	-3.41	5.50	0.73	4.20	0.74	-9.82	
E23A029	16.80	16.02	0.59	0.38	0.60	-4.64	15.60	0.68	13.56	0.68	-7.09	
E23A030	2.96	2.77	0.57	1.63	0.57	-6.44	3.02	0.65	1.94	0.65	1.99	
E23A031	5.37	3.22	0.33	4.80	0.45	-40.12	4.60	0.46	4.97	0.48	-14.35	
E23A033	5.24	5.12	0.60	0.71	0.60	-2.27	5.35	0.70	2.61	0.71	2.22	
E23A034	25.60	23.74	0.67	0.97	0.68	-7.26	24.42	0.73	15.13	0.73	-4.65	
E23A035	107.63	104.60	0.72	0.36	0.72	-2.81	96.81	0.82	52.64	0.82	-10.07	
E23A036	12.41	11.81	0.67	1.22	0.68	-4.87	12.15	0.69	7.42	0.69	-2.10	
E23A037	54.92	67.34	0.50	0.60	0.54	22.63	92.28	0.15	60.07	0.50	68.01	
E23A038	31.15	31.37	0.73	0.36	0.73	0.72	29.99	0.79	19.20	0.79	-3.72	
E23A039	13.77	9.66	0.36	3.29	0.44	-29.86	9.76	0.34	11.50	0.43	-29.12	
E23A040	2.83	2.77	0.60	1.09	0.60	-2.25	2.85	0.66	2.36	0.66	0.66	
E23A042	9.05	8.60	0.71	1.45	0.71	-4.90	8.67	0.63	6.05	0.64	-4.24	
Mean	24.75	24.26	0.62	1.09	0.63	-5.61	24.51	0.66	15.58	0.68	-6.06	
Median	13.09	10.73	0.62	0.86	0.63	-3.39	10.50	0.69	8.24	0.70	-5.57	

The data presented in Table 4-4 reveals that the NSE and R² values of the model fall within a satisfactory range across most of the basins. Furthermore, the RMSE and percentage bias demonstrate acceptable levels. Additionally, the simulated runoff exhibits a high degree of similarity.

The NSE value of 0.66 falls within a satisfactory range in HBV-R, indicating a reasonable level of model performance. Moreover, the coefficient of determination provides favorable results, further affirming the model's quality. However, it is worth noting that the RMSE value appears notably high at approximately 15.6, suggesting

a degree of discrepancy between the model's predictions and the observed data. On a positive note, the bias value of -6.06 is considerably acceptable, signifying that the model's predictions are balanced and unbiased on average. These findings underscore the model's ability to capture the observed data's essential characteristics while highlighting areas for potential improvement, particularly in reducing the observed RMSE.

Table 4-5 Calibration Statistics for HBV-Light Model for GCMs

Sub-Basins	HADGEM						GFDL						MPI					
	Qobs (m ³ /s)	Qsim (m ³ /s)	NSE	RMSE (m ³ /s)	R ²	Bias (%)	Qsim (m ³ /s)	NSE	RMSE (m ³ /s)	R ²	Bias (%)	Qsim (m ³ /s)	NSE	RMSE (m ³ /s)	R ²	Bias (%)		
D23A001	31.86	29.95	0.66	1.91	0.66	-6.00	29.69	0.53	1.38	0.53	-6.80	29.17	0.59	1.29	0.59	-8.43		
D23A026	2.81	2.76	0.54	0.05	0.55	-1.91	2.75	0.59	1.15	0.59	-2.11	2.79	0.71	0.96	0.71	-0.85		
D23A031	10.28	9.22	0.59	1.06	0.60	-10.28	9.51	0.55	1.71	0.56	-7.53	10.19	0.65	1.50	0.66	-0.86		
D23A032	1.65	1.60	0.51	0.06	0.51	-3.38	1.35	0.11	1.35	0.13	-18.13	1.65	0.38	1.19	0.38	0.13		
D23A037	0.45	0.47	0.63	0.02	0.63	5.01	0.41	0.73	0.58	0.74	-8.70	0.46	0.63	0.68	0.63	3.07		
E23A004	1.39	1.34	0.46	0.05	0.47	-3.49	1.33	0.56	0.59	0.57	-4.49	1.35	0.55	0.60	0.56	-2.82		
E23A005	2.04	1.89	0.54	0.15	0.55	-7.21	1.99	0.70	0.54	0.70	-2.14	2.02	0.56	0.65	0.56	-0.79		
E23A016	12.45	11.90	0.48	0.56	0.49	-4.46	12.72	0.64	0.44	0.64	2.13	11.89	0.57	0.48	0.57	-4.53		
E23A020	44.08	45.42	0.49	1.35	0.49	3.06	46.52	0.73	0.37	0.74	5.53	47.01	0.51	0.45	0.52	6.66		
E23A021	131.92	121.11	0.52	10.81	0.53	-8.20	123.69	0.66	1.24	0.66	-6.24	124.50	0.60	1.34	0.61	-5.62		
E23A022	44.09	43.30	0.52	0.78	0.52	-1.78	42.88	0.60	0.56	0.60	-2.74	44.21	0.56	0.58	0.57	0.27		
E23A023	3.01	3.02	0.32	0.01	0.33	0.32	2.95	0.55	0.36	0.55	-2.27	2.96	0.44	0.40	0.45	-1.82		
E23A026	235.24	212.20	0.54	23.04	0.54	-9.79	227.00	0.55	2.88	0.55	-3.50	210.40	0.45	3.17	0.46	-10.56		
E23A027	32.36	30.85	0.47	1.52	0.48	-4.68	32.17	0.54	1.28	0.54	-0.60	31.12	0.43	1.42	0.43	-3.85		
E23A028	2.93	2.81	0.59	0.12	0.59	-4.20	2.97	0.56	0.88	0.56	1.33	2.88	0.63	0.81	0.63	-1.75		
E23A029	6.00	5.69	0.39	0.31	0.39	-5.16	6.26	0.46	0.45	0.46	4.39	6.08	0.42	0.46	0.42	1.34		
E23A030	14.95	14.29	0.63	0.66	0.63	-4.43	13.30	0.60	1.60	0.62	-11.04	14.19	0.70	1.39	0.70	-5.12		
E23A031	189.66	156.04	0.43	33.62	0.45	-17.73	162.35	0.40	4.57	0.41	-14.40	149.69	0.36	4.71	0.39	-21.07		
E23A033	1.58	1.57	0.61	0.62	0.61	-0.78	1.43	0.78	0.56	0.78	-9.73	1.54	0.67	0.66	0.68	-2.94		
E23A034	1.76	1.64	0.67	0.12	0.67	-6.63	1.76	0.51	1.21	0.51	-0.19	1.76	0.58	1.12	0.58	0.12		
E23A035	2.65	2.68	0.63	0.03	0.64	1.31	2.65	0.72	0.38	0.72	0.04	2.80	0.65	0.43	0.65	5.72		
E23A036	33.62	31.65	0.68	1.38	0.69	-5.86	30.63	0.70	1.16	0.70	-8.88	31.31	0.63	1.35	0.64	-6.88		
E23A037	130.69	122.53	0.72	8.17	0.72	-6.25	130.74	0.72	0.43	0.73	0.03	123.36	0.60	0.52	0.60	-5.61		
E23A038	3.37	3.61	0.54	0.24	0.55	7.25	3.69	0.77	0.33	0.77	9.67	3.69	0.51	0.49	0.52	9.66		
E23A040	71.58	71.55	0.59	0.04	0.59	-0.05	68.28	0.67	0.99	0.67	-4.62	69.10	0.53	1.173	0.53	-3.47		
E23A042	8.82	7.52	0.69	1.30	0.69	-14.75	7.34	0.66	1.85	0.67	-16.84	8.11	0.67	1.81	0.67	-8.09		
Mean	39.28	36.02	0.55	3.38	0.56	-4.23	37.17	0.60	1.11	0.60	-4.15	35.93	0.56	1.14	0.57	-2.62		
Median	9.55	8.37	0.54	0.59	0.55	-4.45	8.42	0.60	0.94	0.61	-3.12	9.15	0.58	0.88	0.58	-2.32		

Within GCMs in calibration, the simulated runoff average exhibits a comparable trend. The Nash-Sutcliffe Efficiency (NSE) values are nearly equivalent between the MPI and HadGEM and slightly improved for the GFDL. The Coefficient of Determination (R²) yields similar results across all three models; however, the Root Mean Square Error (RMSE) significantly surpasses typical levels in the case of the

Hadley Global Environment Model (HADGEM), in contrast to the other models. Moreover, when considering bias, MPI demonstrates markedly superior performance compared to the rest.

Table 4-6 Validation Statistics for HBV-Light and HBV-R Model for ERA5-Land

Sub-Basins	HBV-LIGHT ERA5-LAND VALIDATION						HBV-R ERA5-LAND VALIDATION				
	Qobs (m ³ /s)	Qsim (m ³ /s)	NSE	RMSE (m ³ /s)	R ²	Bias (%)	Qsim (m ³ /s)	NSE	RMSE (m ³ /s)	R ²	Bias (%)
D23A001	32.63	27.00	0.59	1.19	0.65	-17.25	28.69	0.69	20.02	0.71	-12.09
D23A003	2.50	2.46	0.74	1.07	0.63	-1.74	2.10	0.69	2.16	0.71	-15.84
D23A016	6.20	4.50	0.38	0.88	0.62	-27.37	3.78	0.52	4.33	0.69	-39.00
D23A026	1.80	1.54	0.47	1.24	0.65	-14.34	1.74	0.68	1.22	0.68	-3.24
D23A031	1.34	1.12	0.63	1.52	0.73	-16.64	0.95	0.58	1.13	0.64	-29.03
D23A032	2.26	2.17	0.38	0.96	0.52	-4.14	2.20	0.62	1.33	0.64	-2.72
D23A037	1.40	1.43	0.27	0.73	0.82	2.15	1.33	0.58	1.34	0.63	-5.47
E23A004	14.65	15.23	0.42	0.64	0.59	3.95	15.09	0.75	8.50	0.75	2.94
E23A005	66.09	65.67	0.60	0.57	0.71	-0.63	64.34	0.76	36.65	0.76	-2.66
E23A016	35.96	38.44	0.59	0.48	0.64	6.90	38.77	0.75	23.56	0.76	7.78
E23A020	31.78	33.58	0.74	0.36	0.58	5.65	30.07	0.79	17.43	0.80	-5.43
E23A021	14.17	11.89	0.57	1.34	0.68	-16.11	10.79	0.63	8.46	0.69	-23.88
E23A022	161.56	161.94	0.72	0.46	0.72	0.24	152.79	0.79	83.74	0.79	-5.46
E23A023	30.48	35.24	0.47	0.32	0.56	15.63	31.19	0.69	19.07	0.75	2.32
E23A025	7.76	6.60	0.52	0.31	0.55	-14.97	6.32	0.52	6.27	0.55	-18.55
E23A026	8.22	5.93	0.55	2.66	0.68	-27.96	6.50	0.76	5.62	0.79	-20.98
E23A027	18.33	22.03	0.66	0.84	0.58	20.17	20.83	0.67	11.73	0.74	13.64
E23A028	5.57	5.41	0.59	0.70	0.65	-2.80	4.99	0.73	3.62	0.73	-10.45
E23A029	15.94	14.16	0.51	0.35	0.60	-11.17	15.30	0.61	12.57	0.63	-4.05
E23A030	2.62	2.55	0.51	1.44	0.57	-2.60	3.04	0.54	1.83	0.60	15.91
E23A031	4.15	2.72	0.23	5.18	0.45	-34.36	4.40	0.34	5.53	0.38	5.96
E23A033	6.57	5.82	0.43	1.05	0.60	-11.33	5.83	0.54	3.99	0.56	-11.23
E23A034	25.12	22.05	0.53	1.03	0.68	-12.20	24.08	0.62	15.79	0.64	-4.19
E23A035	131.32	115.74	0.63	0.45	0.72	-11.86	104.94	0.70	72.62	0.75	-20.13
E23A036	14.04	12.62	0.33	1.79	0.68	-10.14	12.68	0.55	9.13	0.56	-9.71
E23A037	54.77	87.05	-0.03	0.87	0.41	58.95	109.55	-0.37	77.14	0.40	99.94
E23A038	36.88	35.64	0.74	0.40	0.73	-3.37	33.52	0.76	22.68	0.78	-9.14
E23A039	10.51	8.05	0.32	2.57	0.44	-23.36	9.54	0.48	7.74	0.52	-9.24
E23A040	2.42	2.56	0.52	0.81	0.60	5.93	2.93	0.55	1.84	0.65	21.29
E23A042	8.95	7.85	0.63	1.43	0.71	-12.35	8.52	0.61	5.45	0.64	-4.90
Mean	25.20	25.30	0.51	1.12	0.62	-5.24	25.23	0.61	16.42	0.66	-3.25
Median	12.27	9.97	0.52	0.88	0.63	-7.14	10.16	0.62	8.10	0.69	-5.44

The NSE value for validating the HBV-R model surpasses the HBV-Light model's by 0.1. The R² and bias correction values exhibit close alignment between the models. However, a substantial disparity emerges regarding RMSE, with HBV-light yielding a value of 1.12, while HBV-R demonstrates a significantly higher RMSE of 16.42.

Table 4-7 Validation Statistics for HBV-Light Model for GCM

Sub-Basins	HADGEM					GFDL					MPI					
	Qobs (m ³ /s)	Qsim (m ³ /s)	NSE	RMSE (m ³ /s)	R ²	Bias (%)	Qsim (m ³ /s)	NSE	RMSE (m ³ /s)	R ²	Bias (%)	Qsim (m ³ /s)	NSE	RMSE (m ³ /s)	R ²	Bias (%)
D23A001	28.49	26.90	0.49	1.28	0.66	-5.59	30.57	0.51	1.27	0.53	7.30	20.14	0.42	1.38	0.59	-29.29
D23A026	2.70	2.71	0.60	1.11	0.55	0.22	3.08	0.62	1.07	0.59	14.07	2.34	0.42	1.33	0.71	-13.31
D23A031	9.60	10.65	0.46	1.72	0.60	11.01	10.30	0.60	1.48	0.56	7.35	8.34	0.41	1.79	0.66	-13.10
D23A032	1.69	1.99	0.34	1.18	0.51	17.76	1.33	0.05	1.41	0.13	-21.68	1.33	0.19	1.30	0.38	-21.64
D23A037	0.33	0.52	0.02	0.67	0.63	56.93	0.48	0.44	0.51	0.74	45.94	0.34	0.25	0.59	0.63	2.47
E23A004	1.33	1.58	0.33	0.79	0.47	18.59	1.42	0.64	0.58	0.57	6.68	1.16	0.37	0.77	0.56	-12.62
E23A005	1.88	1.94	0.53	0.65	0.55	3.36	2.21	0.67	0.54	0.70	17.54	1.64	0.44	0.70	0.56	-12.55
E23A016	11.74	13.29	0.35	0.61	0.49	13.13	16.13	0.52	0.52	0.64	37.39	10.23	0.43	0.57	0.57	-12.91
E23A020	43.09	46.38	0.39	0.56	0.40	7.64	50.82	0.62	0.44	0.71	17.96	31.76	0.29	0.60	0.51	-26.29
E23A021	129.89	112.17	0.60	1.38	0.53	-13.64	138.49	0.73	1.14	0.66	6.62	92.24	0.39	1.70	0.61	-28.99
E23A022	37.64	42.71	0.47	0.55	0.52	13.48	47.71	0.52	0.52	0.60	26.76	38.04	0.05	0.74	0.57	1.07
E23A023	2.40	3.32	0.01	0.39	0.33	38.44	2.78	0.29	0.33	0.55	15.89	2.58	0.31	0.32	0.45	7.45
E23A026	650.29	551.44	0.55	2.98	0.54	-15.20	590.43	0.40	3.46	0.55	-9.20	564.93	0.52	3.09	0.46	-13.13
E23A027	113.30	118.05	0.36	1.31	0.48	4.19	126.38	0.28	1.39	0.54	11.55	120.46	0.46	1.21	0.43	6.33
E23A028	16.78	19.05	0.49	0.79	0.59	13.58	24.12	0.43	0.84	0.56	43.78	17.01	0.50	0.78	0.63	1.36
E23A029	1.03	1.28	0.27	0.43	0.39	23.85	1.59	0.26	0.43	0.46	54.38	1.09	0.31	0.41	0.42	6.18
E23A030	26.62	30.85	0.47	1.58	0.63	15.89	30.59	0.65	1.27	0.62	14.91	28.00	0.50	1.52	0.70	5.18
E23A031	22.76	25.05	0.23	5.17	0.45	10.08	30.75	0.14	5.46	0.41	35.12	23.09	0.26	5.05	0.39	1.44
E23A033	55.52	48.37	0.27	1.09	0.61	-12.87	43.68	0.35	1.03	0.73	-21.32	36.54	0.33	1.04	0.68	-34.18
E23A034	1.89	1.48	0.41	1.25	0.67	-21.71	2.07	0.43	1.23	0.51	9.59	1.32	0.36	1.30	0.58	-30.15
E23A035	0.70	0.84	0.44	0.50	0.74	20.45	0.91	0.28	0.57	0.72	30.84	0.50	0.41	0.51	0.60	-27.48
E23A036	9.06	8.17	0.65	1.37	0.58	-9.81	8.98	0.62	1.43	0.71	-0.85	4.57	0.19	2.08	0.59	-49.52
E23A037	11.98	10.96	0.37	0.72	0.72	-8.56	13.02	0.56	0.60	0.73	8.67	8.23	0.32	0.75	0.60	-31.35
E23A038	97.77	105.22	0.49	0.54	0.44	7.61	126.00	0.61	0.47	0.75	28.88	66.41	0.29	0.63	0.50	-32.08
E23A040	7.76	7.19	0.40	1.33	0.59	-7.36	6.69	0.47	1.26	0.67	-13.81	4.13	0.17	1.57	0.53	-46.72
E23A042	175.09	204.97	0.56	1.47	0.60	17.06	179.51	0.68	1.27	0.64	2.52	132.59	0.53	1.52	0.63	-24.28
Mean	56.20	53.73	0.41	1.21	0.55	7.64	57.31	0.48	1.17	0.60	14.50	46.88	0.35	1.28	0.56	-16.47
Median	11.86	12.12	0.43	1.10	0.55	8.86	14.58	0.51	1.05	0.61	12.81	9.28	0.36	1.12	0.58	-13.22

In Table 4-7, aside from the bias parameter in which HadGEM exhibits superior performance compared to GFDL and MPI, the other parameters demonstrate similarities across the models. The NSE values are ranked in descending order: GFDL has the highest value at 0.48, followed by HadGEM at 0.41, and MPI at 0.35.

As a result of data limitations, the TRMM 3B42 model was solely validated using the parameter set acquired from ERA5-Land calibration without undergoing its calibration process. The findings presented in Table 4-8 highlight that while the TRMM 3B42 dataset yields favorable outcomes in certain sub-basins, its overall performance could be better. Nonetheless, an individual comparison between the HBV-Light and HBV-R models for TRMM 3B42 suggests that the HBV-R model demonstrates superior performance, even though it was not calibrated using the same dataset.

Table 4-8 Validation Statistics for HBV-LIGHT and HBV-R Model for TRMM3B42

Sub-Basins	HBV-LIGHT TRMM 3B42 VALIDATION						HBV-R TRMM 3B42 VALIDATION					
	Qobs (m ³ /s)	Qsim (m ³ /s)	NSE	RMSE (m ³ /s)	R ²	Bias (%)	Qsim (m ³ /s)	NSE	RMSE (m ³ /s)	R ²	Bias (%)	
D23A001	31.16	28.01	0.54	1.24	0.55	-10.11	29.10	0.61	22.03	0.62	-6.61	
D23A003	2.50	1.80	0.02	2.02	0.28	-27.71	1.55	0.59	2.47	0.65	-38.08	
D23A016	5.49	2.40	-0.10	1.07	0.20	-56.25	2.38	0.21	5.07	0.56	-56.77	
D23A026	2.21	2.05	0.41	1.63	0.42	-6.95	1.54	0.40	2.09	0.47	-30.42	
D23A031	1.31	1.24	0.14	2.39	0.41	-5.00	0.94	0.57	1.17	0.62	-28.47	
D23A032	2.28	2.11	-0.16	1.38	0.38	-7.62	1.94	0.56	1.52	0.62	-14.90	
D23A037	1.38	4.38	-14.96	3.35	0.55	216.14	2.56	-0.98	2.84	0.42	84.68	
E23A004	16.08	21.31	-0.65	1.23	0.48	32.48	14.54	0.58	12.49	0.64	-9.62	
E23A005	73.30	116.23	-0.87	1.35	0.48	58.57	95.62	0.23	72.68	0.50	30.43	
E23A016	38.74	60.84	-1.25	1.19	0.53	57.05	44.26	0.53	34.47	0.64	14.23	
E23A020	30.63	3.25	-0.30	0.80	0.40	-89.38	3.43	-0.28	43.45	0.33	-88.81	
E23A021	14.73	14.94	-0.48	2.64	0.49	1.37	9.67	0.50	10.40	0.62	-34.38	
E23A023	28.01	26.67	0.11	0.37	0.58	-4.77	23.06	0.31	25.54	0.55	-17.69	
E23A026	1.09	1.24	-0.23	0.51	0.30	13.97	5.80	-54.52	9.91	0.36	432.70	
E23A027	37.09	21.64	0.48	2.40	0.59	-41.66	15.07	0.30	39.02	0.64	-59.39	
E23A028	5.94	1.68	-0.06	1.25	0.26	-71.77	2.41	0.33	6.25	0.60	-59.37	
E23A029	17.63	10.75	0.15	0.54	0.30	-38.98	10.04	0.29	20.07	0.43	-43.02	
E23A030	2.67	1.89	0.39	1.66	0.48	-29.20	2.26	0.42	2.13	0.46	-15.48	
E23A031	4.32	2.58	0.17	5.82	0.23	-40.16	3.69	0.25	6.38	0.28	-14.74	
E23A033	5.89	1.42	-0.31	1.49	0.38	-75.82	1.61	-0.15	5.92	0.49	-72.73	
E23A034	25.01	22.52	0.03	1.55	0.38	-9.97	20.52	0.56	17.90	0.64	-17.95	
E23A035	125.12	106.05	0.23	0.65	0.51	-15.24	93.79	0.59	86.36	0.67	-25.05	
E23A036	13.25	10.96	0.52	1.50	0.58	-17.27	10.71	0.61	8.41	0.66	-19.19	
E23A037	58.33	0.31	-0.66	1.19	0.01	-99.47	2.70	-0.55	88.61	0.18	-95.38	
E23A038	35.51	42.87	-0.09	0.80	0.58	20.73	30.33	0.56	30.37	0.69	-14.59	
E23A040	2.65	1.24	0.10	1.33	0.29	-53.29	1.43	0.40	2.56	0.53	-45.97	
E23A042	9.03	3.18	-0.06	2.49	0.40	-64.84	6.53	0.50	6.30	0.58	-27.78	
Mean	21.90	19.02	-0.63	1.62	0.41	-13.52	16.20	-1.73	20.98	0.54	-10.16	
Median	13.25	3.25	-0.06	1.35	0.41	-15.24	5.80	0.40	9.91	0.58	-25.05	

Table 4-9 NSE Values of The Historical Datasets

Sub-Basins	HL-ERA5	HL-ERA5	HL-GCM	HL-GCM	HR-ERA5	HR-ERA5	HL-TRMM	HR-TRMM
	CAL	VAL	CAL	VAL	CAL	VAL	VAL	VAL
D23A001	0.65	0.59	0.59	0.47	0.71	0.69	0.54	0.61
D23A003	0.62	0.74	-	-	0.74	0.69	0.02	0.59
D23A016	0.62	0.38	-	-	0.47	0.52	-0.10	0.21
D23A026	0.65	0.47	0.61	0.55	0.75	0.68	0.41	0.40
D23A031	0.73	0.63	0.60	0.49	0.74	0.58	0.14	0.57
D23A032	0.52	0.38	0.33	0.19	0.63	0.62	-0.16	0.56
D23A037	0.82	0.27	0.66	0.24	0.77	0.58	-14.96	-0.98
E23A004	0.58	0.42	0.53	0.45	0.73	0.75	-0.65	0.58
E23A005	0.71	0.6	0.60	0.55	0.80	0.76	-0.87	0.23
E23A016	0.64	0.59	0.57	0.43	0.76	0.75	-1.25	0.53
E23A020	0.57	0.74	0.58	0.43	0.65	0.79	-0.30	-0.28
E23A021	0.67	0.57	0.59	0.57	0.70	0.63	-0.48	0.50
E23A022	0.72	0.72	0.56	0.35	0.79	0.79	-	-
E23A023	0.55	0.47	0.44	0.20	0.67	0.69	0.11	0.31
E23A025	0.55	0.52	-	-	0.67	0.52	-	-
E23A026	0.62	0.55	0.51	0.49	0.57	0.76	-0.23	-54.52
E23A027	0.57	0.66	0.48	0.37	0.62	0.67	0.48	0.30
E23A028	0.65	0.59	0.59	0.47	0.73	0.73	-0.06	0.33
E23A029	0.59	0.51	0.42	0.28	0.68	0.61	0.15	0.29
E23A030	0.57	0.51	0.64	0.54	0.65	0.54	0.39	0.42
E23A031	0.33	0.22	0.39	0.21	0.46	0.34	0.17	0.25
E23A033	0.6	0.43	0.68	0.32	0.70	0.54	-0.31	-0.15
E23A034	0.67	0.53	0.58	0.40	0.73	0.62	0.03	0.56
E23A035	0.72	0.63	0.67	0.38	0.82	0.70	0.23	0.59
E23A036	0.67	0.33	0.67	0.49	0.69	0.55	0.52	0.61
E23A037	0.49	0	0.68	0.42	0.15	-0.37	-0.66	-0.55
E23A038	0.73	0.74	0.61	0.46	0.79	0.76	-0.09	0.56
E23A039	0.36	0.32	0.60	0.35	0.34	0.48	-	-
E23A040	0.6	0.52	-	-	0.66	0.55	0.10	0.40
E23A042	0.71	0.63	0.67	0.59	0.63	0.61	-0.06	0.50
Mean	0.62	0.51	0.57	0.41	0.66	0.61	-0.63	-1.73
Median	0.62	0.53	0.59	0.43	0.69	0.62	-0.06	0.40

The table provided showcases the performance of the HBV-Light (HL) and HBV-R (HR) models, with "CAL" denoting the calibration period and "VAL" representing the validation period. Notably, the NSE values of the GCM models are presented as an ensemble mean and are collectively compared.

It could be seen that HBV-Light model NSE values for ERA5-Land calibration and validation are higher than GCM. The averages for calibration and validation periods remain relatively close for ERA5-Land in both models, except for the TRMM 3B42 analysis. However, upon closer individual examination, it becomes evident that the HBV-R model consistently outperforms the HBV-Light model across various cases.

To conduct a detailed performance comparison between the two distinct HBV models, the E23A022 Sub-Basin is chosen. This selection is based on the basin's extensive coverage within the Çoruh Basin and the availability of 20 years of observational data (Table 3-5).

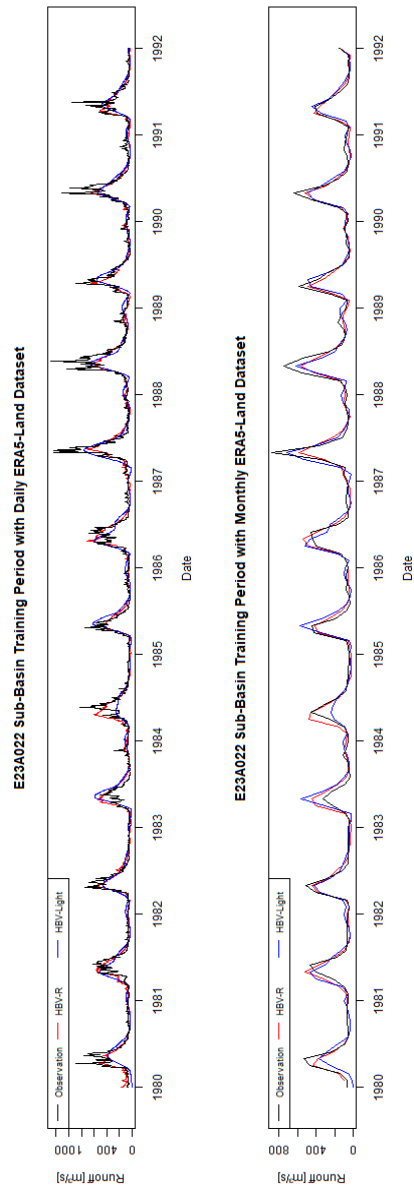


Figure 4-5 E23A022 Sub-Basin Training Period

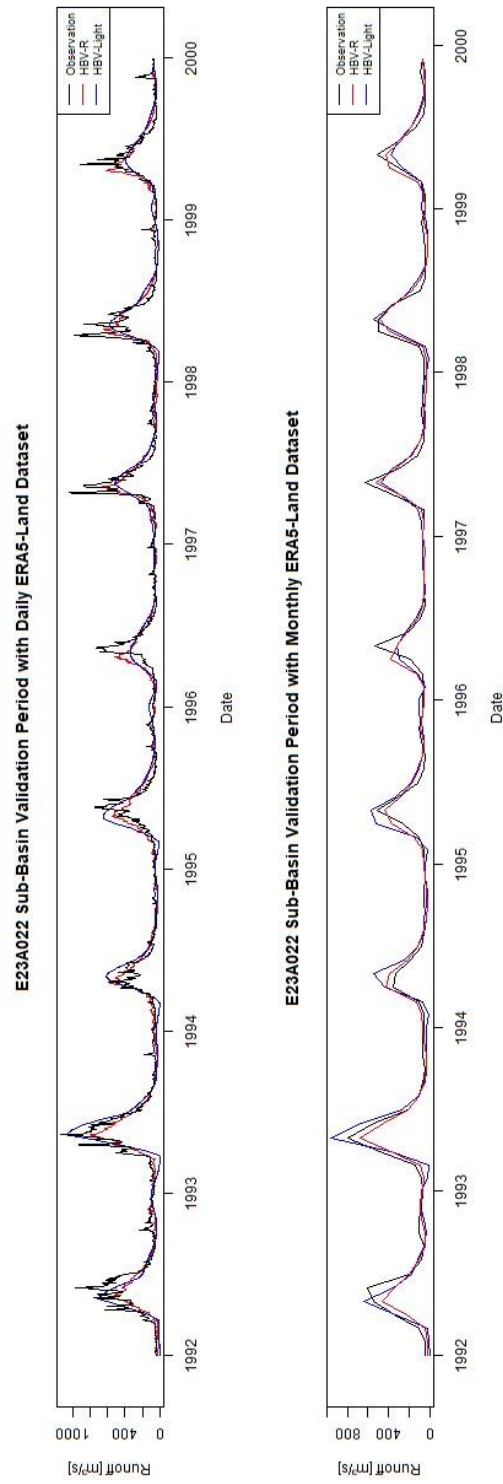


Figure 4-6 E23A022 Sub-Basin Validation Period

The graph below shows HBV-Light calibrated with historical GCMs and HBV-R calibrated ERA5-Land parameters, along with the observation for surface runoff in m³/s. The interquartile graph is provided in Figure 4-7 to compare the data distribution visually.

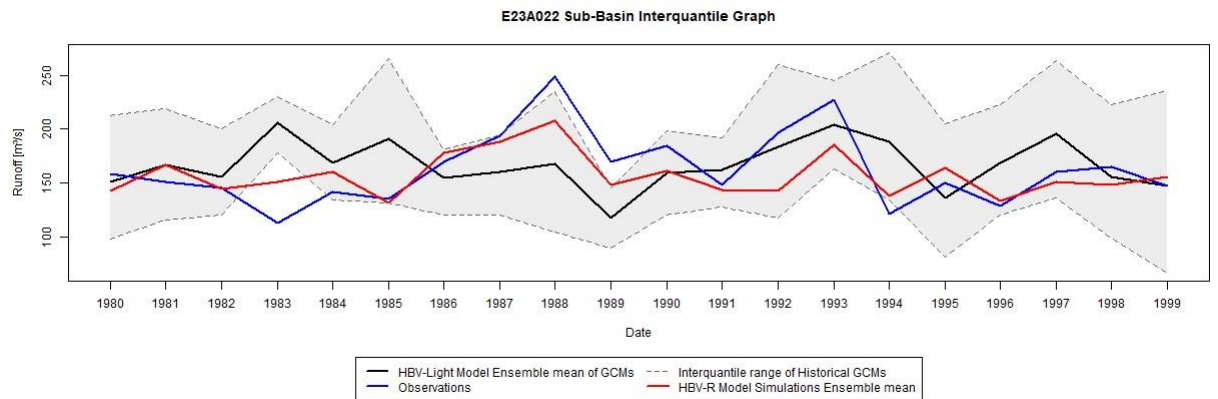


Figure 4-7 E23A022 Sub-Basin Interquartile Graph of Runoff

4.4 Future Projections of HBV Models

The tabulated data below presents future projections generated by the HBV-R models. Era5-Land calibrated parameter set is used, and the 3 GCMs' ensemble mean is calculated for the projections. There are substantial increases in runoff patterns under the RCP 4.5 scenario. In the initial period, there is an approximate 21.5% increase in runoff, followed by a modest decrease of approximately 2.2% in the subsequent period. In contrast, the RCP 8.5 scenario demonstrates a comparatively lower increase, about 18.6%, in the first period, followed by a decrease in the second period, with a slight increase of 7.42% compared to historical values.

Table 4-10 Historical and Future Projected Mean Runoff Values with HBV-R Model

Sub-Basins	Period	Historical Period		RCP 4.5		RCP 8.5		Change (%)			
		Observed Runoff (m ³ /s)	Simulated Runoff (m ³ /s)	2023-2060 Runoff (m ³ /s)	2061-2098 Runoff (m ³ /s)	2023-2060 Runoff (m ³ /s)	2061-2098 Runoff (m ³ /s)	F1-4.5	F2-4.5	F2-8.5	F2-8.5
D23A001	1992-2005	31.46	29.17	20.39	19.72	19.77	17.04	-35.19	-37.32	-37.17	-45.83
D23A003	1998-2005	2.50	1.97	1.71	1.67	1.66	1.44	-31.56	-94.70	-94.72	-95.43
D23A016	1999-2005	5.26	4.16	1.22	1.19	1.14	0.91	-76.78	-96.21	-96.36	-97.10
D23A026	1980-2001	1.87	1.82	1.49	1.45	1.45	1.29	-20.43	-95.39	-95.38	-95.91
D23A031	1986-2005	1.28	1.02	1.16	1.12	1.13	1.00	-8.85	-96.43	-96.42	-96.83
D23A032	1986-2005	2.31	2.28	3.27	3.21	3.22	2.98	41.41	-89.80	-89.77	-90.53
D23A037	1991-2005	1.46	1.25	2.17	2.15	2.14	1.96	48.45	-93.16	-93.20	-93.76
E23A004	1980-2005	15.55	14.88	21.74	21.39	21.28	19.73	39.77	-32.00	-32.34	-37.29
E23A005	1980-2005	69.94	66.29	91.43	90.12	89.54	82.07	30.73	186.48	184.64	160.91
E23A016	1980-2005	38.86	37.46	62.24	61.59	61.10	56.37	60.19	95.78	94.24	79.21
E23A020	1993-2005	28.89	27.62	12.55	12.44	11.88	10.37	-56.55	-60.44	-62.24	-67.02
E23A021	1980-2005	14.01	11.20	12.45	12.07	12.11	10.93	-11.14	-61.62	-61.49	-65.24
E23A022	1980-1999	162.32	156.61	223.00	218.65	217.56	197.17	37.38	595.07	591.62	526.79
E23A023	1980-2002	32.75	32.22	64.18	62.88	62.49	56.17	95.98	99.90	98.66	78.58
E23A025	1991-2005	7.04	6.06	13.25	13.16	12.98	11.97	88.33	-58.18	-58.73	-61.95
E23A026	1982-1997	8.70	6.79	5.61	5.35	5.39	4.67	-35.46	-83.00	-82.87	-85.15
E23A027	1982-1997	21.64	21.52	25.43	24.72	24.86	22.54	17.50	-21.42	-20.97	-28.35
E23A028	1982-2005	5.97	5.42	4.29	4.12	4.08	3.46	-28.17	-86.90	-87.04	-89.00
E23A029	1982-2005	16.58	15.54	24.68	24.30	24.02	21.31	48.84	-22.75	-23.64	-32.26
E23A030	1982-2005	2.88	3.05	1.47	1.39	1.39	1.16	-48.98	-95.58	-95.57	-96.31
E23A031	1988-1999	4.97	4.56	3.31	3.08	3.13	2.58	-33.27	-90.20	-90.06	-91.80
E23A033	1994-2005	5.68	5.63	3.29	3.22	3.19	2.83	-42.03	-89.75	-89.86	-90.99
E23A034	1990-2005	25.45	24.25	28.76	27.91	27.99	25.18	13.00	-11.26	-11.00	-19.95
E23A035	1993-2005	114.92	98.23	187.05	184.87	183.96	168.58	62.76	487.70	484.82	435.92
E23A036	1993-2005	12.91	12.77	6.42	5.97	6.00	4.77	-50.32	-81.01	-80.94	-84.83
E23A037	1990-2005	54.87	99.71	21.74	21.62	20.91	18.48	-60.38	-31.26	-33.54	-41.25
E23A038	1993-2005	32.91	30.56	47.63	47.14	46.69	42.72	44.72	49.85	48.42	35.79
E23A039	1991-1998	12.14	9.97	7.43	7.12	7.15	6.34	-38.76	-77.36	-77.26	-79.86
E23A040	1992-2005	2.68	2.88	2.67	2.60	2.61	2.29	-0.37	-91.72	-91.71	-92.71
E23A042	1993-2005	9.01	8.69	5.25	4.86	4.90	3.86	-41.71	-84.56	-84.43	-87.74
Mean		24.89	24.79	30.24	29.70	29.52	26.74	0.30	-5.57	-6.14	-15.00
	Change in Flow (%)			21.49	19.32	18.60	7.42				

Table 4-11 presents future projections obtained by the HBV-Light model. In contrast to the HBV-R model, this model suggests a decrease in runoff during the future periods for both scenarios. The decrease in the RCP 4.5 scenario is less significant, with a 2.7% decrease in the first period and a 3.6% decrease in the second. However, in the RCP 8.5 scenario, there is a dramatic decrease in runoff, with a 2.95% decrease in the first period and a 14.3% decrease in the second period.

Table 4-11 Historical and Future Projected Mean Runoff Values with HBV-Light Model

Sub-Basins	Period	Historical Period		RCP 4.5		RCP 8.5		Change (%)			
		Observed Runoff (m ³ /s)	Simulated Runoff (m ³ /s)	2023-2060 Runoff (m ³ /s)	2061-2098 Runoff (m ³ /s)	2023-2060 Runoff (m ³ /s)	2061-2098 Runoff (m ³ /s)	F1-4.5	F2-4.5	F2-8.5	F2-8.5
D23A001	1992-2005	31.46	28.06	32.71	33.15	33.56	30.29	3.98	5.39	6.70	-3.71
D23A003	1998-2005	2.50	2.28	1.58	1.52	1.57	1.33	-94.96	-95.16	-95.02	-95.78
D23A016	1999-2005	5.26	4.47	0.09	0.09	0.10	0.06	-99.71	-99.71	-99.69	-99.82
D23A026	1980-2001	1.87	1.78	1.23	1.19	1.19	1.03	-96.09	-96.22	-96.21	-96.72
D23A031	1986-2005	1.28	1.17	1.24	1.21	1.22	1.09	-96.05	-96.14	-96.11	-96.54
D23A032	1986-2005	2.31	2.27	2.44	2.35	2.40	2.08	-92.23	-92.53	-92.38	-93.39
D23A037	1991-2005	1.46	1.43	1.21	1.19	1.18	0.97	-96.16	-96.21	-96.24	-96.92
E23A004	1980-2005	15.55	15.32	11.22	11.04	11.65	10.09	-64.32	-64.89	-62.97	-67.94
E23A005	1980-2005	69.94	68.59	52.40	51.74	52.13	46.41	66.57	64.47	65.71	47.53
E23A016	1980-2005	38.86	38.40	36.48	36.05	36.44	31.86	15.98	14.59	15.85	1.29
E23A020	1993-2005	28.89	30.42	4.16	4.45	4.13	3.96	-86.78	-85.86	-86.88	-87.42
E23A021	1980-2005	14.01	12.35	19.07	18.68	18.48	16.60	-39.38	-40.63	-41.25	-47.22
E23A022	1980-1999	162.32	160.00	175.49	173.26	174.23	156.00	457.89	450.78	453.88	395.93
E23A023	1980-2002	32.75	35.14	43.25	41.38	42.40	33.68	37.48	31.53	34.80	7.07
E23A025	1991-2005	7.04	6.58	6.81	7.10	6.80	6.83	-78.36	-77.43	-78.37	-78.29
E23A026	1982-1997	8.70	6.52	13.70	13.56	13.78	12.10	-56.45	-56.88	-56.20	-61.55
E23A027	1982-1997	21.64	21.11	54.18	54.98	54.66	49.04	72.25	74.79	73.75	55.89
E23A028	1982-2005	5.97	5.77	6.37	6.39	6.53	5.64	-79.75	-79.67	-79.25	-82.09
E23A029	1982-2005	16.58	15.55	8.21	9.18	8.18	6.72	-73.91	-70.83	-74.01	-78.62
E23A030	1982-2005	2.88	2.72	1.49	1.43	1.44	1.19	-95.26	-95.46	-95.42	-96.21
E23A031	1988-1999	4.97	3.05	5.65	5.72	5.66	5.01	-82.03	-81.82	-82.00	-84.06
E23A033	1994-2005	5.68	5.35	5.23	5.35	5.37	4.93	-83.38	-83.00	-82.93	-84.33
E23A034	1990-2005	25.45	23.22	54.45	53.31	55.19	47.42	73.11	69.46	75.44	50.76
E23A035	1993-2005	114.92	108.03	131.93	130.22	130.72	116.16	319.42	313.97	315.56	269.28
E23A036	1993-2005	12.91	12.06	8.37	8.04	8.22	6.98	-73.39	-74.45	-73.88	-77.81
E23A037	1990-2005	54.87	73.50	0.02	0.02	0.01	0.01	-99.94	-99.94	-99.95	-99.98
E23A038	1993-2005	32.91	32.68	25.20	25.44	25.44	23.53	-19.88	-19.14	-19.12	-25.19
E23A039	1991-1998	12.14	8.85	13.03	12.77	12.88	11.04	-58.57	-59.40	-59.06	-64.92
E23A040	1992-2005	2.68	2.69	2.56	2.50	2.51	2.27	-91.87	-92.05	-92.03	-92.79
E23A042	1993-2005	9.01	8.31	6.88	6.61	6.73	5.64	-78.14	-78.98	-78.61	-82.07
Mean		24.89	24.59	24.22	24.00	24.16	21.33	-23.00	-23.71	-23.20	-32.19
	Change in Flow (%)			-2.70	-3.60	-2.95	-14.31				

Surface runoff is calculated for two different HBV models. The E23A022 sub-basin has been selected for more extensive examination in the context of these two models. This choice is based on the consideration that its substantial geographical coverage of 18 000 km² and the availability of 20 years of observational data make it representative of the Çoruh Basin. For this sub-basin, HBV-R indicates a 37.4% increase in the first half and a 34.7% increase in the second half for the RCP 4.5 scenario. For RCP 8.5 scenarios, 34% and 21.5% increases are projected for the first and second periods, respectively. Compared with the HBV-Light model for RCP 4.5, the growth is 8% for the first period and 6.7% for the following period. For RCP 8.5, the first half shows a 7.3% increase, while the second period indicates a decrease in runoff with 3.9%. The figures of annual future projections and interquartile graphs for the two models are given below.

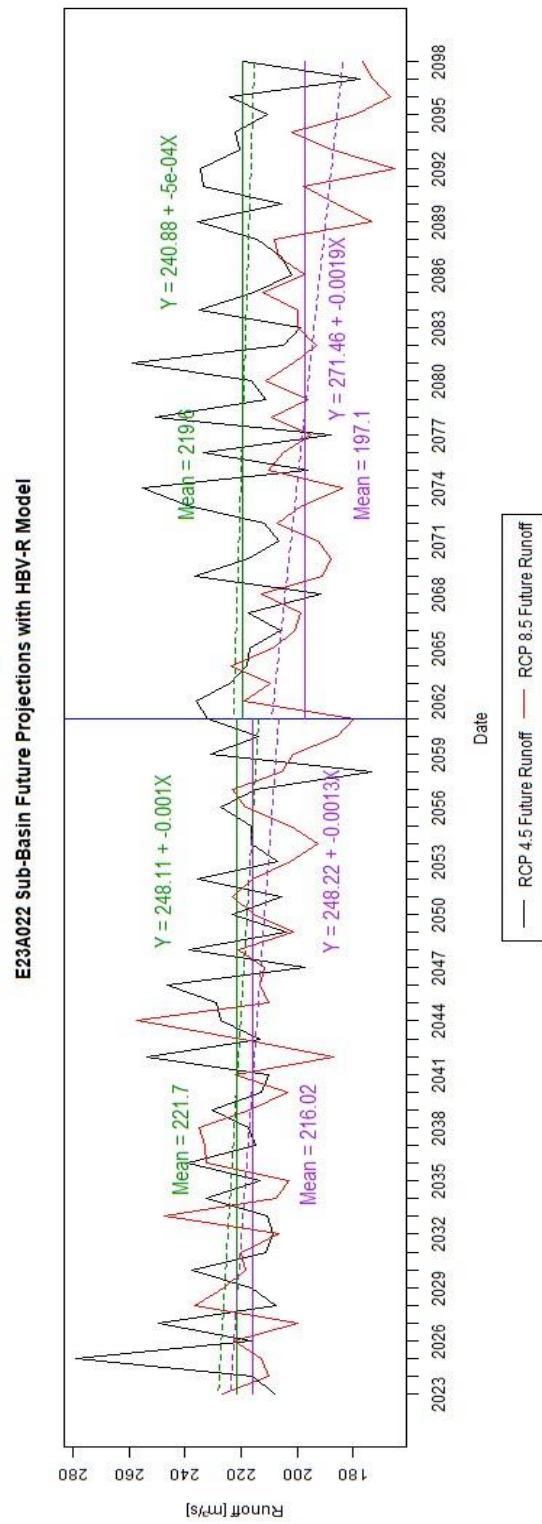


Figure 4-8 E23A022 Sub-Basin Future Surface Runoff Projections with HBV-R Model

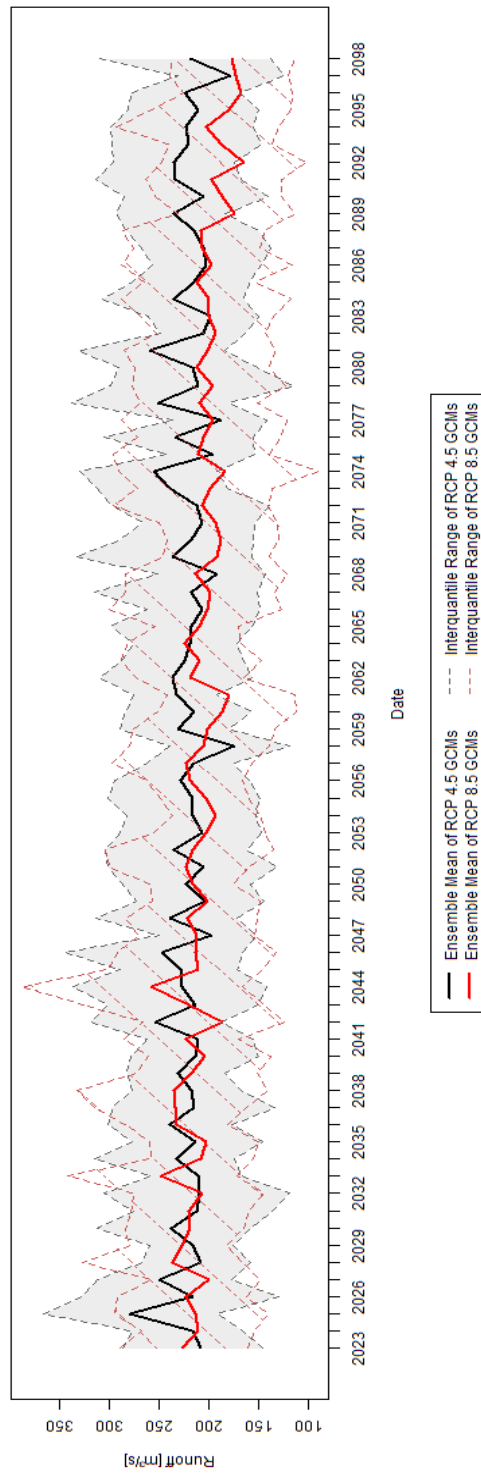


Figure 4-9 E23A022 Sub-Basin Annual Surface Runoff Projections with HBV-R Model

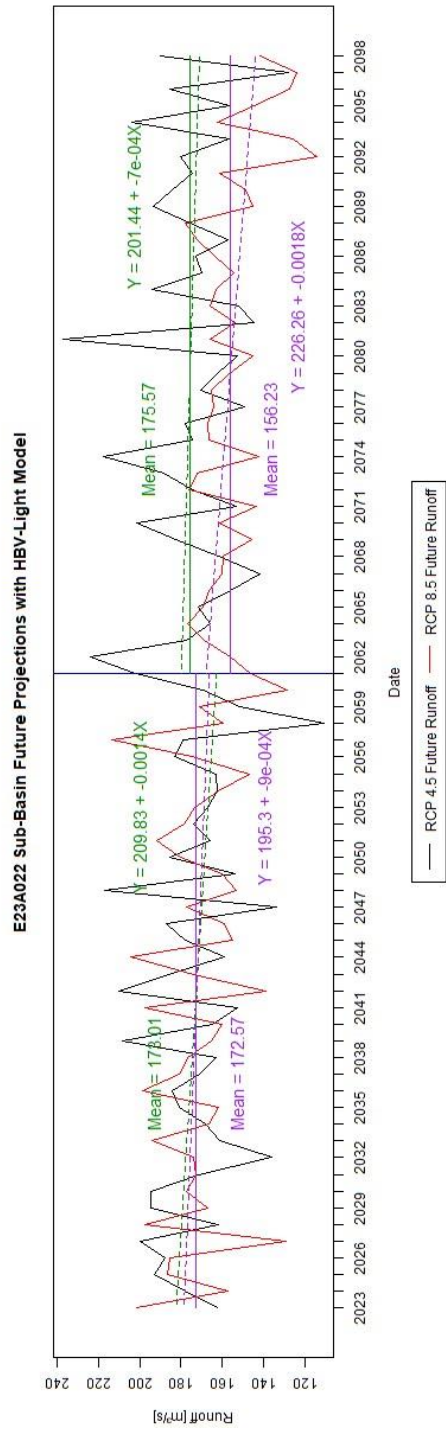


Figure 4-10 E23A022 Sub-Basin Future Surface Runoff Projections with HBV-Light Model

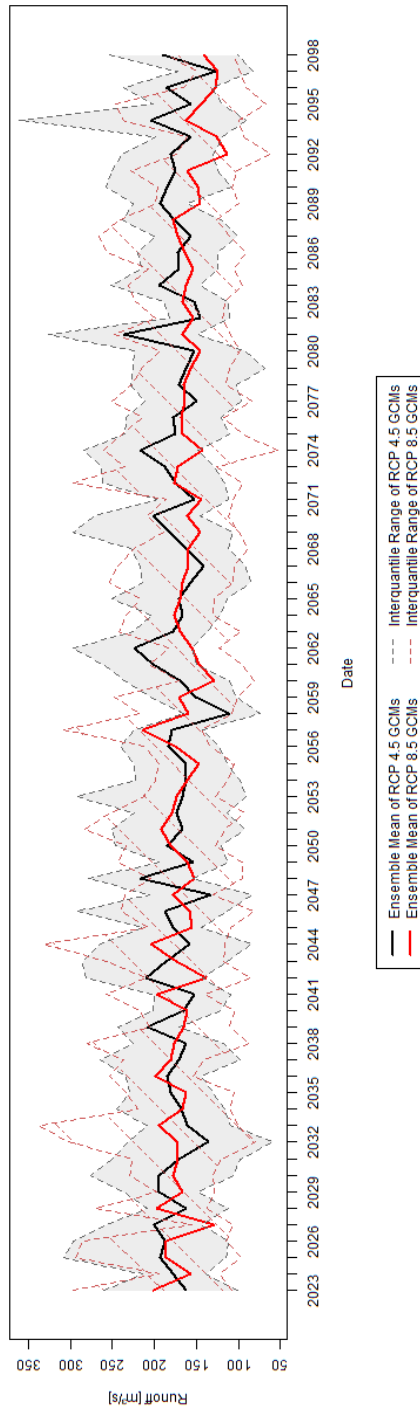


Figure 4-11 E23A022 Sub-Basin Annual Surface Runoff Projections with HBV-Light Model

A study done by SYGM (2020) indicated that there would be a significant decrease in the overall water potential, amounting to approximately 20%, as a result of climate change. Conversely, another study conducted by Yucel et al. (2015) projected an increase of approximately 4% in average daily stream flows from 2070 to 2099. These findings closely align with the projections generated by the HBV-Light model. However, it's worth noting that the HBV-R model tends to overestimate surface runoff compared to these projections.

CHAPTER 5

CONCLUSIONS AND RECOMMENDATIONS

The study aims to introduce a new and open-source conceptual hydrological model called HBV-R, where HBV-Light is used as a benchmark hydrological model to compare the performance of HBV-R. This study is implemented over Çoruh Basin for the historical period (utilizing ERA5-Land, TRMM, and RCM datasets between 1980 and 2005) and the future (utilizing RCM datasets between 2020 and 2100), where the LHS method is used to acquire optimized HBV-R parameters. The study conducts assessments of climate change impacts using GCMs (HADGEM, MPI, and GFDL) and validates both hydrological models for future projections. Given the constraints of data and the commendable performance of the HBV-R model, it could be said that the conceptual and newly developed HBV-R model performs better in the case of scarce data.

The HBV-Light and HBV-R models initially show similar performance during the calibration period, with Nash-Sutcliffe values of 0.62 and 0.66, respectively. However, a notable disparity arises in their validation results, with the HBV-R model achieving an NSE value of approximately 0.61 compared to the HBV-Light model's 0.51. The HBV-R model demonstrates a substantial improvement in basin representation, with an enhancement of around 20% in the Nash-Sutcliffe Efficiency (NSE) value. In contrast, the HBV-Light model aligns more closely with the findings of previous studies, where HBV-R predicts significantly higher increases than other models. Specifically, HBV-Light suggests a decrease of surface runoff potential of approximately 3% and 8% for RCP 4.5 and RCP 8.5, respectively. Meanwhile, the HBV-R model projects a dramatic increase in the surface runoff potential with 20% for RCP 4.5 and 13% for RCP 8.5.

To sum up:

- HBV-R model performed better than HBV-Light in training and validation, comparing the NSE value.
- Conversely, HBV-Light aligns more closely in future predictions with the previous studies.
- The models that used TRMM 3B42 did not perform well since there was no data. Even though the HBV-R model performed better at most of the basins than the HBV-Light.
- HBV-R model for the second period of the RCP 8.5 scenario gave similar findings to another study.
- The increase in the rainfall in future projections overlaps with the conclusions from HBV-R, but in some basins, the model tends to overestimate.
- The additional snow component in the HBV-R could be said to be playing a part in improving the model's understanding.

For further investigation, to comprehensively explore the HBV-R model's performance and to model the impacts of climate change on runoff accurately, the study suggests extending analyses to alternative geographical regions characterized by different climatic conditions. Given that the LHS method requires a longer calibration time than the GAP optimization technique, considering alternative parameter calibration algorithms is advisable to enhance efficiency. Despite its simplicity, the HBV-R model offers room for further enhancement and refinement (e.g., via more calibrated parameters). Additionally, considering alternative evapotranspiration equations or utilizing different temperature and precipitation datasets could contribute to refining the model's representation. Furthermore, expanding the study's scope to encompass a broader range of GCMs and adopting diverse bias-correction and downscaling methodologies holds the potential to boost the model's predictive accuracy and enhance its future projection capabilities.

REFERENCES

- Abyani, M., & Bahaari, M. R. (2020). A comparative reliability study of corroded pipelines based on Monte Carlo Simulation and Latin Hypercube Sampling methods. *International Journal of Pressure Vessels and Piping*, *181*, 104079. <https://doi.org/10.1016/J.IJPVP.2020.104079>
- Afshar, M. H., Şorman, A. Ü., Tosunoğlu, F., Bulut, B., Yilmaz, M. T., & Danandeh Mehr, A. (2020). Climate change impact assessment on mild and extreme drought events using copulas over Ankara, Turkey. *Theoretical and Applied Climatology*, *141*(3–4), 1045–1055. <https://doi.org/10.1007/S00704-020-03257-6/TABLES/4>
- Aghakouchak, A., Nakhjiri, N., & Habib, E. (2013). An educational model for ensemble streamflow simulation and uncertainty analysis. *Hydrology and Earth System Sciences*, *17*(2), 445–452. <https://doi.org/10.5194/HESS-17-445-2013>
- Bağçacı, S. Ç., Yucel, I., Duzenli, E., & Yilmaz, M. T. (2021). Intercomparison of the expected change in the temperature and the precipitation retrieved from CMIP6 and CMIP5 climate projections: A Mediterranean hot spot case, Turkey. *Atmospheric Research*, *256*, 105576. <https://doi.org/10.1016/J.ATMOSRES.2021.105576>
- Bayar, A. S., Yilmaz, M. T., Yücel, İ., & Dirmeyer, P. (2023). CMIP6 Earth System Models Project Greater Acceleration of Climate Zone Change Due To Stronger Warming Rates. *Earth's Future*, *11*(4), e2022EF002972. <https://doi.org/10.1029/2022EF002972>
- Beck, H. E., Van Dijk, A. I. J. M., De Roo, A., Dutra, E., Fink, G., Orth, R., & Schellekens, J. (2017). Global evaluation of runoff from 10 state-of-the-art

- hydrological models. *Hydrol. Earth Syst. Sci*, 21, 2881–2903.
<https://doi.org/10.5194/hess-21-2881-2017>
- Beck, M. B. (1991). Forecasting environmental change. *Journal of Forecasting*, 10(1–2), 3–19. <https://doi.org/10.1002/FOR.3980100103>
- Bergström, S. (1995). The HBV model. *Computer Models of Watershed Hydrology*, 443–476.
- BERGSTROM, S., & FORSMAN, A. (1973). DEVELOPMENT OF A CONCEPTUAL DETERMINISTIC RAINFALL-RUNOFF MODEL. *NORDIC HYDROL.*, 4(3 (1973)), 147–170.
<https://doi.org/10.2166/NH.1973.0012>
- Birundu, A. M., & Mutua, B. M. (2017). Analyzing the Mara River Basin Behaviour through Rainfall-Runoff Modeling. *International Journal of Geosciences*, 08(09), 1118–1132. <https://doi.org/10.4236/IJG.2017.89064>
- Bizuneh, B. B., Moges, M. A., Sinshaw, B. G., & Kerebih, M. S. (2021). SWAT and HBV models' response to streamflow estimation in the upper Blue Nile Basin, Ethiopia. *Water-Energy Nexus*, 4, 41–53.
<https://doi.org/10.1016/J.WEN.2021.03.001>
- Çallı, S. S. (2023). *Dağlık karst akiferleri için parametrik yağış-karstik kaynak boşalımı modeli geliştirilmesi*. <https://doi.org/10.13140/RG.2.2.12194.81604>
- Çallı, S. S., Çallı, K. Ö., Tuğrul Yılmaz, M., & Çelik, M. (2022). Contribution of the satellite-data driven snow routine to a karst hydrological model. *Journal of Hydrology*, 607, 127511. <https://doi.org/10.1016/J.JHYDROL.2022.127511>
- Cannon, A. J., Sobie, S. R., & Murdock, T. Q. (2015). Bias Correction of GCM Precipitation by Quantile Mapping: How Well Do Methods Preserve Changes in Quantiles and Extremes? *Journal of Climate*, 28(17), 6938–6959.
<https://doi.org/10.1175/JCLI-D-14-00754.1>

- Çolak, M. A. (2017). *PREDICTABILITY OF MONTHLY STREAMFLOW DISCHARGE USING REMOTE SENSING PRECIPITATION DATA BY DATA DRIVEN MODELS* [M.S. - Master of Science]. Middle East Technical University.
- Collins, W., Bellouin, N., Doutriaux-Boucher, M., Gedney, N., Hinton, T., Jones, C., Liddicoat, S., Martin, G., Rae, J., Senior, C., Totterdell, I., Woodward Reichler, S. T., Kim, J., Woodward, S., & Reichler, T. (2008). *Evaluation of HadGEM2 model Evaluation of the HadGEM2 model*.
- Cotronei, A., & Slawig, T. (2020). Single-precision arithmetic in ECHAM radiation reduces runtime and energy consumption. *Geoscientific Model Development*, *13*(6), 2783–2804. <https://doi.org/10.5194/GMD-13-2783-2020>
- Devia, G. K., Ganasri, B. P., & Dwarakish, G. S. (2015). A Review on Hydrological Models. *Aquatic Procedia*, *4*, 1001–1007. <https://doi.org/10.1016/J.AQPRO.2015.02.126>
- Driessen, T. L. A., Hurkmans, R. T. W. L., Terink, W., Hazenberg, P., Torfs, P. J. J. F., & Uijlenhoet, R. (2010). The hydrological response of the Ourthe catchment to climate change as modelled by the HBV model. *Hydrology and Earth System Sciences*, *14*(4), 651–665. <https://doi.org/10.5194/HESS-14-651-2010>
- Dutta, S., & Gandomi, A. H. (2020). Design of experiments for uncertainty quantification based on polynomial chaos expansion metamodels. *Handbook of Probabilistic Models*, 369–381. <https://doi.org/10.1016/B978-0-12-816514-0.00015-1>
- Eden, J. M., Widmann, M., Maraun, D., & Vrac, M. (2014). Comparison of GCM- and RCM-simulated precipitation following stochastic postprocessing. *Journal of Geophysical Research*, *119*(19), 11,040-11,053. <https://doi.org/10.1002/2014JD021732>

- ERA5-Land hourly data from 1950 to present.* (n.d.). Retrieved August 7, 2023, from <https://cds.climate.copernicus.eu/cdsapp#!/dataset/reanalysis-era5-land?tab=overview>
- Ersoy, N. E. (2022). *IMPACT OF CLIMATE CHANGE OVER THE VARIABILITY OF DROUGHT CHARACTERISTICS OVER 25 BASINS OF TURKEY.* <https://open.metu.edu.tr/handle/11511/96769>
- Fakioğlu, S., Kağnicioğlu, N., Genel, D., Dsi, M., Müdürlüğü, G., Ve, E., Dairesi, P., Yardımcısı, B., Ve Plan, E., Başkanlığı, D., & Müdürü, Ş. (2009). DOĞU KARADENİZ VE ÇORUH HAVZALARININ HİDROELEKTRİK ENERJİ ÜRETİMİ AÇISINDAN DEĞERLENDİRİLMESİ. *FORUM*, 13–15.
- Farr, T. G., Rosen, P. A., Caro, E., Crippen, R., Duren, R., Hensley, S., Kobrick, M., Paller, M., Rodriguez, E., Roth, L., Seal, D., Shaffer, S., Shimada, J., Umland, J., Werner, M., Oskin, M., Burbank, D., & Alsdorf, D. E. (2007). The Shuttle Radar Topography Mission. *Reviews of Geophysics*, 45(2), 2004. <https://doi.org/10.1029/2005RG000183>
- Fire Weather Indices Wiki | Potential evapotranspiration.* (n.d.). Retrieved August 7, 2023, from <https://wikifire.wsl.ch/tiki-indexf125.html?page=Potential+evapotranspiration>
- GES DISC.* (n.d.). Retrieved August 7, 2023, from https://disc.gsfc.nasa.gov/datasets/TRMM_3B42_7/summary
- GFDL. (n.d.). *Climate Model Downscaling – Geophysical Fluid Dynamics Laboratory.* Retrieved October 9, 2023, from <https://www.gfdl.noaa.gov/climate-model-downscaling/>
- Giorgetta, M. A., Jungclaus, J., Reick, C. H., Legutke, S., Bader, J., Böttinger, M., Brovkin, V., Crueger, T., Esch, M., Fieg, K., Glushak, K., Gayler, V., Haak, H., Hollweg, H.-D., Ilyina, T., Kinne, S., Kornblueh, L., Matei, D., Mauritsen, T., ... Stevens, B. (2013). Climate and carbon cycle changes from 1850 to 2100 in MPI-ESM simulations for the Coupled Model Intercomparison

Project phase 5. *Journal of Advances in Modeling Earth Systems*, 5(3), 572–597. <https://doi.org/10.1002/JAME.20038>

Grillakis, M. G., Tsanis, I. K., & Koutroulis, A. G. (2010). Natural Hazards and Earth System Sciences Application of the HBV hydrological model in a flash flood case in Slovenia. *Hazards Earth Syst. Sci*, 10, 2713–2725. <https://doi.org/10.5194/nhess-10-2713-2010>

Gudmundsson, L., Boulange, J., Do, H. X., Gosling, S. N., Grillakis, M. G., Koutroulis, A. G., Leonard, M., Liu, J., Schmied, H. M., Papadimitriou, L., Pokhrel, Y., Seneviratne, S. I., Satoh, Y., Thiery, W., Westra, S., Zhang, X., & Zhao, F. (2021). Globally observed trends in mean and extreme river flow attributed to climate change. *Science*, 371(6534), 1159–1162. <https://doi.org/10.1126/SCIENCE.ABA3996>

Gumus, B., Oruc, S., Yucel, I., & Tugrul Yilmaz, M. (2023). Impacts of Climate Change on Extreme Climate Indices in Türkiye Driven by High-Resolution Downscaled CMIP6 Climate Models. *Sustainability 2023*, Vol. 15, Page 7202, 15(9), 7202. <https://doi.org/10.3390/SU15097202>

Huntington, T. G. (2006). Evidence for intensification of the global water cycle: Review and synthesis. *Journal of Hydrology*, 319(1–4), 83–95. <https://doi.org/10.1016/J.JHYDROL.2005.07.003>

Ilyina, T., Six, K. D., Segschneider, J., Maier-Reimer, E., Li, H., & Núñez-Riboni, I. (2013). Global ocean biogeochemistry model HAMOCC: Model architecture and performance as component of the MPI-Earth system model in different CMIP5 experimental realizations. *Journal of Advances in Modeling Earth Systems*, 5(2), 287–315. <https://doi.org/10.1029/2012MS000178>

Inglezakis, V. J., Pouloupoulos, S. G., Arkhangelsky, E., Zorpas, A. A., & Menegaki, A. N. (2016). Aquatic Environment. *Environment and Development*, 137–212. <https://doi.org/10.1016/B978-0-444-62733-9.00003-4>

- IPCC. (2013). *What is a GCM?* https://www.ipcc-data.org/guidelines/pages/gcm_guide.html
- IPCC, Adger, N., Aggarwal, P., Agrawala, S., Alcamo, J., Allali, A., Anisimov, O., Arnell, N., Boko, M., Canziani, O., Carter, T., Casassa, G., Confalonieri, U., Cruz, R. V., De, E., Alcaraz, A., Easterling, W., Field, C., Fischlin, A., ... Hanson, C. E. (2007). Summary for Policymakers In: *Climate Change 2007: Impacts, Adaptation and Vulnerability. Contribution of Working Group II to the Fourth Assessment Report of the Intergovernmental Panel on Climate Change. Cambridge University Press.*
- Jungclaus, J. H., Fischer, N., Haak, H., Lohmann, K., Marotzke, J., Matei, D., Mikolajewicz, U., Notz, D., & Von Storch, J. S. (2013). Characteristics of the ocean simulations in the Max Planck Institute Ocean Model (MPIOM) the ocean component of the MPI-Earth system model. *Journal of Advances in Modeling Earth Systems*, 5(2), 422–446. <https://doi.org/10.1002/JAME.20023>
- Kazezyılmaz-Alhan, C. M., Yalçın, Javanshour, K., Aytekin, M., & Gülbaz, S. (2021). A hydrological model for Ayamama watershed in Istanbul, Turkey, using HEC-HMS. *Water Practice and Technology*, 16(1), 154–161. <https://doi.org/10.2166/WPT.2020.108>
- Kokkonen, T., Koivusalo, H., & Karvonen, T. (2001). A semi-distributed approach to rainfall-runoff modelling-a case study in a snow affected catchment. *Environmental Modelling & Software*, 16, 481–493. www.elsevier.com/locate/envsoft
- Kucherenko, S., Albrecht, D., & Saltelli, A. (2015). *Exploring multi-dimensional spaces: a Comparison of Latin Hypercube and Quasi Monte Carlo Sampling Techniques*. <https://arxiv.org/abs/1505.02350v1>
- Kumanlioglu, A. A., & Fistikoglu, O. (2019). Performance Enhancement of a Conceptual Hydrological Model by Integrating Artificial Intelligence. *Journal*

of Hydrologic Engineering, 24(11), 04019047.

[https://doi.org/10.1061/\(ASCE\)HE.1943-5584.0001850](https://doi.org/10.1061/(ASCE)HE.1943-5584.0001850)

Kundzewicz, Z. W. S., Bates, B. C., Kundzewicz, Z. W., Wu, S., & Palutikof, J. P. (2008). Climate Change and Water. *Eos, Transactions American Geophysical Union*, 71(12), 1–210. <https://www.taccire.sua.ac.tz/handle/123456789/552>

Lehner, B., Döll, P., Alcamo, J., Henrichs, T., & Kaspar, F. (2006). Estimating the impact of global change on flood and drought risks in Europe: A continental, integrated analysis. *Climatic Change*, 75(3), 273–299.

<https://doi.org/10.1007/S10584-006-6338-4>

Li, C.-Q., & Yang, W. (2023). Essential reliability methods. *Time-Dependent Reliability Theory and Its Applications*, 51–119. <https://doi.org/10.1016/B978-0-323-85882-3.00006-4>

Martin, M., Bellouin, N., Collins, W. J., Culverwell, I. D., Halloran, P. R., Hardiman, S. C., Hinton, T. J., Jones, C. D., McDonald, R. E., McLaren, A. J., O’connor, F. M., Roberts, M. J., Rodriguez, J. M., Woodward, S., Best, M. J., Brooks, M. E., Brown, A. R., Butchart, N., Dearden, C., ... Wiltshire, A. (2011). The HadGEM2 family of Met Office Unified Model climate configurations The HadGEM2 Development Team: G. *Geosci. Model Dev*, 4, 723–757. <https://doi.org/10.5194/gmd-4-723-2011>

Mesta, B., Kargı, P. G., Tezyapar, İ., Ayvaz, M. T., Göktaş, R. K., Kentel, E., & Tezel, U. (2019). Determination of Rainfall – Runoff Relationship in Yenicegoruce Basin with HEC-HMS Hydrologic Model. *Pamukkale University Journal of Engineering Sciences*, 25(8), 949–955.

<https://doi.org/10.5505/PAJES.2019.75133>

Motovilov, Y. G., Gottschalk, L., Engeland, K., & Rodhe, A. (1999). Validation of a distributed hydrological model against spatial observations. *Agricultural and Forest Meteorology*, 98–99, 257–277. [https://doi.org/10.1016/S0168-1923\(99\)00102-1](https://doi.org/10.1016/S0168-1923(99)00102-1)

- Nash, J. E., & Sutcliffe, J. V. (1970). River flow forecasting through conceptual models part I — A discussion of principles. *Journal of Hydrology*, *10*(3), 282–290. [https://doi.org/10.1016/0022-1694\(70\)90255-6](https://doi.org/10.1016/0022-1694(70)90255-6)
- Nuri Balov, M., & Altunkaynak, A. (2020). The impacts of climate change on the runoff volume of Melen and Munzur Rivers in Turkey based on calibration of WASMOD model with multiobjective genetic algorithm. *Meteorology and Atmospheric Physics*, *132*(1), 85–98. <https://doi.org/10.1007/S00703-019-00676-7/TABLES/3>
- OECD. (2013). Water and Climate Change Adaptation: Policies to Navigate Uncharted Waters. *OECD Studies on Water*, OECD Publishing. <https://doi.org/10.1787/9789264200449-EN>
- O’Neill, B. C., Tebaldi, C., Van Vuuren, D. P., Eyring, V., Friedlingstein, P., Hurtt, G., Knutti, R., Kriegler, E., Lamarque, J. F., Lowe, J., Meehl, G. A., Moss, R., Riahi, K., & Sanderson, B. M. (2016). The Scenario Model Intercomparison Project (ScenarioMIP) for CMIP6. *Geoscientific Model Development*, *9*(9), 3461–3482. <https://doi.org/10.5194/GMD-9-3461-2016>
- Ozkul, S. (2009). Assessment of climate change effects in aegean river basins: The case of gediz and buyuk menderes basins. *Climatic Change*, *97*(1), 253–283. <https://doi.org/10.1007/S10584-009-9589-Z/METRICS>
- Parmesan, C., Morecroft, M. D., Trisurat, Y., Langsdorf, S., Lösckke, S., Möller, V., Okem, A., Officer, S., Rama, B., Belling, D., Dieck, W., Götze, S., Kersher, T., Mangele, P., Maus, B., Mühle, A., Nabiyeva, K., Nicolai, M., Niebuhr, A., ... Weyer, N. (2022). *Climate Change 2022:Impacts, Adaptation and Vulnerability Working Group II Contribution to the Sixth Assessment Report of the Intergovernmental Panel on Climate Change*. <https://hal.science/hal-03774939>

- Press, W. H. , F. B. P. , T. S. A. , and V. W. T. (1992). *Numerical recipes in FORTRAN: The art of scientific computing* (2nd edition). Cambridge University Press.
- Ranit, A. B., Durge, P. V, Sangita, M., & Ranit, A. (2014). Overview of Hydrology with Hydrological Models and Modeling. *International Journal of Engineering Research & Technology*, 3(2).
<https://doi.org/10.17577/IJERTV3IS21010>
- Rinsema, J. G. (2014). *Comparison of rainfall runoff models for the Florentine Catchment*. <http://www.discovertasmania.com.au/attraction/lakemeadowbank>
- Saber, M., & Yilmaz, K. K. (2018). Evaluation and Bias Correction of Satellite-Based Rainfall Estimates for Modelling Flash Floods over the Mediterranean region: Application to Karpuz River Basin, Turkey. *Water* 2018, Vol. 10, Page 657, 10(5), 657. <https://doi.org/10.3390/W10050657>
- Schneck, R., Reick, C. H., & Raddatz, T. (2013). Land contribution to natural CO₂ variability on time scales of centuries. *Journal of Advances in Modeling Earth Systems*, 5(2), 354–365. <https://doi.org/10.1002/JAME.20029>
- SEI. (2017). *An Agenda of Action*. www.klimatkalkylatorn.se
- Seibert, J. (2000). Multi-criteria calibration of a conceptual runoff model using a genetic algorithm. *Hydrology and Earth System Sciences*, 4(2), 215–224.
<https://doi.org/10.5194/HESS-4-215-2000>
- Seibert, J. (2005) *HBV Light Version 2. User's Manual*. Department of Physical Geography and Quaternary Geology, Stockholm University, Stockholm. - *References - Scientific Research Publishing*. (n.d.). Retrieved August 8, 2023, from
[https://www.scirp.org/\(S\(351jmbntvnsjt1aadkposzje\)\)/reference/ReferencesPapers.aspx?ReferenceID=2014466](https://www.scirp.org/(S(351jmbntvnsjt1aadkposzje))/reference/ReferencesPapers.aspx?ReferenceID=2014466)

- Seibert, J., & Bergström, S. (2022). A retrospective on hydrological catchment modelling based on half a century with the HBV model. *Hydrology and Earth System Sciences*, 26(5), 1371–1388. <https://doi.org/10.5194/HESS-26-1371-2022>
- Sitterson, J., Knightes, C., Parmar, R., Wolfe, K., Avant, B., Overview, A., & Muche, M. (2018). *An Overview of Rainfall-Runoff Model Types An Overview of Rainfall-Runoff Model Types An Overview of Rainfall-Runoff Model Types*. 41. <https://scholarsarchive.byu.edu/iemssconferencehttps://scholarsarchive.byu.edu/iemssconference/2018/Stream-C/41Thisoralpresentation>
- Soriano, E., Mediero, L., & Garijo, C. (2019). Selection of Bias Correction Methods to Assess the Impact of Climate Change on Flood Frequency Curves. *Water* 2019, Vol. 11, Page 2266, 11(11), 2266. <https://doi.org/10.3390/W11112266>
- Stevens, B., Giorgetta, M., Esch, M., Mauritsen, T., Crueger, T., Rast, S., Salzmann, M., Schmidt, H., Bader, J., Block, K., Brokopf, R., Fast, I., Kinne, S., Kornblueh, L., Lohmann, U., Pincus, R., Reichler, T., & Roeckner, E. (2013). Atmospheric component of the MPI-M Earth System Model: ECHAM6. *Journal of Advances in Modeling Earth Systems*, 5(2), 146–172. <https://doi.org/10.1002/JAME.20015>
- SYGM. (2016). *İklim Değişikliğinin Su Kaynaklarına Etkisi Projesi*. https://www.tarimorman.gov.tr/SYGM/Belgeler/iklim%20de%C4%9Fi%C5%9Fikli%C4%9Finin%20su%20kaynaklar%C4%B1na%20etkisi/Iklim_NihaiRapor.pdf
- SYGM. (2020a). *Çoruh Havzası Taşkın Yönetim Planı*.
- SYGM. (2020b). *Çoruh ve Doğu Karadeniz Havzaları Taşkın Yönetim Planının Hazırlanması Projesi*.

SYGM. (2020c). *İklim Değişikliği ve Uyum*.

<https://www.tarimorman.gov.tr/SYGM/Belgeler/iklim%20de%C4%9Fi%C5%9Fikli%C4%9Finin%20su%20kaynaklar%C4%B1na%20etkisi/iklimkitap2020.pdf>

Tashie, A., Pavelsky, T., & Kumar, M. (2022). A Calibration-Free Groundwater Module for Improving Predictions of Low Flows. *Water Resources Research*, 58(3), e2021WR030800. <https://doi.org/10.1029/2021WR030800>

T.C. KTB. (n.d.). *Artvin Çoruh River*. Retrieved August 9, 2023, from <https://www.ktb.gov.tr/EN-99421/artvin-coruh-river.html>

Te Linde, A. H., Aerts, J. C. J. H., Hurkmans, R. T. W. L., & Eberle, M. (2008). Comparing model performance of two rainfall-runoff models in the Rhine basin using different atmospheric forcing data sets. *Hydrology and Earth System Sciences*, 12(3), 943–957. <https://doi.org/10.5194/HESS-12-943-2008>

Teutschbein, C., & Seibert, J. (2012). Bias correction of regional climate model simulations for hydrological climate-change impact studies: Review and evaluation of different methods. *Journal of Hydrology*, 456–457, 12–29. <https://doi.org/10.1016/J.JHYDROL.2012.05.052>

The Water Cycle | U.S. Geological Survey. (n.d.). Retrieved August 8, 2023, from <https://www.usgs.gov/special-topics/water-science-school/science/water-cycle>

The World Bank. (2009). *World Development Report 2010*. The World Bank. <https://doi.org/10.1596/978-0-8213-7987-5>

Thornthwaite, C. W. (1948). An Approach toward a Rational Classification of Climate. *Geographical Review*, 38(1), 55. <https://doi.org/10.2307/210739>

Tibangayuka, N., Mulungu, D. M. M., & Izdori, F. (2022). Evaluating the performance of HBV, HEC-HMS and ANN models in simulating streamflow for a data scarce high-humid tropical catchment in Tanzania.

- <https://doi.org/10.1080/02626667.2022.2137417>, 67(14), 2191–2204.
<https://doi.org/10.1080/02626667.2022.2137417>
- TRMM. (n.d.). Retrieved August 7, 2023, from <https://trmm.gsfc.nasa.gov/>
- UN. (n.d.). What Is Climate Change? | United Nations. *United Nations*. Retrieved August 9, 2023, from <https://www.un.org/en/climatechange/what-is-climate-change>
- Vaze, M. J., & Banerjee, J. (2012). Prediction of liquid height for onset of slug flow. *The Canadian Journal of Chemical Engineering*, 90(5), 1295–1303.
<https://doi.org/10.1002/CJCE.20626>
- Willmott, C. J., Rowe, C. M., & Mintz, Y. (1985). Climatology of the terrestrial seasonal water cycle. *Journal of Climatology*, 5(6), 589–606.
<https://doi.org/10.1002/JOC.3370050602>
- Yilmaz, M. (2023a). Accuracy assessment of temperature trends from ERA5 and ERA5-Land. *Science of the Total Environment*, 856.
<https://doi.org/10.1016/J.SCITOTENV.2022.159182>
- Yilmaz, M. (2023b). Consistency of spatiotemporal variability of MODIS and ERA5-Land surface warming trends over complex topography. *Environmental Science and Pollution Research International*, 30(41), 94414–94435.
<https://doi.org/10.1007/S11356-023-28983-Y>
- Yilmaz, M., Alp, H., Fatih Tosunoğlu, ·, Ömer, ·, Aşıkoğlu, L., Eriş, · Ebru, & Eriş, E. (2022). Impact of climate change on meteorological and hydrological droughts for Upper Coruh Basin, Turkey. *Natural Hazards*, 112, 1039–1063.
<https://doi.org/10.1007/s11069-022-05217-x>
- Young, P. C. (2020). *Real-Time Flow Forecasting*.
- Yucel, I., Güventürk, A., & Sen, O. L. (2015a). Climate change impacts on snowmelt runoff for mountainous transboundary basins in eastern Turkey.

International Journal of Climatology, 35(2), 215–228.

<https://doi.org/10.1002/JOC.3974>

Yucel, I., Güventürk, A., & Sen, O. L. (2015b). Climate change impacts on snowmelt runoff for mountainous transboundary basins in eastern Turkey.

International Journal of Climatology, 35(2), 215–228.

<https://doi.org/10.1002/JOC.3974>

APPENDICES

A. Parameters of The Trained HBV Models

Calibration Parameters for HBV-LIGHT for ERA5-Land

Sub-Basins	TT	CFMAX	PERC	SP	SFCF	CFR	CWH	FC	LP	BETA	UZL	K0	K1	K2	MAXBAS
D23A001	-0.0543	3.9006	13.9968	1.0000	1.9083	0.0000	0.0000	100.0001	0.9507	1.5344	231.3805	0.5280	0.9900	0.0331	75.3369
D23A003	-1.5338	8.0631	92.3222	0.7111	4.4019	1.7507	4.4699	16.4107	0.1512	0.8973	40.8505	0.9900	0.6425	0.0467	80.3009
D23A016	-1.8814	5.6996	1.1824	0.5256	0.6554	4.0914	0.0100	446.6471	0.9299	6.3239	519.9288	0.0821	0.3234	0.0275	38.8366
D23A026	1.2448	5.3861	91.6759	0.4726	2.3255	4.3793	0.0137	10.0000	0.8768	9.0500	454.8443	0.2931	0.4597	0.0256	69.3431
D23A031	1.5850	8.7241	20.1907	1.0000	4.3734	3.8758	4.3439	10.0002	0.8249	0.1376	458.4883	0.2730	0.8793	0.0016	94.3964
D23A032	-1.0331	5.1995	15.9949	0.3614	4.1368	5.0000	0.3699	999.9975	0.8706	0.0982	4.6246	0.8256	0.9355	0.0428	91.0919
D23A037	0.1343	9.2805	1.1130	0.8299	3.0720	4.3190	0.9151	246.0682	0.7596	1.8948	301.9488	0.3784	0.6403	0.0006	70.1842
E23A004	-1.5231	9.5127	49.0518	0.1250	2.6221	5.0000	2.4304	21.3652	0.3302	0.6096	53.8598	0.9900	0.7442	0.0349	75.6741
E23A005	-1.8284	8.1823	21.3316	0.5475	2.1387	4.9513	0.0100	100.2230	0.2875	0.5426	436.0273	0.4399	0.3597	0.0444	47.9664
E23A016	1.1572	9.1317	21.0231	0.1096	2.1538	4.2004	0.0100	124.9179	0.1171	0.4741	502.8868	0.2689	0.9097	0.0458	51.2069
E23A020	-1.5482	0.5111	74.8644	0.4535	0.4703	0.0010	0.0100	272.4698	0.5284	2.6937	248.2484	0.7296	0.7908	0.8396	40.7400
E23A021	2.5069	8.6053	27.0216	0.9221	4.7267	0.3377	3.0604	404.1044	1.0000	0.0500	234.5357	0.9900	0.9012	0.0008	100.0000
E23A022	-0.4952	8.3133	19.8560	1.0000	1.9763	5.0000	0.2074	57.5676	0.3965	0.5780	165.3240	0.0436	0.9900	0.0782	92.9772
E23A023	0.3407	9.9999	10.5104	0.4356	2.9867	4.0037	0.0223	985.1166	0.5300	1.0465	530.1400	0.0465	0.9900	0.0486	64.9341
E23A025	-1.5500	3.1740	98.3801	0.2639	0.6758	4.9668	0.6243	51.3480	0.1492	0.7937	424.0384	0.2514	0.1259	0.0456	29.1456
E23A026	1.1770	9.3983	17.9020	1.0000	5.0000	0.0010	0.0100	10.0000	1.0000	0.0500	321.7883	0.2645	0.4746	0.0655	77.8426
E23A027	0.7479	9.9999	9.6862	0.8833	4.3253	0.0010	3.2519	68.2169	0.9999	0.0500	347.4325	0.4783	0.9900	0.0004	95.5289
E23A028	-0.3404	4.8994	21.3841	0.4815	1.7854	2.1318	0.6078	179.4187	1.0000	2.2721	480.5834	0.1569	0.9900	0.0401	69.8208
E23A029	0.9015	8.5669	0.6678	0.6950	2.1456	4.9998	4.8575	584.6831	0.5596	2.5406	336.3131	0.9898	0.9549	0.0001	72.7817
E23A030	-0.7088	4.1306	70.6650	0.1573	2.7766	4.7632	3.3425	128.2171	1.0000	3.1099	28.4915	0.9398	0.8249	0.0241	97.6640
E23A031	1.4230	9.6818	1.0659	1.0000	5.0000	0.7442	0.0203	10.0000	1.0000	0.0500	230.6107	0.0050	0.9900	0.0001	71.6596
E23A033	-0.6981	7.9224	20.6928	0.6799	1.5044	0.1390	0.0100	153.8039	0.7704	1.8311	399.1499	0.4140	0.1695	0.0342	43.4310
E23A034	-0.6258	8.1492	28.6241	0.8669	4.1872	0.0010	0.0100	10.0005	1.0000	0.3903	0.0001	0.9900	0.8516	0.0324	73.7385
E23A035	0.4679	5.9077	90.2936	0.7536	1.8812	0.0169	0.0100	185.7084	0.7165	0.6430	262.2837	0.2889	0.3161	0.0617	61.7960
E23A036	0.2313	7.0757	68.1341	0.3636	3.8365	3.6091	0.9861	58.1241	0.5524	2.0734	0.0000	0.9408	0.9333	0.0189	87.6967
E23A037	4.4647	4.3665	73.1831	0.0084	0.4634	1.3492	0.3163	422.1146	0.7762	11.6781	697.5402	0.5315	0.3248	0.0221	6.6441
E23A038	-1.1549	2.8245	44.3204	0.0000	1.4251	4.9998	0.4043	65.8471	0.2560	0.7793	477.7035	0.4682	0.0603	0.0280	1.8309
E23A039	-1.0774	9.1354	64.1462	0.8415	5.0000	4.6910	0.0100	10.0000	1.0000	0.0500	352.4236	0.3885	0.0751	0.0202	1.0000
E23A040	0.7867	8.4780	19.5863	0.5782	2.2080	4.8266	0.0100	84.6137	0.4677	1.0137	0.0001	0.9900	0.9900	0.0344	72.1750
E23A042	-0.1517	7.4270	25.3831	1.0000	4.9994	0.0010	0.0100	43.1412	1.0000	0.4986	338.0748	0.5128	0.1686	0.0268	99.1648
Mean	0.0321	7.0549	37.1416	0.6022	2.8387	2.8051	1.0118	195.3375	0.6934	1.7918	295.9841	0.5163	0.6599	0.0575	65.3636

Calibration Parameters for HBV-LIGHT GCM-HADGEM Historical

Sub-Basins	TT	CFMAX	PERC	SP	SFCF	CFR	CWH	FC	LP	BETA	UZL	K0	K1	K2	MAXBAS
D23A001	-0.8389	3.1888	11.4921	0.9583	1.4732	0.0000	0.0000	101.3778	1.0000	1.0000	439.4922	0.3747	0.9900	0.0419	77.9016
D23A026	1.1982	6.4544	65.0256	0.9913	2.8689	1.7363	2.4962	10.0000	0.8773	1.2123	188.4946	0.9900	0.5585	0.0190	90.3950
D23A031	5.7136	7.7264	41.1389	0.3426	4.2159	0.4392	5.0000	204.5921	0.0502	0.1390	520.2184	0.3165	0.6170	0.0007	76.3667
D23A032	0.6242	4.3084	23.2495	0.5578	3.5358	3.2630	2.8393	999.9995	1.0000	0.2227	0.0000	0.9900	0.9900	0.0018	100.0000
D23A037	0.7192	8.6683	27.3824	0.5836	3.4768	1.2517	1.0722	509.1778	0.6768	1.3079	17.3097	0.9900	0.9900	0.0591	65.7719
E23A004	3.1270	7.1138	21.8299	0.5034	3.1056	1.0875	0.3038	999.9985	1.0000	0.8506	176.9411	0.0673	0.1570	0.0231	54.2057
E23A005	3.2677	4.3216	34.2626	1.0000	1.3969	0.0147	0.0100	47.9487	0.0422	0.2358	623.0931	0.9174	0.4868	0.0366	69.7461
E23A016	0.8690	3.8618	25.9737	0.8631	1.5640	4.9999	1.2692	257.6926	0.7234	0.5429	462.2062	0.0033	0.9900	0.1032	89.3067
E23A020	2.6337	4.6214	81.9742	0.1773	1.4839	4.9995	1.6906	383.8402	0.7539	0.9495	176.6874	0.8265	0.7381	0.1917	83.5179
E23A021	1.3239	4.1369	30.4775	1.0000	2.8601	0.0010	0.0100	39.8287	1.0000	0.5933	290.0248	0.1825	0.6856	0.0264	89.7420
E23A022	1.0527	6.9503	99.9999	0.4442	1.7300	3.4397	3.7834	56.7490	0.6005	1.4609	231.6936	0.1615	0.3285	0.0163	58.2419
E23A023	0.0468	6.3981	40.3693	0.0654	1.6389	1.3261	4.4762	663.0143	0.6979	1.1044	527.1304	0.4534	0.9900	0.0390	62.5768
E23A026	0.4412	9.9995	38.1181	1.0000	2.8907	0.0010	0.0100	470.1314	0.9998	0.1830	354.1271	0.1065	0.9900	0.0689	79.6987
E23A027	-1.6790	6.2160	25.0953	0.1166	1.8070	3.0323	1.4815	14.3232	1.0000	3.0971	0.0000	0.9345	0.9898	0.0118	99.9999
E23A028	-0.3549	10.0000	96.7752	1.0000	1.8215	1.0080	0.0773	392.4478	0.4736	0.7622	325.5671	0.2790	0.3079	0.0309	49.5745
E23A029	-0.2483	4.9693	97.5710	0.8281	1.5787	4.9999	0.1937	845.9703	0.5626	0.9693	479.2166	0.3816	0.0752	0.0724	65.7619
E23A030	3.2846	8.1780	58.5211	0.7990	2.7056	0.0292	1.7130	61.8960	1.0000	1.2166	278.7104	0.9899	0.1954	0.0217	89.8620
E23A031	-0.3788	9.5084	32.9967	0.8926	3.7850	0.1476	0.1820	999.9942	1.0000	0.0500	0.0001	0.5374	0.9809	0.0274	59.1714
E23A033	-1.1481	7.8345	41.9590	0.4399	1.3275	5.0000	0.4782	147.6673	0.7624	0.9488	601.6084	0.4146	0.9900	0.0275	75.2173
E23A034	-1.0921	9.0787	21.5611	0.0714	2.7199	1.6779	0.7181	999.9918	0.4979	1.5960	2.0792	0.9900	0.9900	0.0239	89.2766
E23A035	1.6858	5.7064	32.9609	0.5130	1.9490	0.5560	3.6514	709.2653	0.8954	1.6833	452.0625	0.6139	0.9900	0.0411	68.8778
E23A036	2.8286	5.3037	15.3536	1.0000	2.5535	0.5319	0.0100	384.5213	1.0000	0.3413	191.5595	0.1609	0.5317	0.0556	98.6059
E23A037	3.2077	6.0152	37.2742	0.9921	1.1067	4.7595	1.3766	10.0000	0.2492	0.7505	618.2143	0.2416	0.6726	0.0282	75.9017
E23A038	1.0209	5.4222	30.4486	0.9886	1.8494	2.5701	3.9874	561.6164	0.6922	0.8808	334.8541	0.3984	0.9325	0.0553	75.5819
E23A040	2.0097	8.9391	33.9752	0.5738	2.0086	5.0000	0.2818	206.1198	0.5680	1.0427	465.0635	0.3727	0.9900	0.0600	80.0370
E23A042	4.0521	9.1649	30.9575	0.9364	4.3943	0.0010	0.0100	929.0580	1.0000	1.6416	378.9286	0.5122	0.0001	0.0202	53.0224
Mean	1.2833	6.6956	42.1824	0.6784	2.3787	1.9951	1.4278	423.3547	0.7355	0.9532	312.8955	0.5079	0.6984	0.0425	76.0908

Calibration Parameters for HBV-LIGHT GCM-GFDL Historical

Sub-Basins	TT	CFMAX	PERC	SP	SFCF	CFR	CWH	FC	LP	BETA	UZL	K0	K1	K2	MAXBAS
D23A001	0.5540	2.8506	5.4669	0.9975	1.9536	0.0000	0.0000	399.9940	1.0000	1.0000	376.7372	0.1515	0.6370	0.0403	79.4427
D23A026	1.6735	5.2686	68.4822	0.8056	4.1240	4.1865	1.3930	10.0020	0.2286	0.4299	37.3432	0.9900	0.7770	0.0278	98.2467
D23A031	2.7991	3.8194	34.0748	0.8809	5.0000	0.2093	0.1675	10.0687	0.1515	0.0001	4.7145	0.9900	0.9900	0.0456	93.0107
D23A032	-0.6135	9.2012	7.0417	0.0181	2.3789	0.1804	4.1041	93.8899	1.0000	0.0638	237.4615	0.3071	0.0001	0.8000	46.8645
D23A037	4.7275	6.6775	2.0730	0.6051	2.7014	4.9993	3.6925	190.5540	1.0000	0.9349	280.2407	0.0859	0.9900	0.0003	70.3147
E23A004	5.7459	5.2746	27.8578	0.8715	2.1021	0.0127	0.0118	10.0000	0.7158	1.1047	4.5936	0.9900	0.9900	0.0208	63.4025
E23A005	-1.1041	1.0908	15.8191	0.9695	4.7922	0.0010	0.6219	73.4609	0.1969	0.5417	401.3425	0.0236	0.9899	0.0508	95.3058
E23A016	1.0521	5.8213	29.4933	0.9822	4.3965	2.8489	0.5730	346.9156	0.8211	1.2312	0.0015	0.9900	0.9900	0.0554	94.7627
E23A020	4.0740	4.0581	20.2349	0.3536	2.8887	1.2663	2.3922	209.2239	1.0000	8.5206	67.4544	0.9900	0.7435	0.0035	81.0496
E23A021	4.1112	7.1362	68.2101	0.9976	3.1758	0.0010	0.0100	10.0000	0.2076	0.5997	0.9937	0.9899	0.4620	0.0216	77.1661
E23A022	1.7599	8.9221	72.3525	0.6259	2.1925	3.0638	2.9019	110.5022	0.6365	0.9032	572.5522	0.5947	0.9900	0.0488	99.9247
E23A023	2.1468	5.1318	46.1590	0.4666	2.2781	2.0287	4.5767	178.7739	0.8867	19.9996	196.9468	0.0377	0.9365	0.0001	100.0000
E23A026	-1.1008	8.4658	47.3700	1.0000	5.0000	0.0010	0.5280	688.9212	1.0000	0.3392	32.5222	0.6676	0.2076	0.0591	99.9997
E23A027	-0.8257	8.7136	52.5379	0.1539	2.9973	2.1088	1.3744	552.7625	0.8922	1.8312	8.9215	0.9253	0.8792	0.0352	97.9825
E23A028	0.6029	8.1681	53.1771	0.5851	2.0938	4.1881	1.4562	271.5982	0.9187	1.4773	0.0007	0.8299	0.8400	0.0577	93.9911
E23A029	-0.9585	2.3126	82.2867	0.9603	3.0704	5.0000	0.0719	740.2392	0.5969	1.3106	259.9009	0.2987	0.4473	0.9899	98.6843
E23A030	0.3550	2.3599	36.7430	1.0000	5.0000	1.1041	0.7125	10.2050	1.0000	0.8871	5.6650	0.9900	0.9900	0.0375	100.0000
E23A031	0.6195	10.0000	56.3077	1.0000	5.5308	0.0010	0.0112	999.9965	1.0000	0.0806	604.8502	0.3200	0.9900	0.1662	94.3118
E23A033	1.0419	6.2617	33.1048	0.2889	1.3203	2.9634	1.8607	241.1735	0.8928	1.5466	499.4501	0.3727	0.9900	0.0026	84.9661
E23A034	-1.1008	7.2838	95.5812	0.7768	2.5080	5.0000	0.4650	229.4531	1.0000	1.5645	238.8614	0.0883	0.4528	0.0222	72.1143
E23A035	0.7849	3.6488	49.7439	0.7224	3.7073	2.4342	4.7487	1717.4024	0.9296	3.0300	0.0000	0.8194	0.9890	0.0506	75.7897
E23A036	1.1593	4.8659	50.5782	0.8405	4.8719	2.7960	1.4227	999.9998	1.0000	0.6330	370.0241	0.3097	0.9900	0.0458	86.7344
E23A037	2.5321	5.0330	76.1696	0.8005	2.4375	4.9998	2.5473	108.6963	0.6763	0.9368	347.5312	0.4716	0.9900	0.0855	98.2067
E23A038	3.0275	7.2559	29.1109	0.7379	3.8647	4.9996	1.6438	999.9995	0.6584	1.3396	159.7266	0.5217	0.9900	0.0934	87.8917
E23A040	-0.0170	2.5939	49.0998	0.9661	3.2490	3.7892	3.0137	27.8816	0.6836	2.8430	454.6844	0.4570	0.9688	0.0262	61.1137
E23A042	3.9159	6.9342	56.6939	0.3316	4.1888	2.2645	1.0659	112.6909	1.0000	0.8124	273.5956	0.0280	0.8278	0.0222	82.4775
Mean	1.4216	5.7365	44.8373	0.7207	3.3778	2.3249	1.5910	359.4002	0.7728	2.0754	209.0814	0.5477	0.8096	0.1080	85.9136

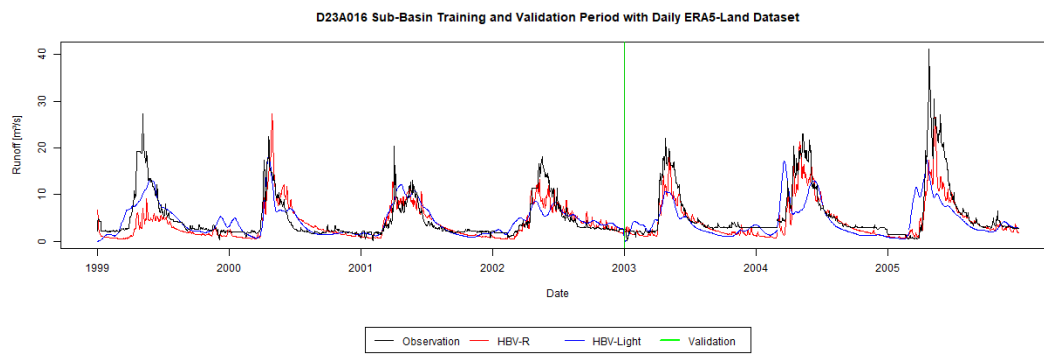
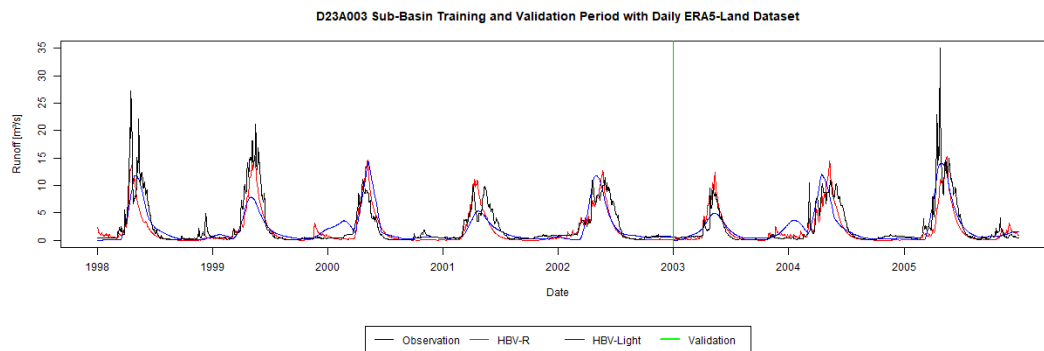
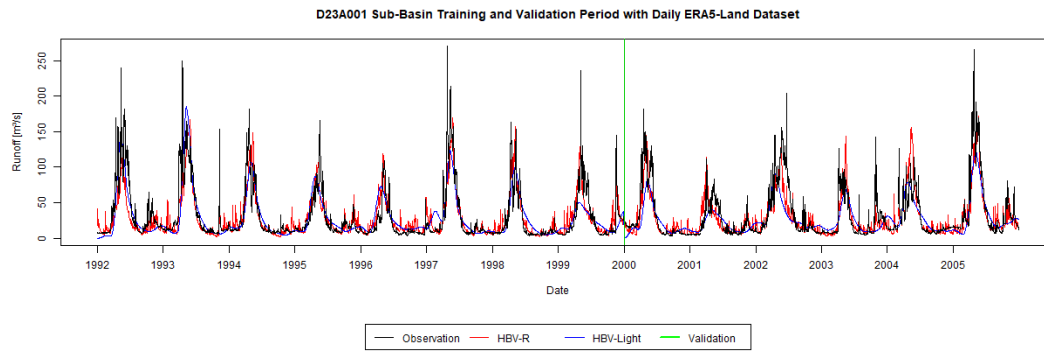
Calibration Parameters for HBV-LIGHT GCM-MPI Historical

Sub-Basins	TT	CFMAX	PERC	SP	SFCF	CFR	CWH	FC	LP	BETA	UZL	K0	K1	K2	MAXBAS
D23A001	-0.5929	4.0000	20.8304	0.9986	1.4661	0.0000	0.0000	272.9217	1.0000	1.0000	251.7739	0.3150	0.1520	0.0312	44.6372
D23A026	2.4975	6.2811	14.1403	0.6813	3.1941	4.7879	1.6923	999.9142	0.7656	0.6474	626.9671	0.3276	0.9900	0.0033	99.6495
D23A031	1.8511	5.2019	7.7685	0.7156	3.4335	3.5845	3.3928	999.9975	1.0000	0.1305	135.7149	0.6111	0.7935	0.0176	95.5049
D23A032	-0.6842	5.7811	29.6965	0.4618	4.0930	4.7382	0.6361	550.9127	0.6476	0.4056	21.0970	0.9900	0.9900	0.0130	81.3045
D23A037	-0.4243	8.2834	12.7918	0.7923	2.4177	4.9128	0.5658	421.8499	0.7414	0.8970	20.2352	0.9900	0.9900	0.1022	75.0712
E23A004	1.2778	8.7783	75.0231	0.8667	2.1051	3.4784	2.8371	547.1272	0.5795	0.2492	305.3587	0.3268	0.9900	0.0547	91.6884
E23A005	2.0254	8.8953	90.3385	0.5876	1.9182	4.9999	1.0723	108.2886	0.4831	1.0067	486.8590	0.2361	0.3729	0.0241	76.6212
E23A016	3.1507	9.2876	7.2852	0.6656	1.4015	0.7619	0.8197	227.9416	1.0000	0.9010	481.9824	0.2363	0.0001	0.3379	100.0000
E23A020	2.3225	4.8603	79.6561	0.5203	1.7579	3.5820	3.4968	430.4944	0.4644	0.6984	459.5999	0.5262	0.9162	0.3329	89.2468
E23A021	-0.2825	4.3276	44.9290	1.0000	3.5227	2.2797	0.0630	32.3241	0.3885	0.4699	331.1088	0.3281	0.8237	0.0247	100.0000
E23A022	-0.6834	6.8343	56.6808	0.4635	3.0317	4.9330	1.5927	711.6631	0.7853	1.3915	219.7176	0.0858	0.9900	0.0443	97.1107
E23A023	-0.5890	4.4658	20.4876	0.5125	1.1258	0.8060	0.8971	419.4588	0.5925	0.8372	4.5445	0.9900	0.4027	0.0947	90.8529
E23A026	-0.4784	6.5767	9.4165	1.0000	2.5960	0.0010	0.0155	10.0000	1.0000	0.2655	632.2595	0.4075	0.6639	0.0378	99.5850
E23A027	-1.6934	9.5535	86.2577	0.1689	1.6928	4.9983	1.2260	82.7341	0.7262	1.2039	22.9913	0.9900	0.3578	0.0226	92.5820
E23A028	-0.7731	9.8002	23.7265	0.4842	1.5872	0.8078	0.8598	264.8488	1.0000	1.9507	25.2182	0.9900	0.5586	0.0458	97.5287
E23A029	-0.9442	8.7945	47.6104	0.7356	1.1390	1.3744	1.8669	321.1837	0.8112	1.2156	0.0001	0.9900	0.9900	0.0801	84.7422
E23A030	1.8762	6.5102	23.2778	0.8050	3.3476	0.5971	2.0881	749.9407	1.0000	0.8175	438.6537	0.2141	0.2220	0.0277	99.9993
E23A031	0.3830	10.0000	14.3265	1.0000	3.0567	0.0010	0.0100	999.9936	1.0000	0.0555	464.7130	0.1021	0.8265	0.0257	71.9290
E23A033	-0.5465	8.3523	18.8048	0.9378	1.2532	5.0000	0.3337	205.4460	0.5637	0.6253	235.4763	0.6371	0.9900	0.0268	85.5997
E23A034	-1.2899	6.6463	20.4699	0.3359	1.6049	2.6676	0.3207	261.9702	1.0000	1.0927	21.9746	0.4967	0.9328	0.0276	89.0700
E23A035	-0.5036	4.7349	17.6790	0.9548	1.5696	3.7041	3.1713	422.9628	0.7236	0.9833	0.0000	0.9900	0.9500	0.0858	86.2733
E23A036	2.9387	9.2361	60.5533	0.8755	2.3458	0.2794	2.8988	41.2556	1.0000	4.2993	187.5544	0.9900	0.2285	0.0125	97.4269
E23A037	1.7803	7.2998	19.1766	0.7047	2.2535	0.6045	0.6901	592.3245	0.7582	1.1780	593.7646	0.0003	0.0001	0.2276	100.0000
E23A038	2.1086	5.9356	75.2768	0.5663	1.9340	7.7127	4.9997	453.7898	0.4843	0.8081	429.0811	0.0418	0.2398	0.1003	82.9356
E23A040	-0.0440	7.4123	2.4245	0.7925	2.2736	3.2611	2.8655	347.4564	0.7340	1.3140	90.6483	0.7607	0.0456	0.9900	82.9130
E23A042	2.5994	6.7497	92.0622	1.0000	3.5418	0.0267	0.0100	414.0905	1.0000	0.4832	271.6409	0.0028	0.0566	0.0341	74.6269
Mean	0.5878	7.1000	37.3342	0.7164	2.2947	2.6885	1.4778	418.8804	0.7788	0.9587	259.9590	0.5221	0.5951	0.1087	87.9576

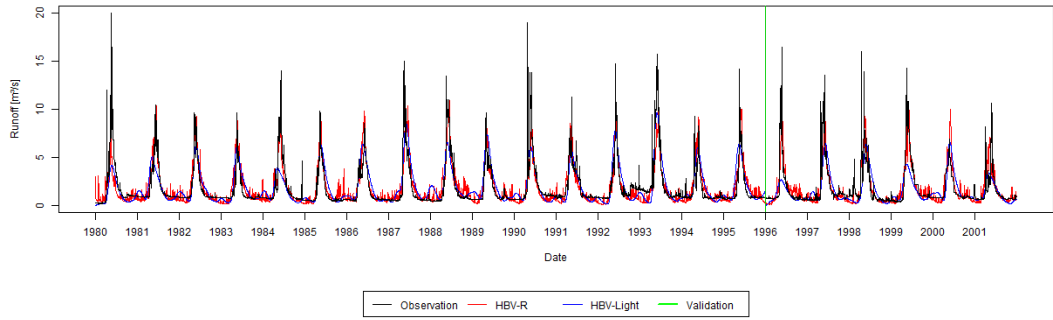
Calibration Parameters for HBV-R Model for ERA5-Land

Sub-Basins	DDF	Fc	beta	k0	l	k1	k2	kp	pwp	Tm	Ts	Tr
D23A001	0.8593	163.2511	1.7421	0.1317	0.1445	0.0511	0.0470	0.3379	187.8157	2.3248	-3.7287	2.5122
D23A003	1.2782	74.9037	4.9084	0.0248	0.1536	0.0698	0.0449	0.3551	59.8633	2.1455	-3.2930	3.6851
D23A016	1.1407	357.9627	3.5343	0.0825	0.3533	0.0343	0.0130	0.1940	116.1545	-0.8201	-2.9688	4.7608
D23A026	0.6639	103.9176	2.6791	0.1497	0.3386	0.0903	0.0329	0.3881	190.1421	2.4141	-3.3667	4.8310
D23A031	1.0391	28.9712	3.2638	0.0250	0.2274	0.0657	0.0465	0.2717	130.1854	2.4394	-4.6754	3.1103
D23A032	0.6793	3.6039	0.0833	0.0815	0.1742	0.0545	0.0201	0.1436	167.8823	2.3977	-3.5838	4.6350
D23A037	0.5344	85.7631	3.3992	0.0222	0.3827	0.0701	0.1177	0.0211	121.9833	0.2151	-2.5729	3.1009
E23A004	0.6680	152.4700	0.3586	0.0832	0.0983	0.0976	0.0386	0.4630	74.7340	0.1347	-4.3028	2.5533
E23A005	0.9610	78.4870	3.3994	0.0104	0.3995	0.0436	0.0406	0.4665	168.5651	-1.4717	-4.1871	2.5705
E23A016	0.3894	70.2712	2.1281	0.0518	0.0626	0.0404	0.0330	0.3508	98.4445	-0.3515	-4.9725	4.9608
E23A020	0.3895	380.8556	2.1910	0.1059	0.1575	0.0374	0.1819	0.0215	60.6407	-1.6468	-4.7008	4.2458
E23A021	0.9395	18.1556	0.4911	0.0454	0.3094	0.0231	0.0332	0.4862	149.2610	2.4577	-4.7282	4.4284
E23A022	0.5806	107.2107	1.8353	0.0256	0.2162	0.0232	0.0292	0.4102	172.1837	0.0525	-4.5063	4.3059
E23A023	0.5146	222.1188	1.1572	0.1223	0.3517	0.0460	0.0438	0.4896	187.9820	-0.3446	-4.2194	4.9837
E23A025	0.3367	264.0838	0.8043	0.0176	0.1279	0.1455	0.0767	0.2267	91.0909	-0.8644	-3.1837	3.4763
E23A026	1.7652	73.4854	0.2296	0.1576	0.3306	0.0757	0.0444	0.4799	128.8923	2.4813	-4.9498	3.7686
E23A027	1.3145	25.6115	0.1865	0.0391	0.1696	0.0964	0.0368	0.3966	153.7440	1.6576	-3.9557	4.9372
E23A028	1.0866	223.9055	1.8211	0.0469	0.2715	0.0155	0.0298	0.2784	124.9666	0.8032	-4.3638	3.2861
E23A029	0.4155	233.7464	1.7749	0.0270	0.3546	0.0665	0.0765	0.4615	161.5002	-0.0006	-3.3909	2.6587
E23A030	1.2291	138.3269	3.8876	0.0186	0.0824	0.0331	0.0283	0.4457	159.7818	2.4685	-4.6889	3.5033
E23A031	4.1118	6.2203	1.5957	0.0842	0.0814	0.1044	0.0132	0.3000	80.2705	2.3177	-4.8956	4.8158
E23A033	0.6506	143.3854	3.2150	0.1157	0.0589	0.0646	0.0180	0.2072	150.5497	0.3813	-4.2357	4.1761
E23A034	1.0715	23.2865	4.9495	0.0900	0.1915	0.0894	0.0308	0.4777	178.1634	1.3469	-4.9606	3.3226
E23A035	0.3355	90.7824	1.6494	0.1156	0.1141	0.0127	0.0310	0.4508	136.1035	0.8660	-3.6201	3.7853
E23A036	1.8357	219.5131	1.2808	0.0145	0.2723	0.0156	0.0148	0.3778	78.6652	2.0463	-4.9072	4.1501
E23A037	0.2618	382.8371	1.8831	0.0144	0.1785	0.0928	0.0324	0.1537	92.7261	-1.3981	-2.6533	4.5769
E23A038	0.8535	142.5948	1.2188	0.0115	0.0635	0.0657	0.0628	0.3503	106.8192	-0.9561	-3.4959	4.3996
E23A039	3.8951	0.3282	1.5449	0.2710	0.0314	0.0554	0.0207	0.4316	127.5980	0.1589	-4.9292	4.1380
E23A040	1.0428	111.4999	2.7158	0.0565	0.1431	0.0645	0.0387	0.4404	195.8334	1.3685	-3.4395	3.0824
E23A042	2.4612	128.6370	4.5409	0.0446	0.1000	0.0356	0.0143	0.4895	126.3496	2.3994	-4.7350	4.6524
Mean	1.1101	135.2062	2.1489	0.0696	0.1980	0.0593	0.0431	0.3456	132.6297	0.8341	-4.0737	3.9138

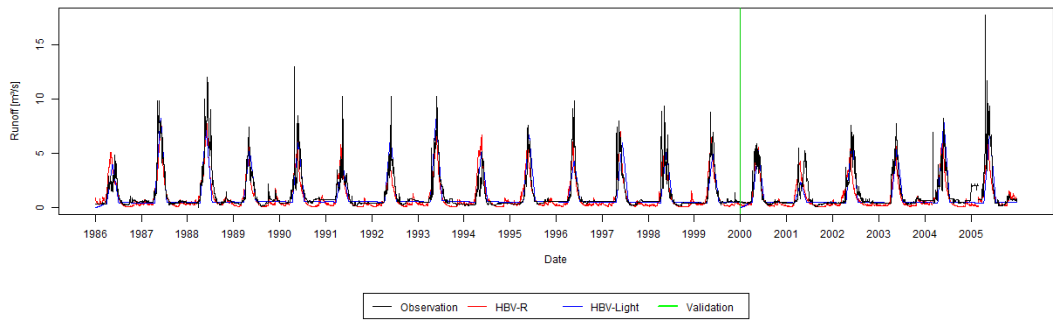
B. ERA5-Land Training and Validation with HBV-R and HBV-Light



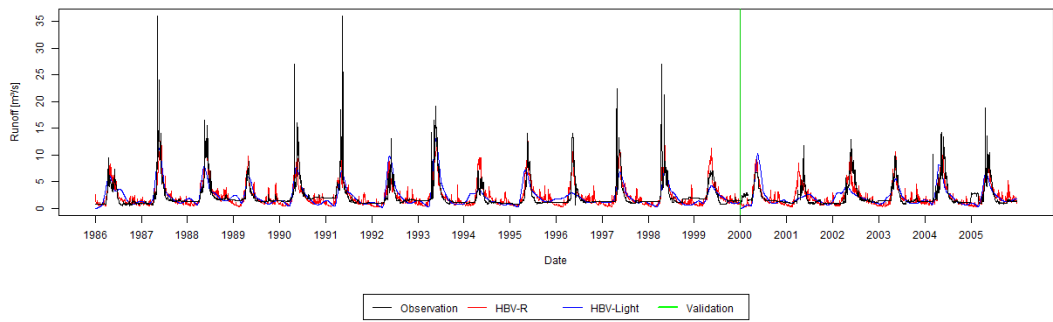
D23A026 Sub-Basin Training and Validation Period with Daily ERA5-Land Dataset



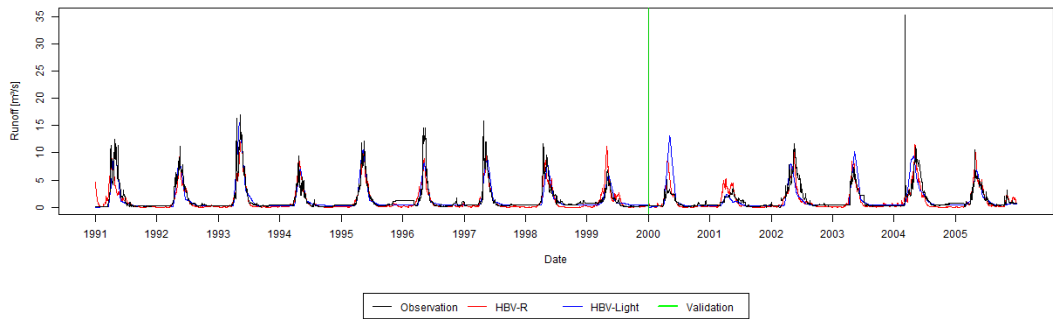
D23A031 Sub-Basin Training and Validation Period with Daily ERA5-Land Dataset



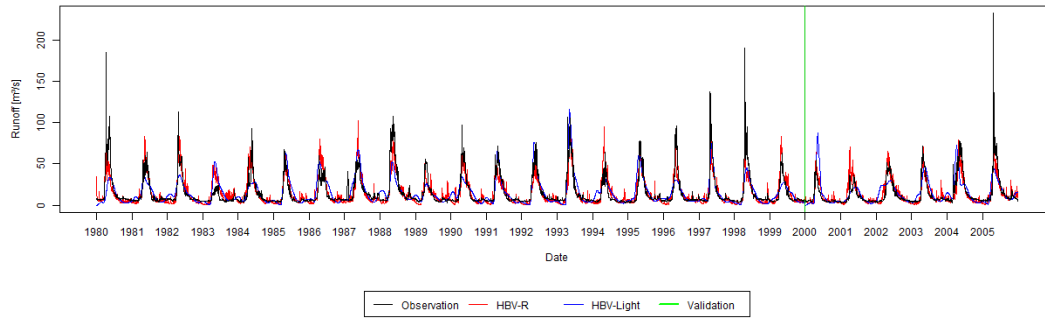
D23A032 Sub-Basin Training and Validation Period with Daily ERA5-Land Dataset



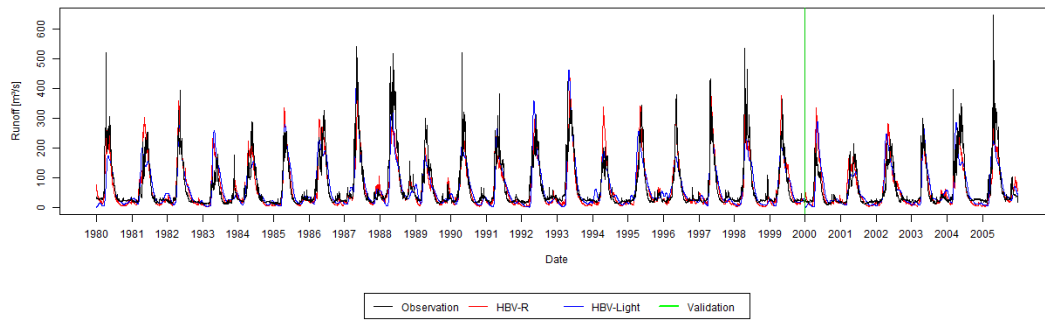
D23A037 Sub-Basin Training and Validation Period with Daily ERA5-Land Dataset



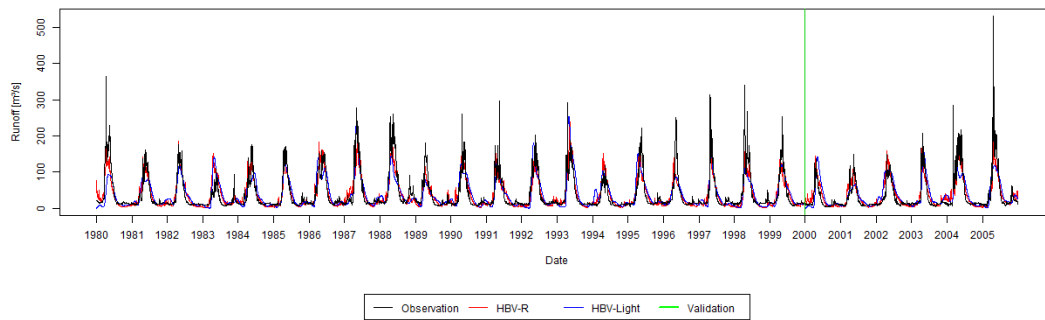
E23A004 Sub-Basin Training and Validation Period with Daily ERA5-Land Dataset



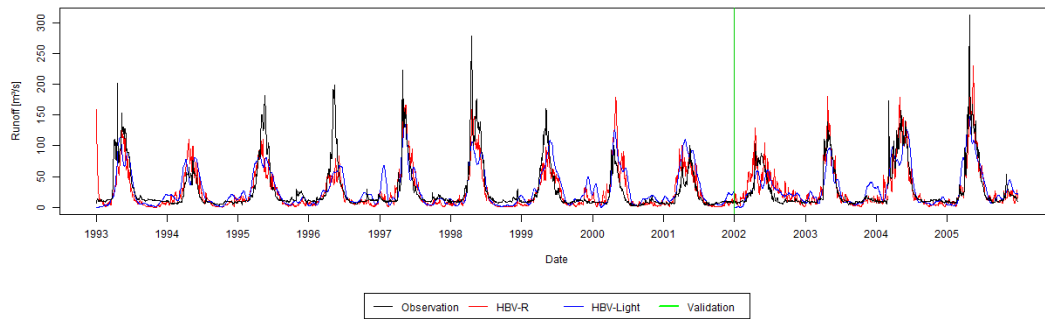
E23A005 Sub-Basin Training and Validation Period with Daily ERA5-Land Dataset

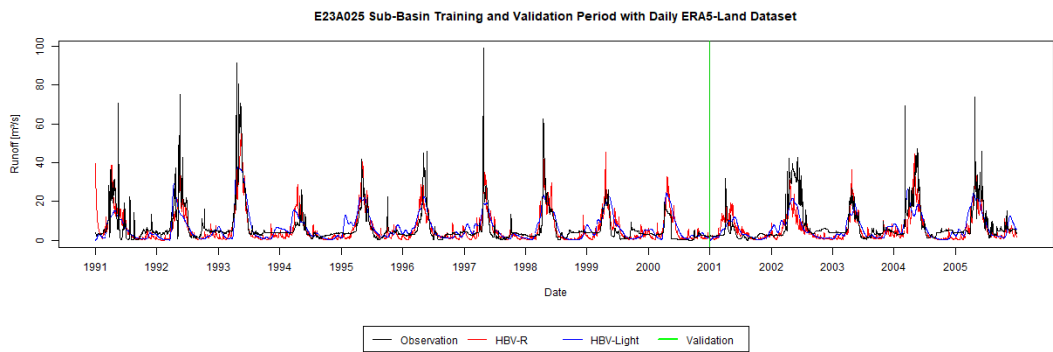
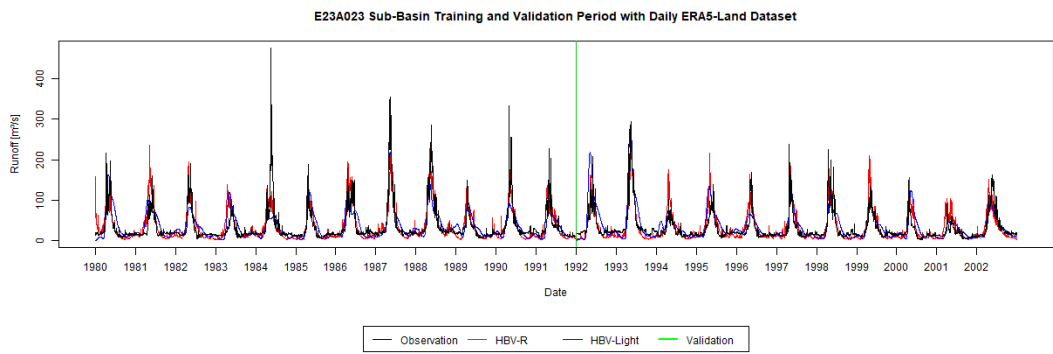
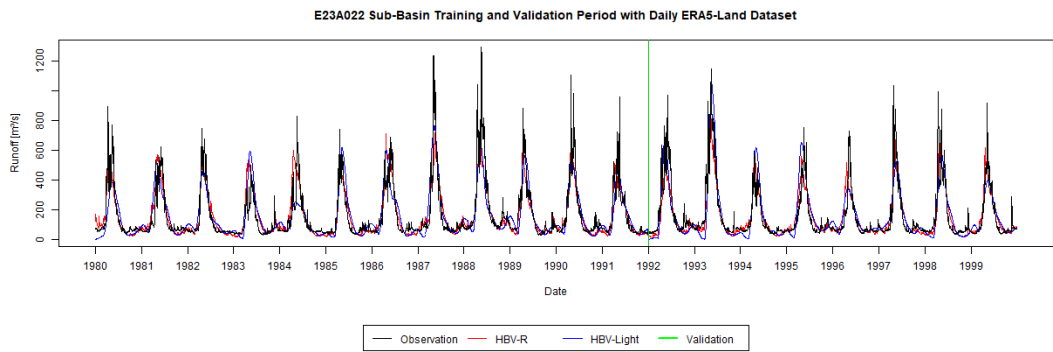
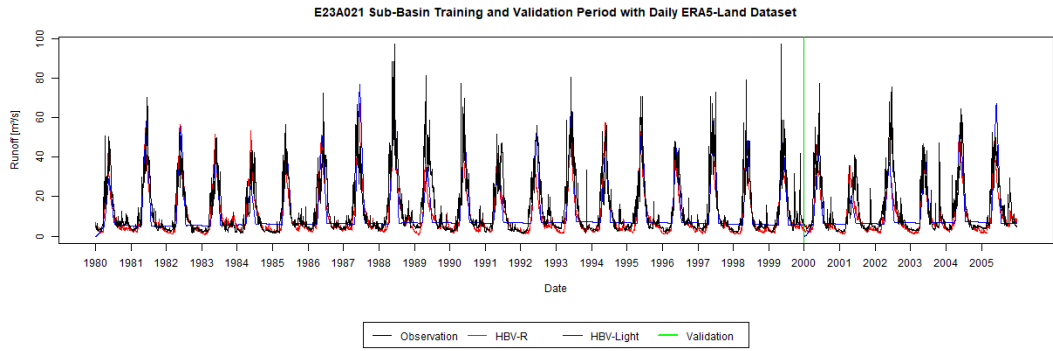


E23A016 Sub-Basin Training and Validation Period with Daily ERA5-Land Dataset

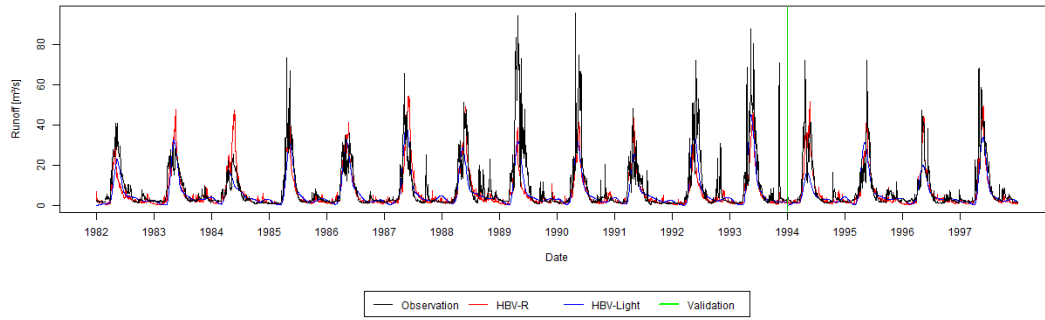


E23A020 Sub-Basin Training and Validation Period with Daily ERA5-Land Dataset

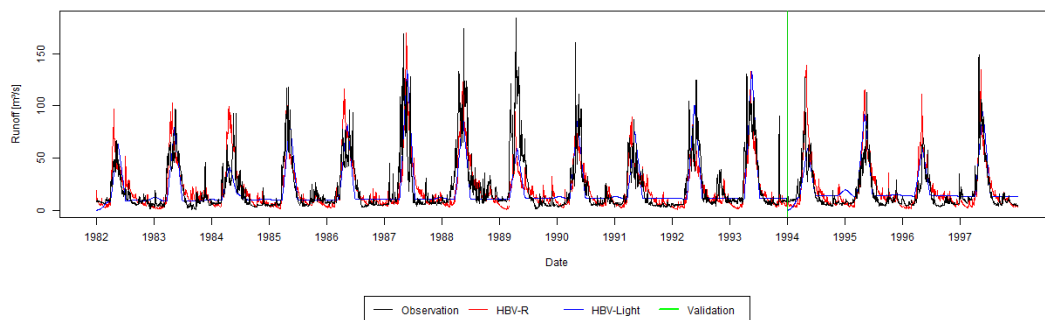




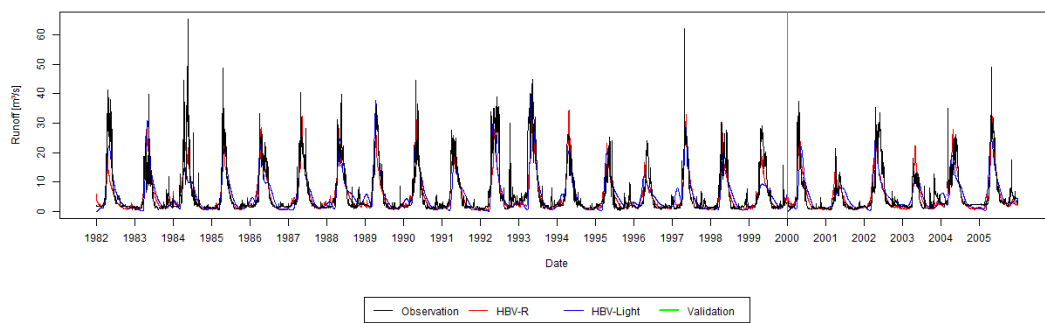
E23A026 Sub-Basin Training and Validation Period with Daily ERA5-Land Dataset



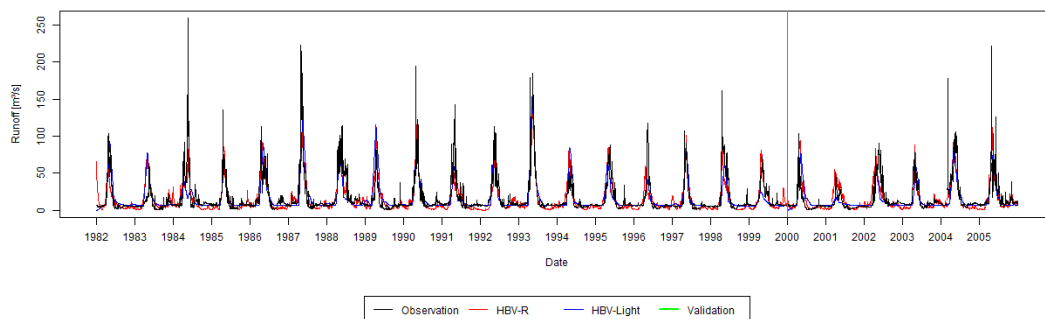
E23A027 Sub-Basin Training and Validation Period with Daily ERA5-Land Dataset



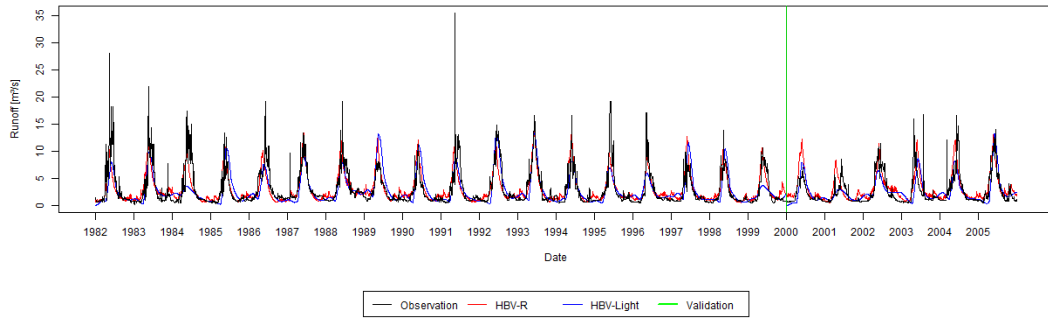
E23A028 Sub-Basin Training and Validation Period with Daily ERA5-Land Dataset



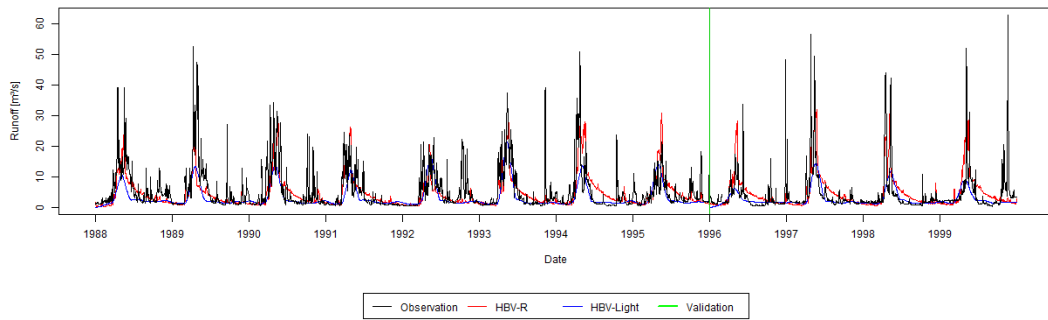
E23A029 Sub-Basin Training and Validation Period with Daily ERA5-Land Dataset



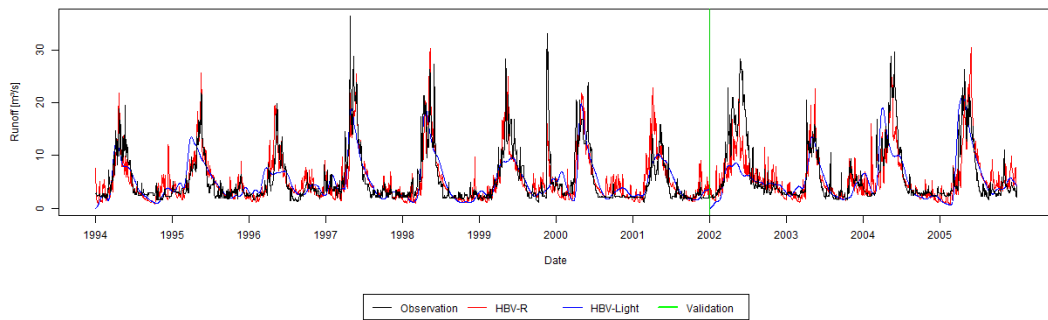
E23A030 Sub-Basin Training and Validation Period with Daily ERA5-Land Dataset



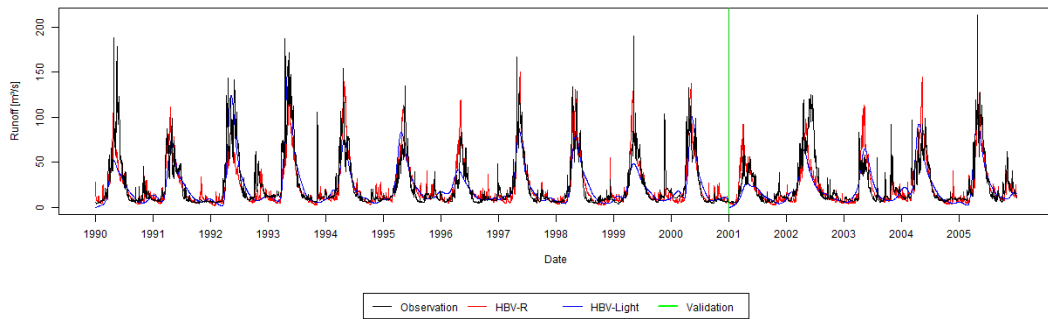
E23A031 Sub-Basin Training and Validation Period with Daily ERA5-Land Dataset



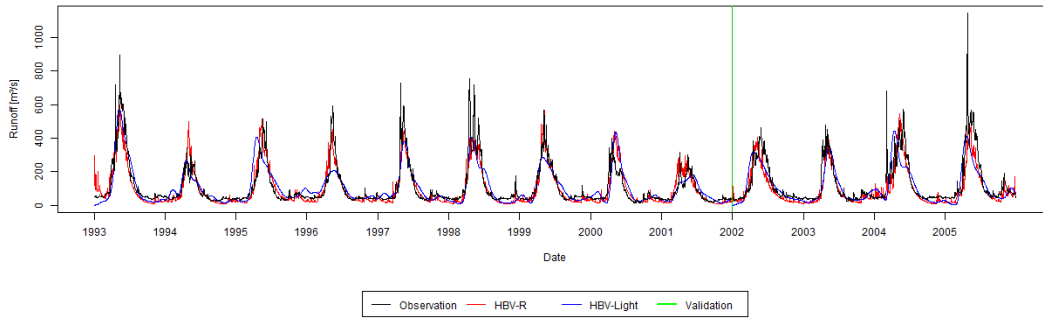
E23A033 Sub-Basin Training and Validation Period with Daily ERA5-Land Dataset



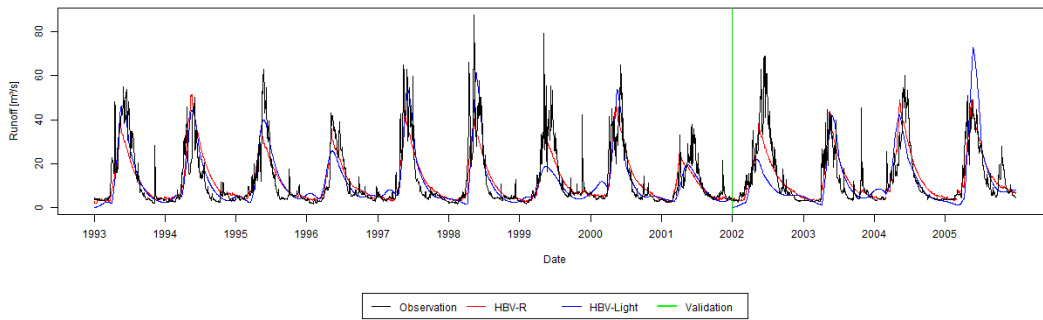
E23A034 Sub-Basin Training and Validation Period with Daily ERA5-Land Dataset



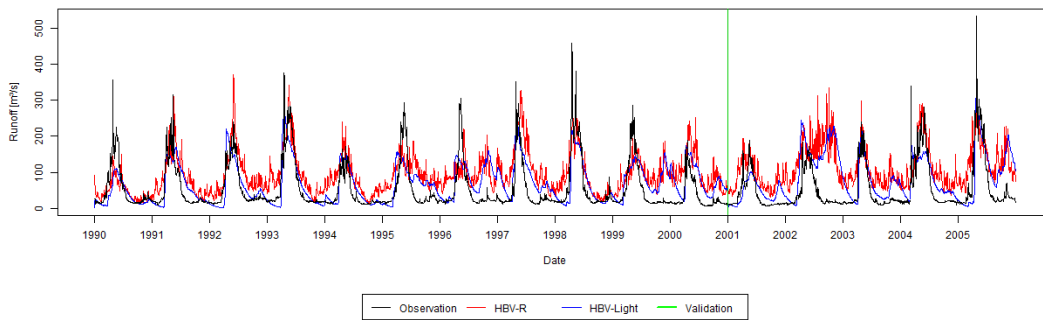
E23A035 Sub-Basin Training and Validation Period with Daily ERA5-Land Dataset



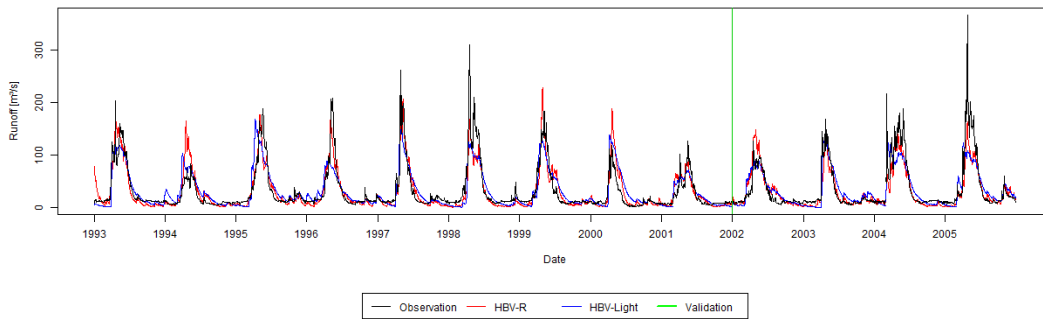
E23A036 Sub-Basin Training and Validation Period with Daily ERA5-Land Dataset

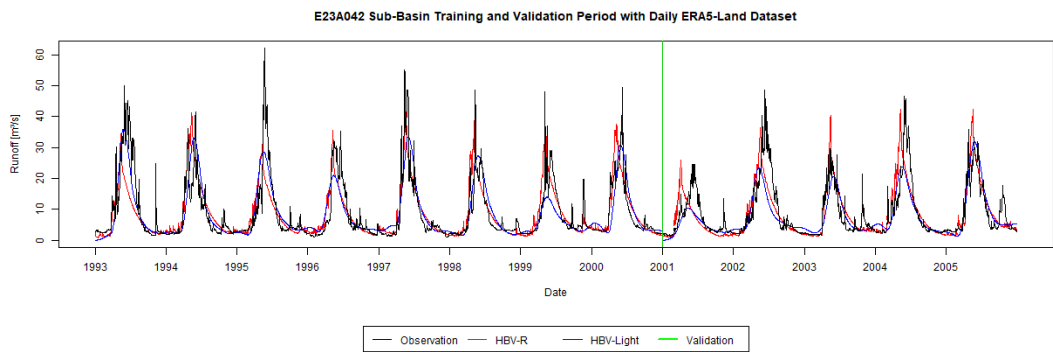
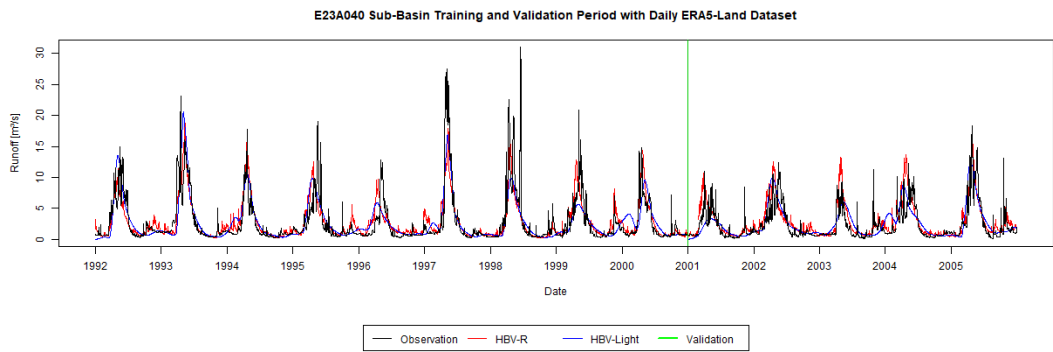
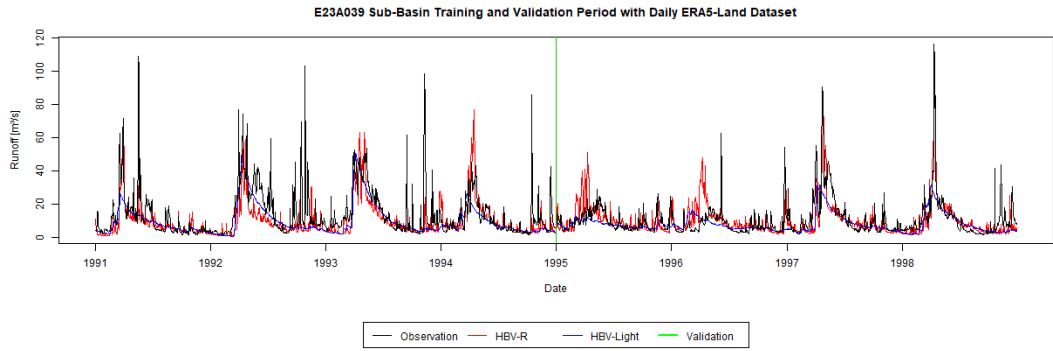


E23A037 Sub-Basin Training and Validation Period with Daily ERA5-Land Dataset

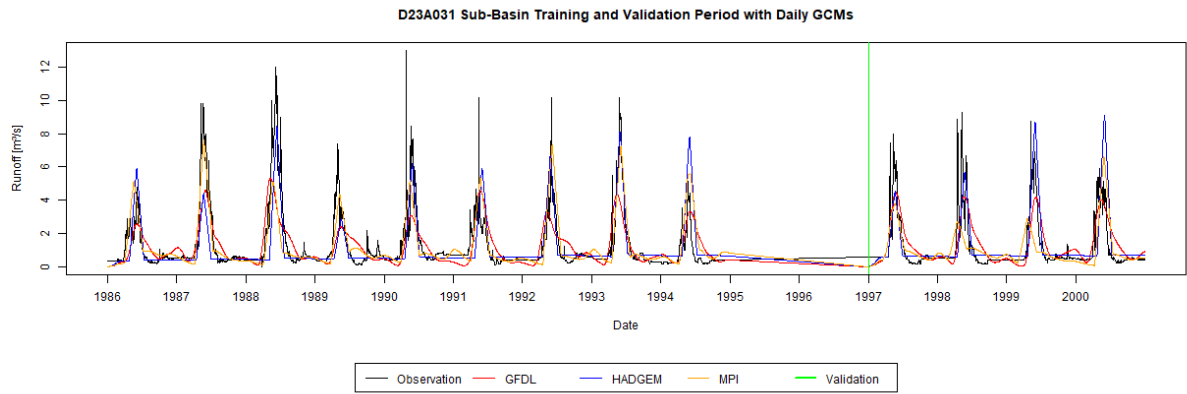
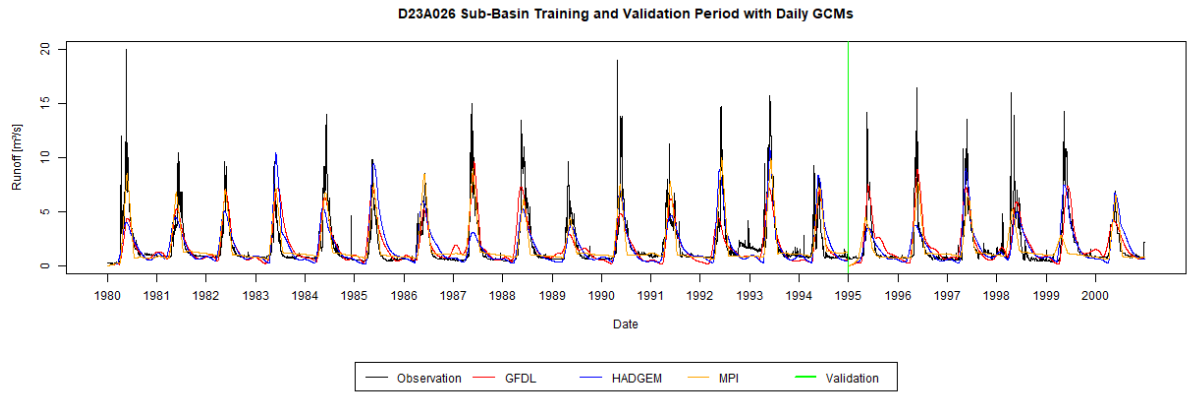
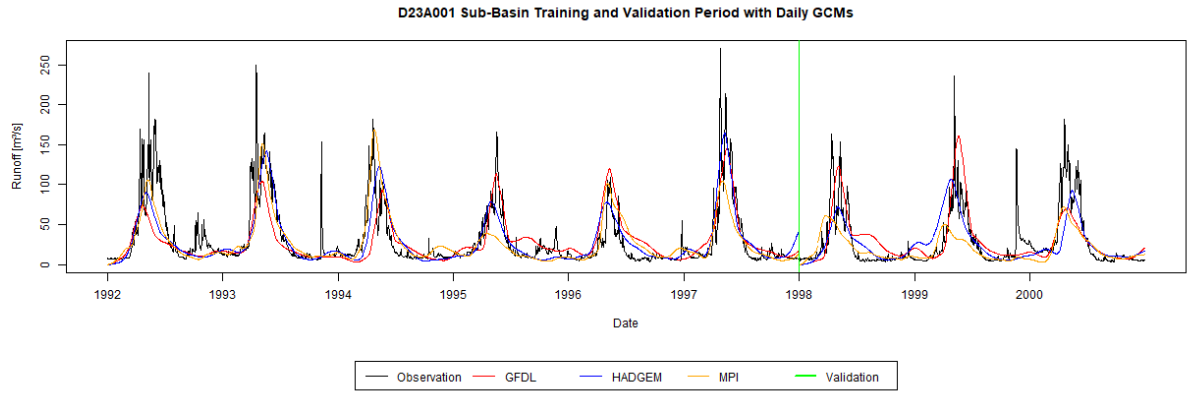


E23A038 Sub-Basin Training and Validation Period with Daily ERA5-Land Dataset

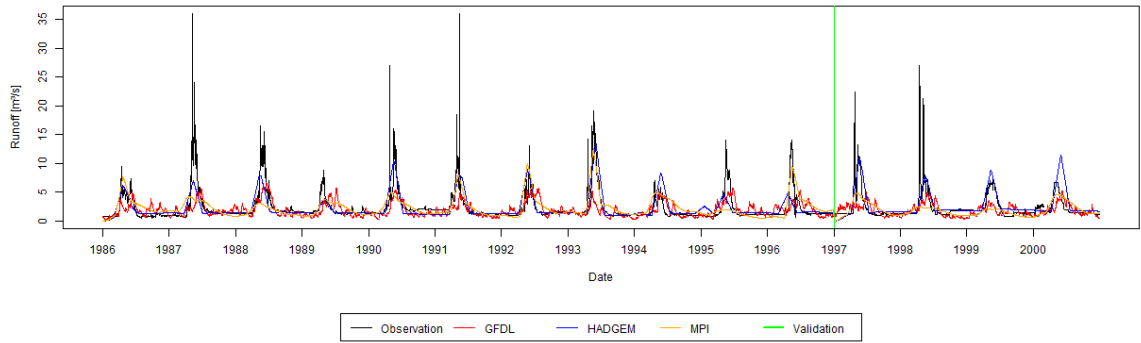




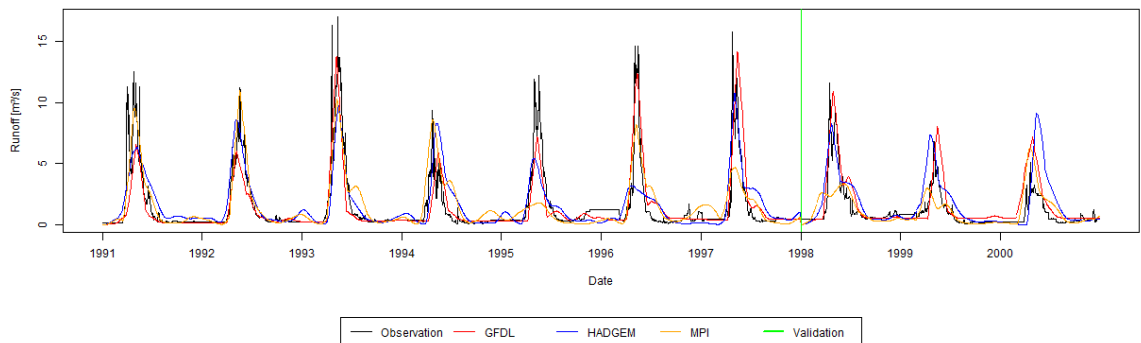
C. GCM Training and Validation



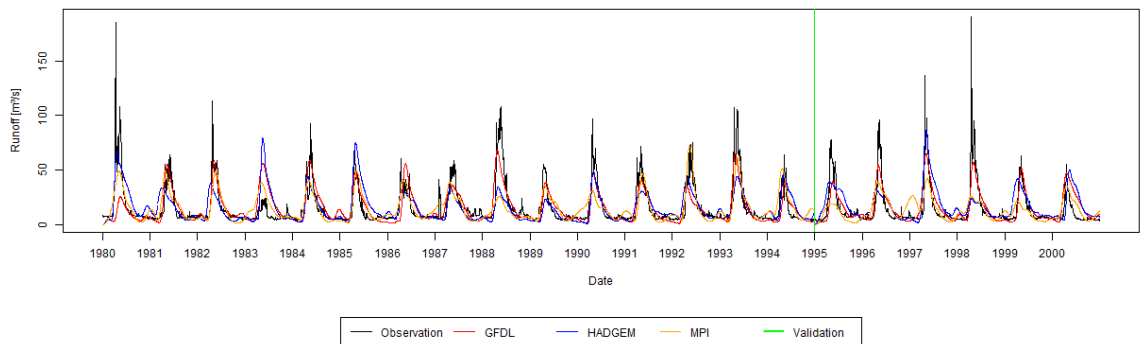
D23A032 Sub-Basin Training and Validation Period with Daily GCMs



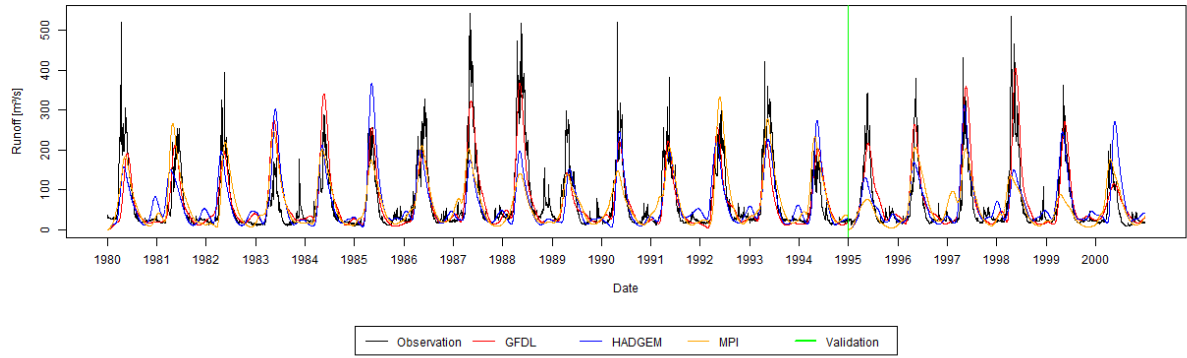
D23A037 Sub-Basin Training and Validation Period with Daily GCMs



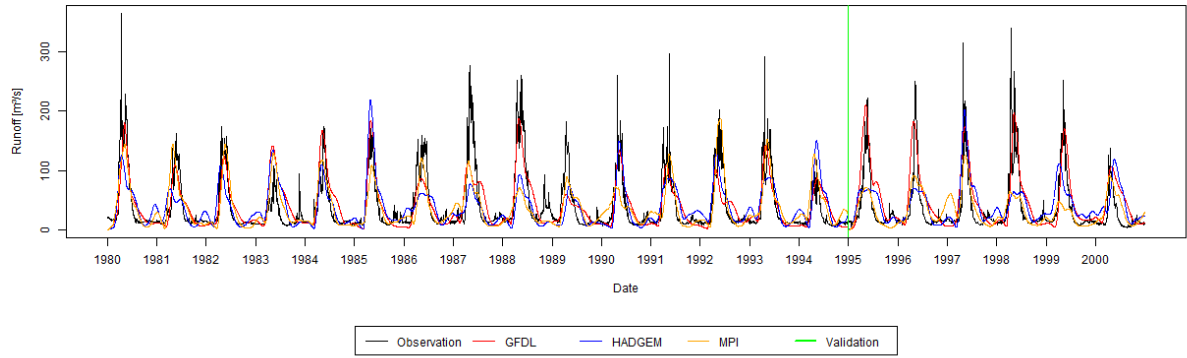
E23A004 Sub-Basin Training and Validation Period with Daily GCMs



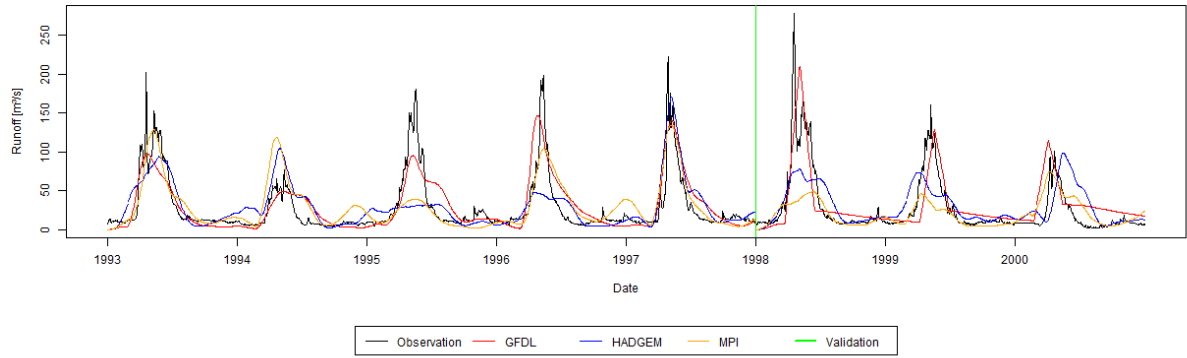
E23A005 Sub-Basin Training and Validation Period with Daily GCMs



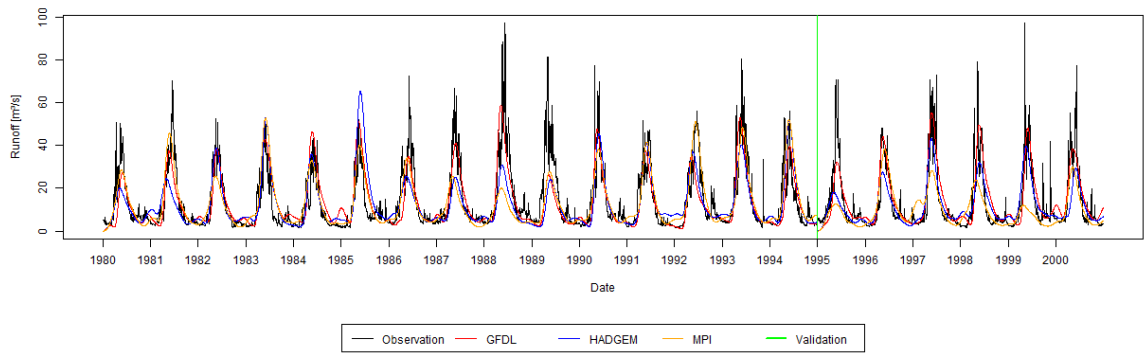
E23A016 Sub-Basin Training and Validation Period with Daily GCMs



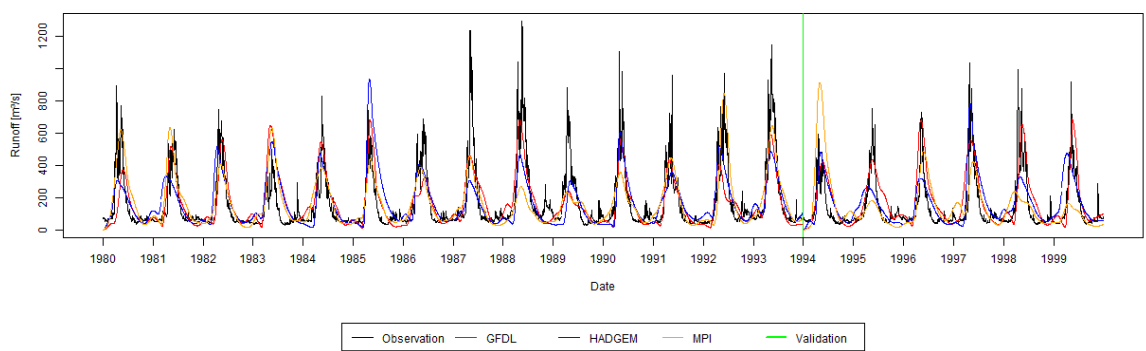
E23A020 Sub-Basin Training and Validation Period with Daily GCMs



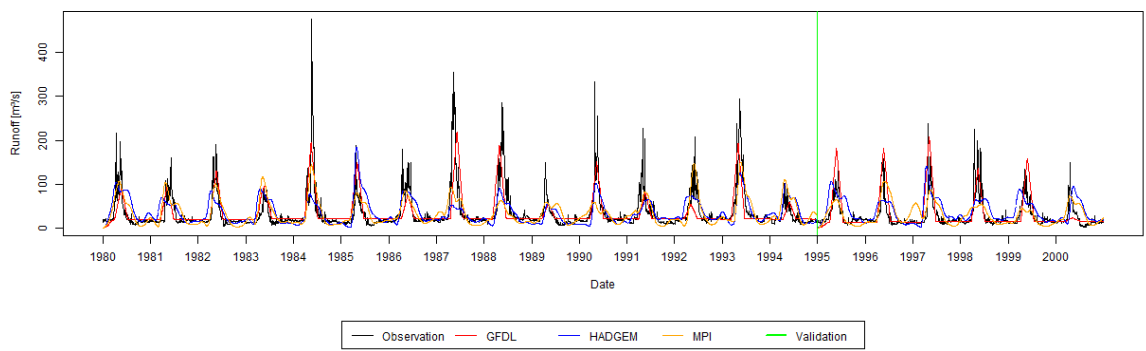
E23A021 Sub-Basin Training and Validation Period with Daily GCMs



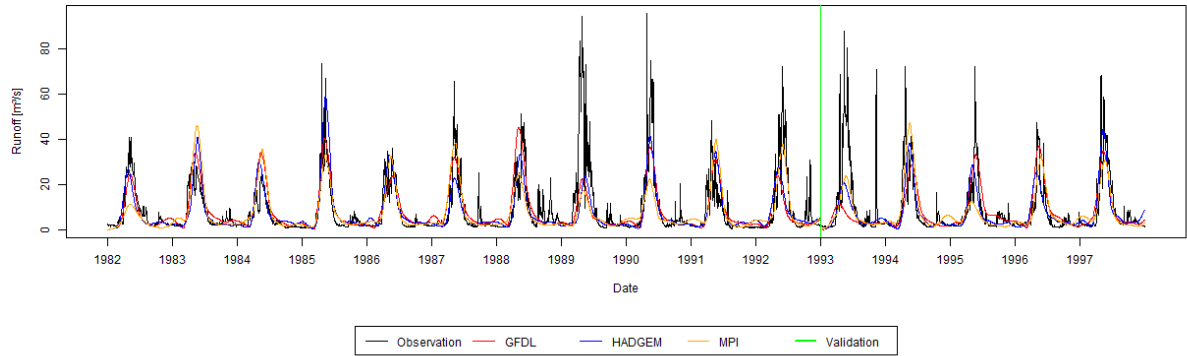
E23A022 Sub-Basin Training and Validation Period with Daily GCMs



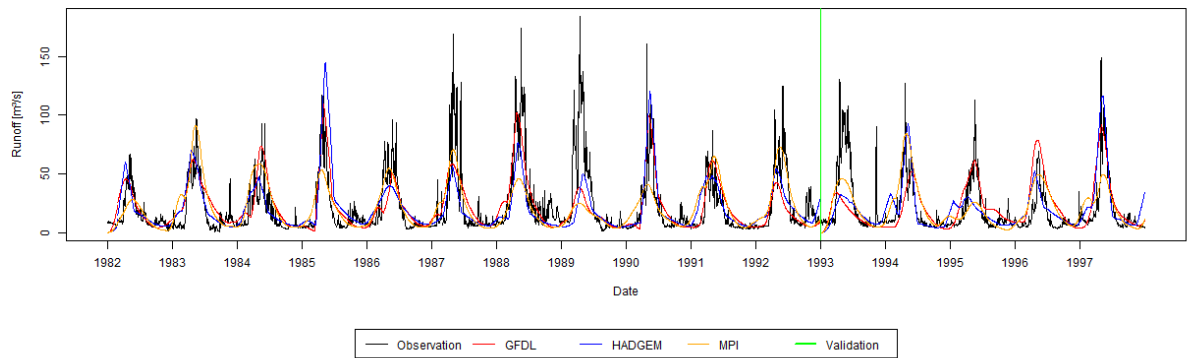
E23A023 Sub-Basin Training and Validation Period with Daily GCMs



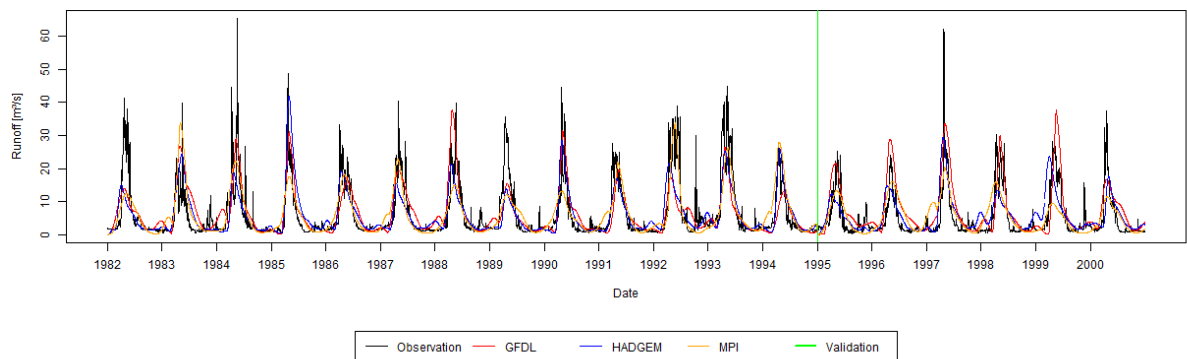
E23A026 Sub-Basin Training and Validation Period with Daily GCMs



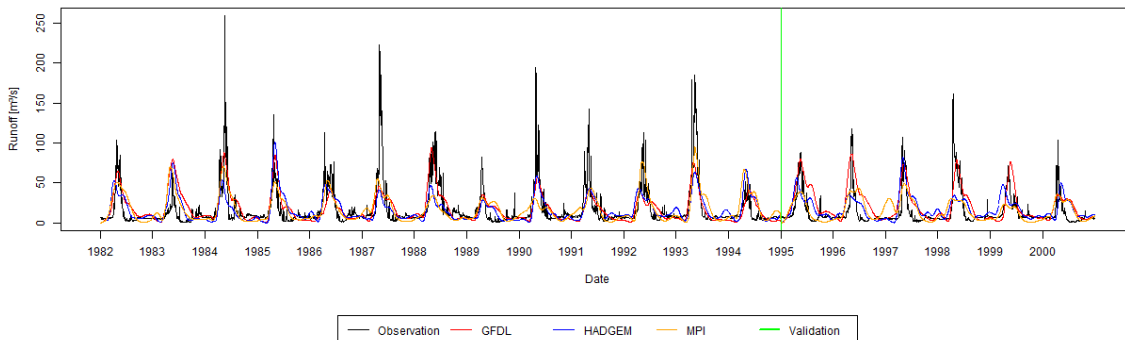
E23A027 Sub-Basin Training and Validation Period with Daily GCMs



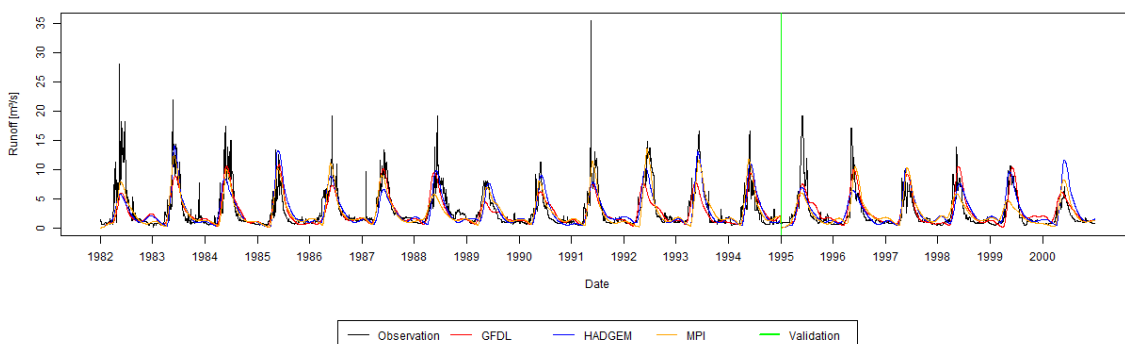
E23A028 Sub-Basin Training and Validation Period with Daily GCMs



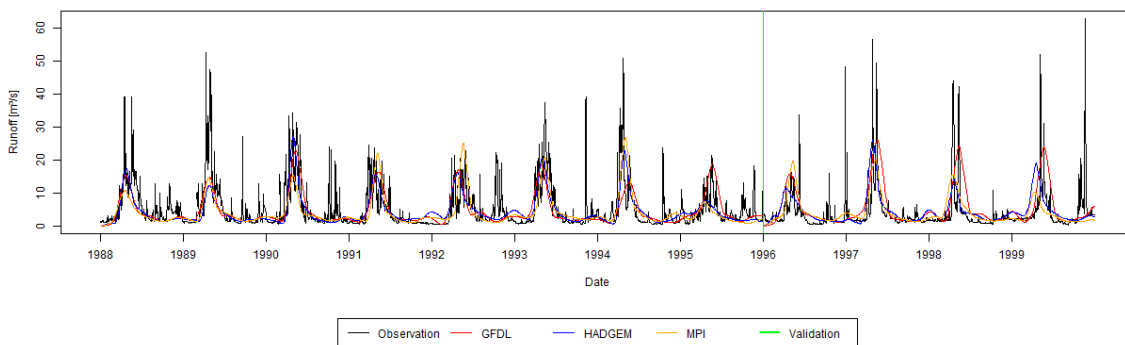
E23A029 Sub-Basin Training and Validation Period with Daily GCMs



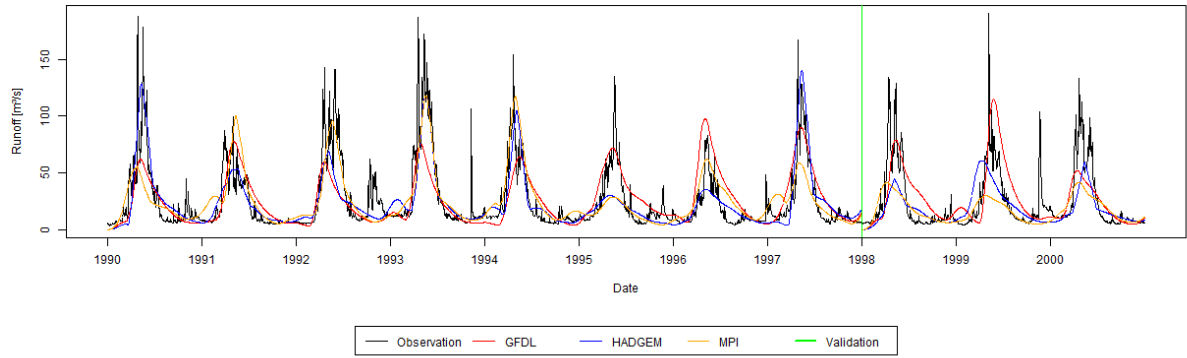
E23A030 Sub-Basin Training and Validation Period with Daily GCMs



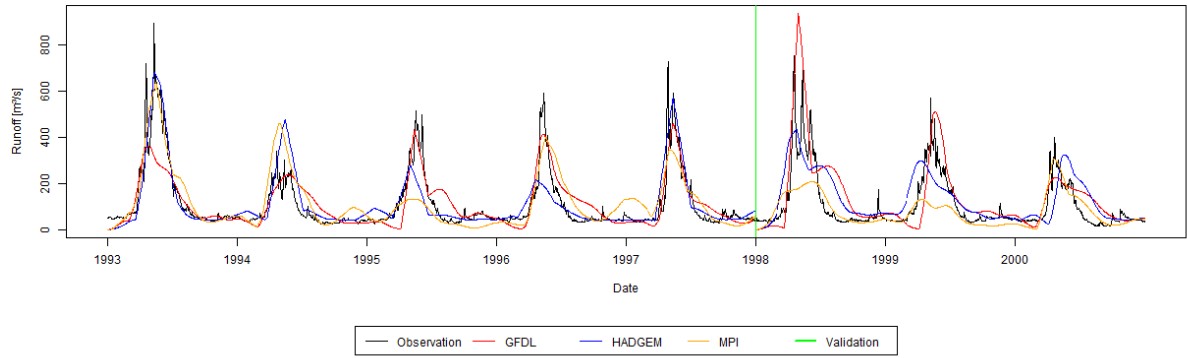
E23A031 Sub-Basin Training and Validation Period with Daily GCMs



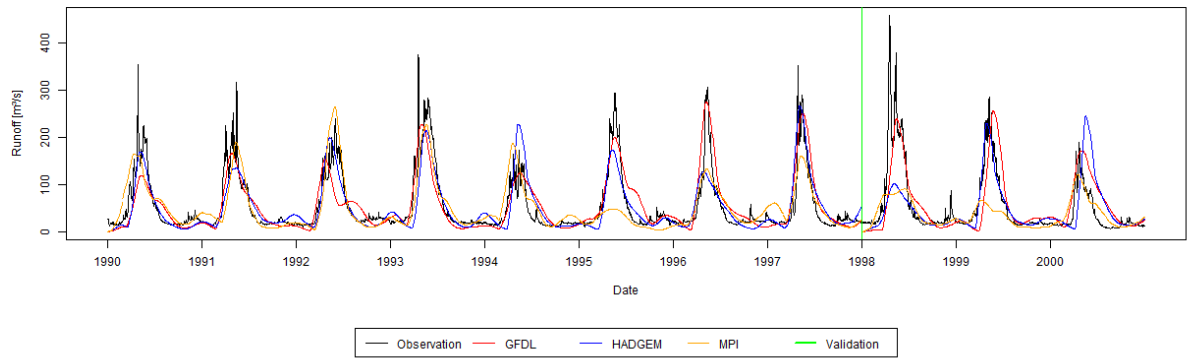
E23A034 Sub-Basin Training and Validation Period with Daily GCMs



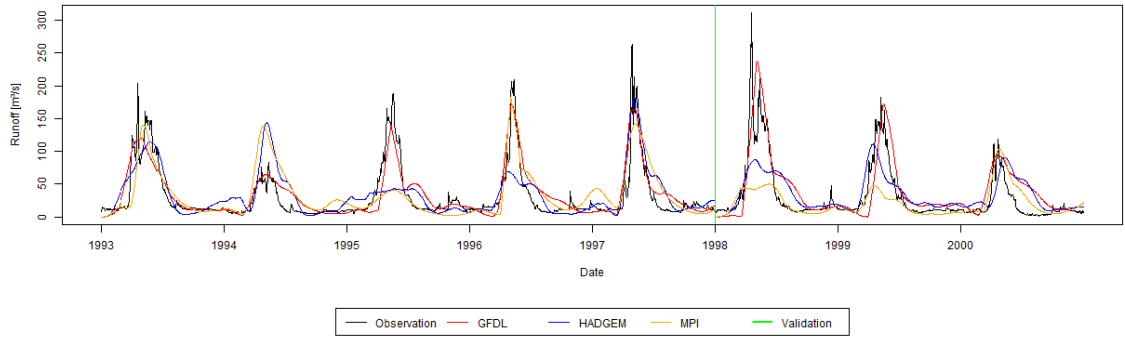
E23A035 Sub-Basin Training and Validation Period with Daily GCMs



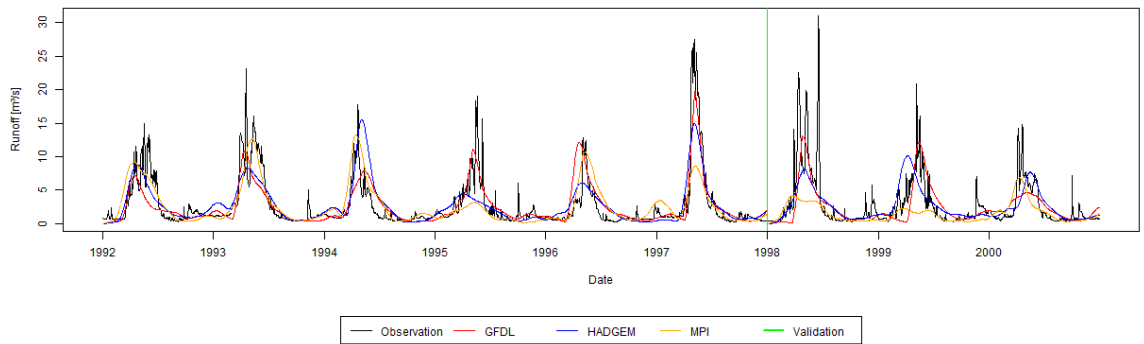
E23A037 Sub-Basin Training and Validation Period with Daily GCMs



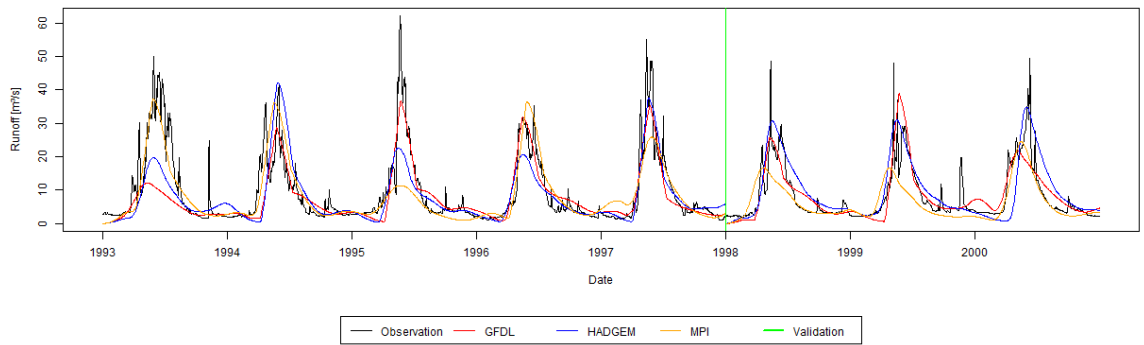
E23A038 Sub-Basin Training and Validation Period with Daily GCMs



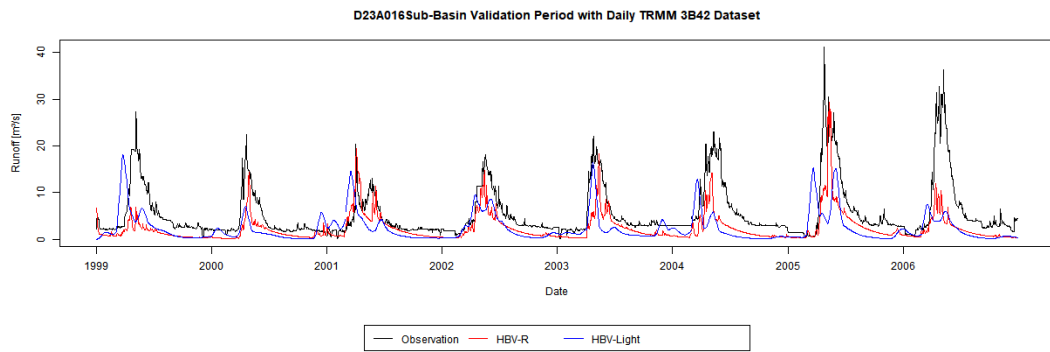
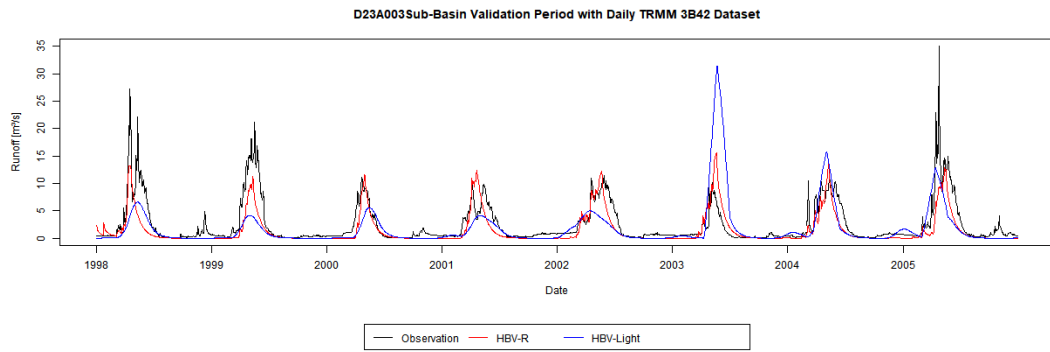
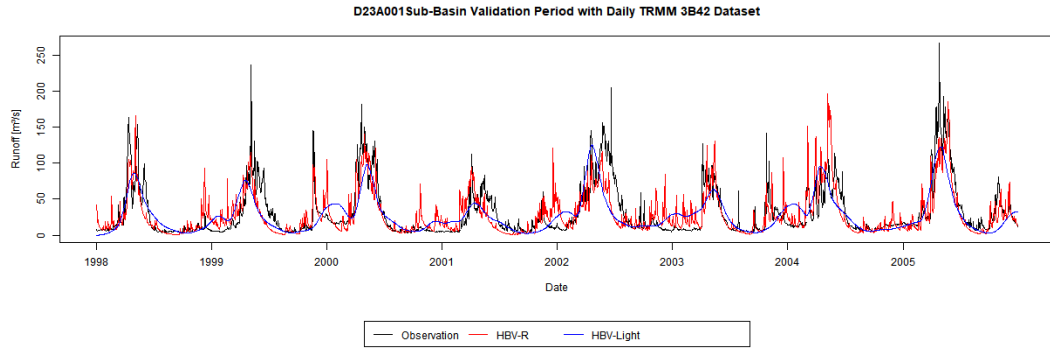
E23A040 Sub-Basin Training and Validation Period with Daily GCMs



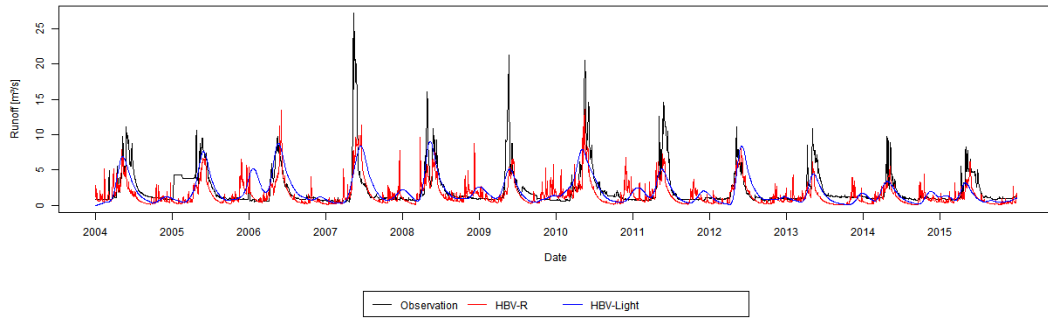
E23A042 Sub-Basin Training and Validation Period with Daily GCMs



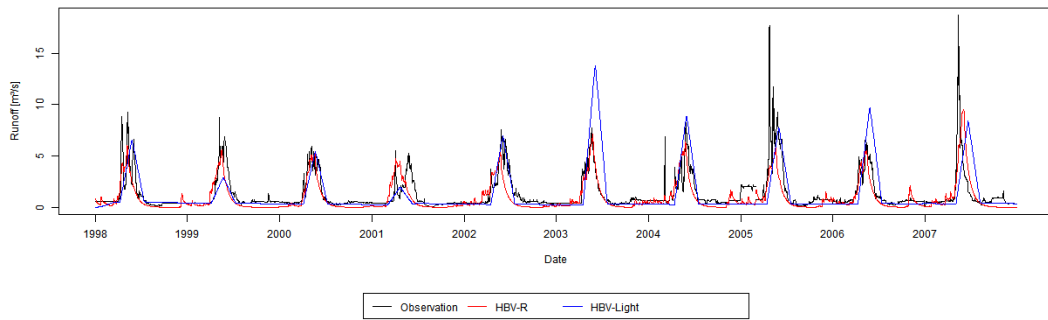
D. TRMM 3B42 Validation



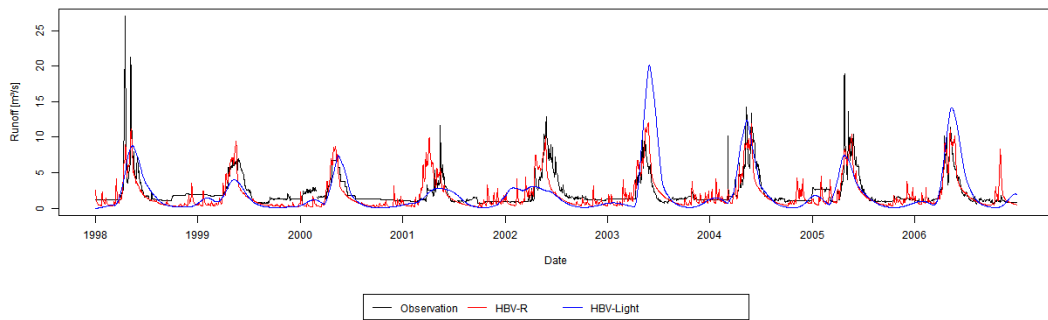
D23A026Sub-Basin Validation Period with Daily TRMM 3B42 Dataset



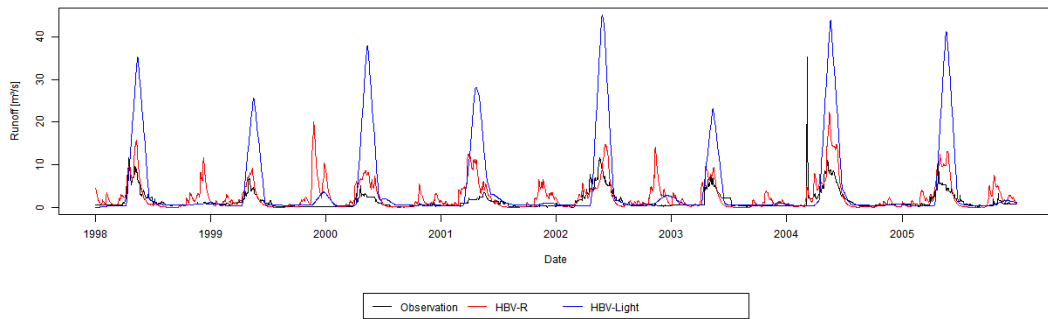
D23A031Sub-Basin Validation Period with Daily TRMM 3B42 Dataset

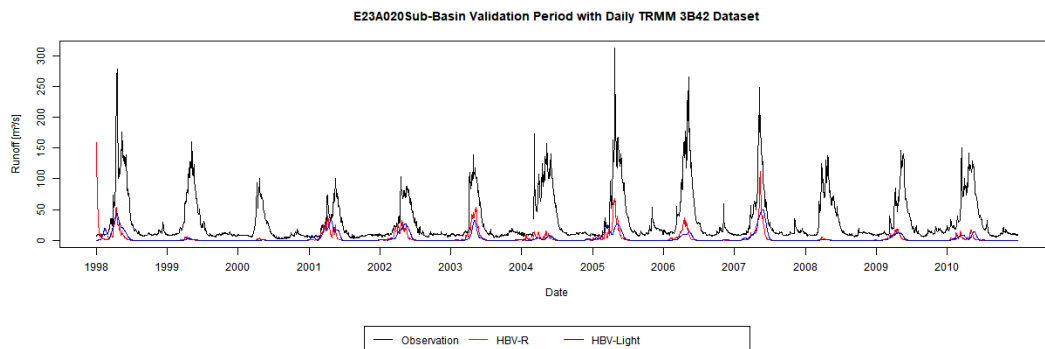
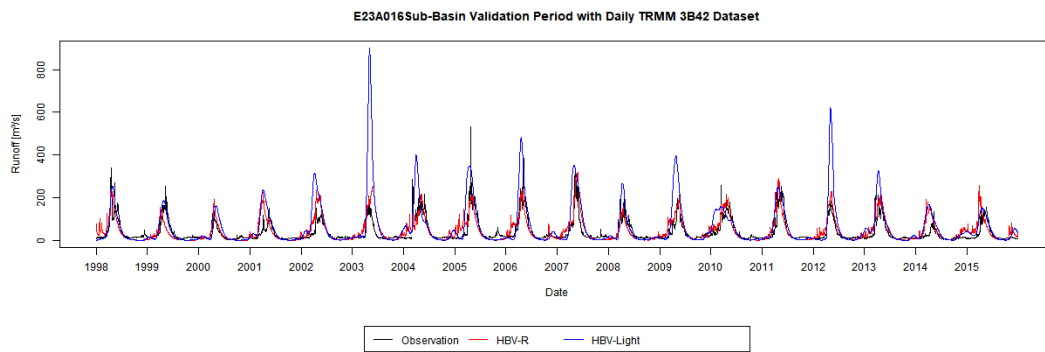
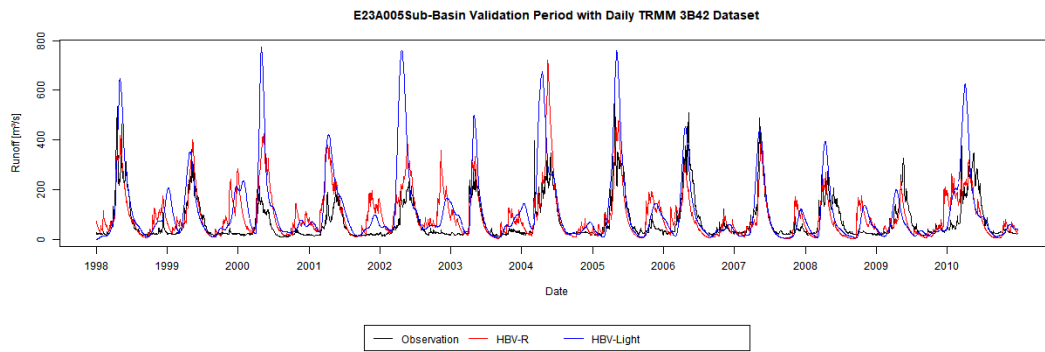
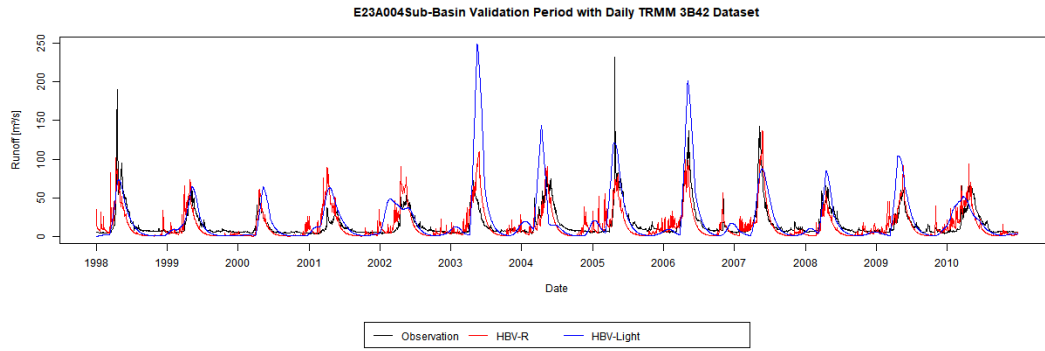


D23A032Sub-Basin Validation Period with Daily TRMM 3B42 Dataset

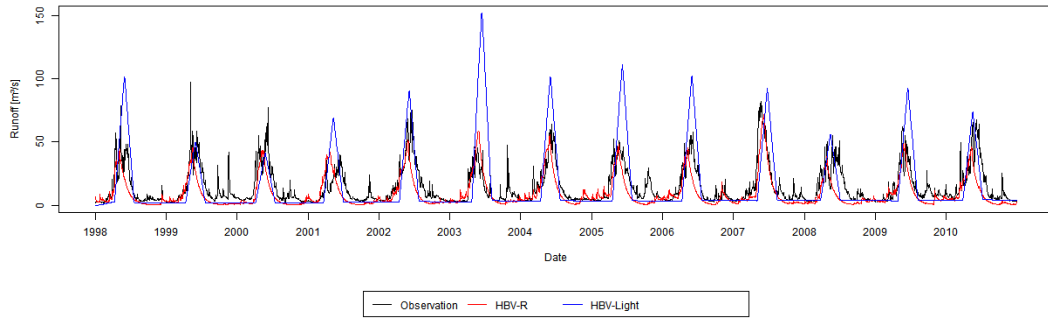


D23A037Sub-Basin Validation Period with Daily TRMM 3B42 Dataset

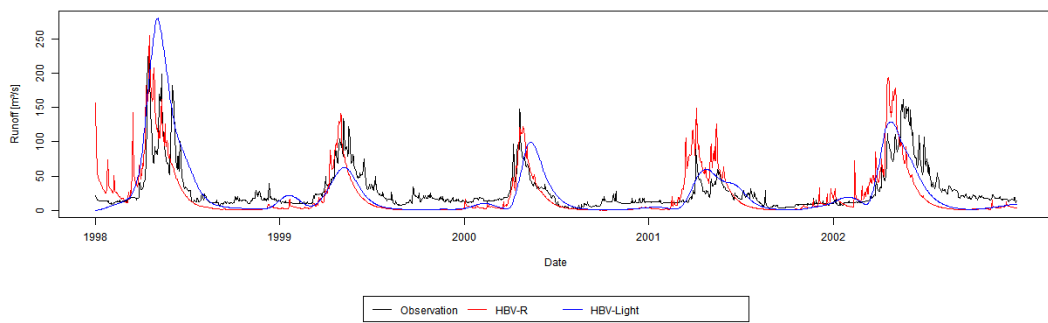




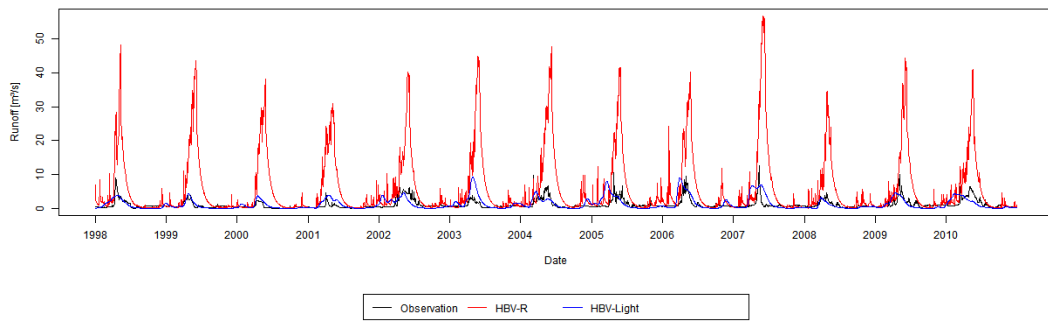
E23A021Sub-Basin Validation Period with Daily TRMM 3B42 Dataset



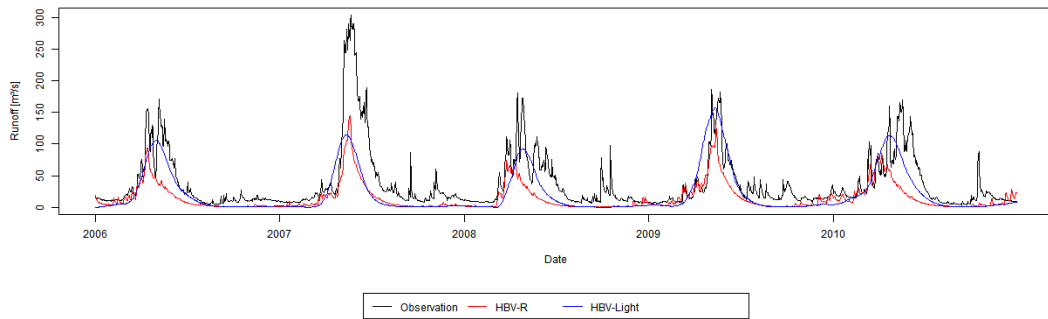
E23A023Sub-Basin Validation Period with Daily TRMM 3B42 Dataset



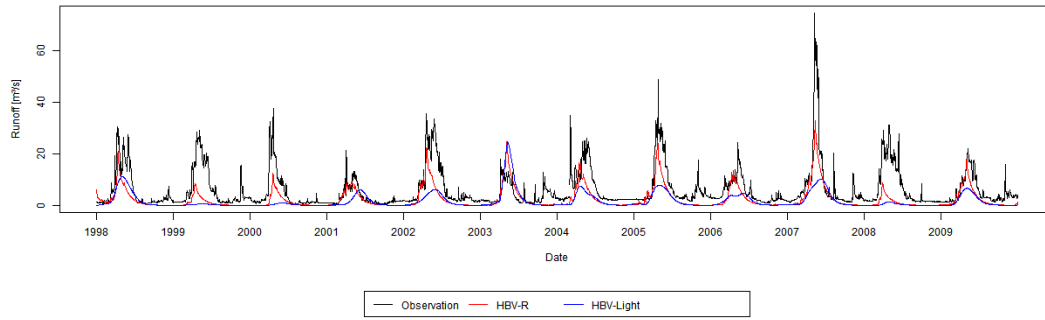
E23A026Sub-Basin Validation Period with Daily TRMM 3B42 Dataset



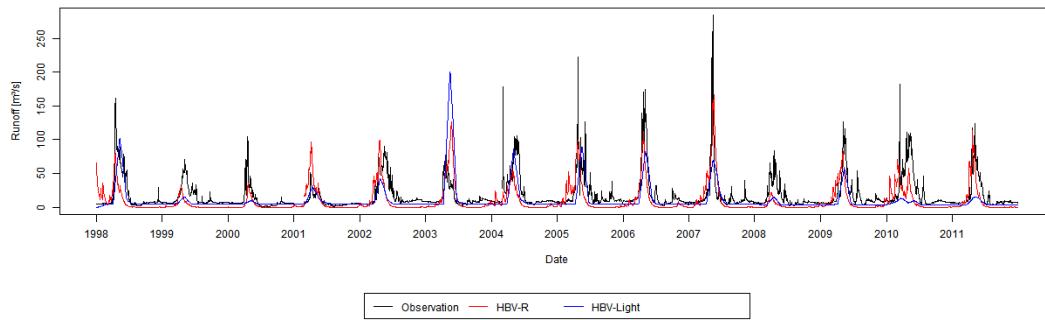
E23A027Sub-Basin Validation Period with Daily TRMM 3B42 Dataset



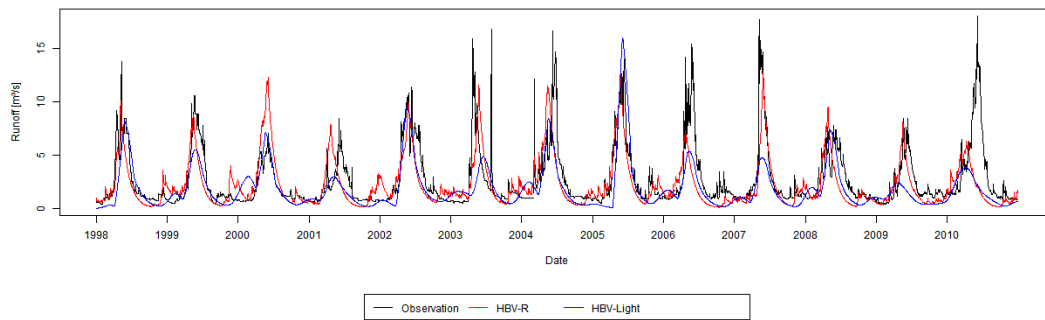
E23A028Sub-Basin Validation Period with Daily TRMM 3B42 Dataset



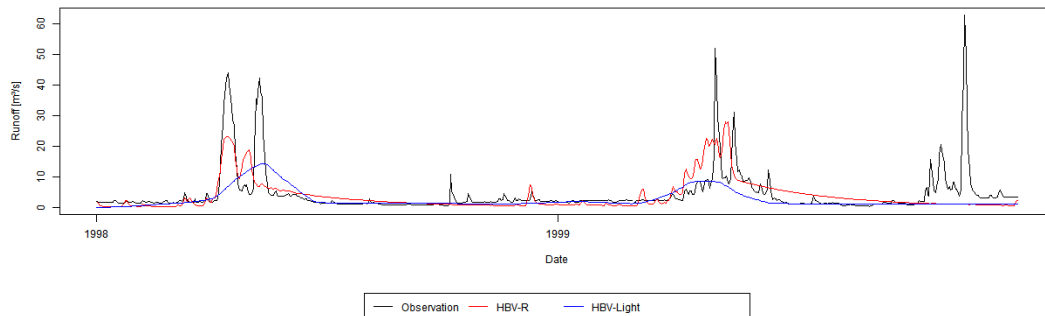
E23A029Sub-Basin Validation Period with Daily TRMM 3B42 Dataset



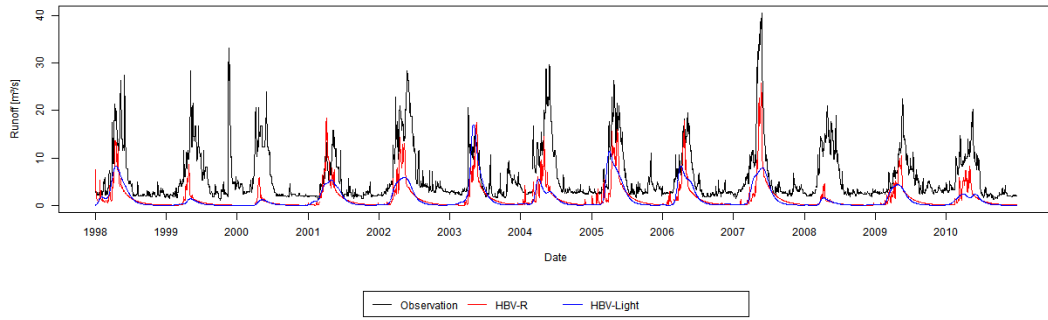
E23A030Sub-Basin Validation Period with Daily TRMM 3B42 Dataset



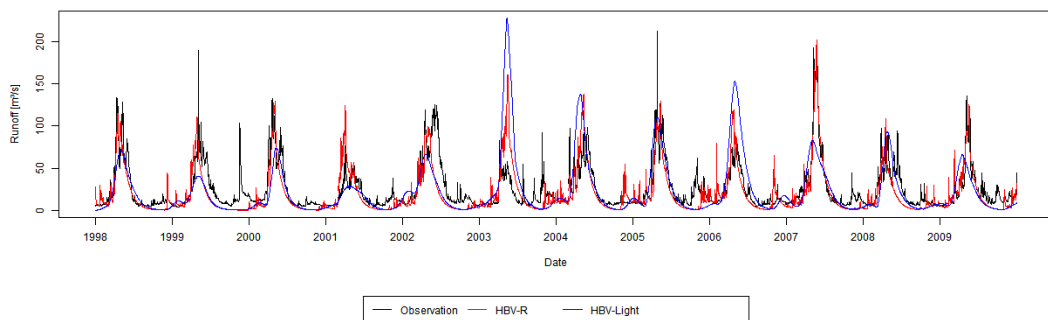
E23A031Sub-Basin Validation Period with Daily TRMM 3B42 Dataset



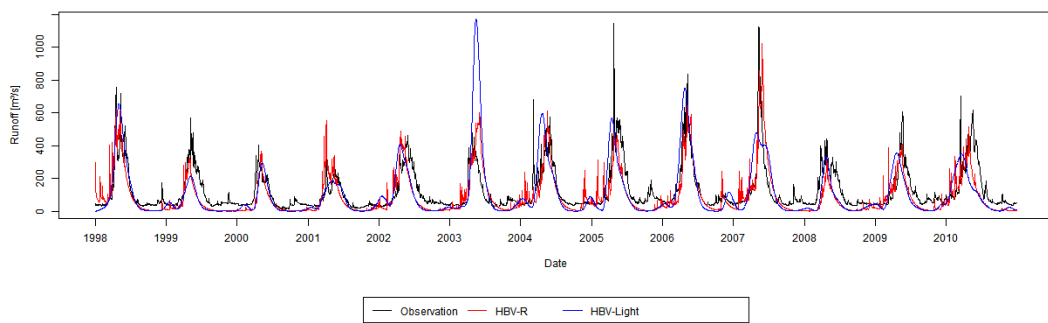
E23A033Sub-Basin Validation Period with Daily TRMM 3B42 Dataset



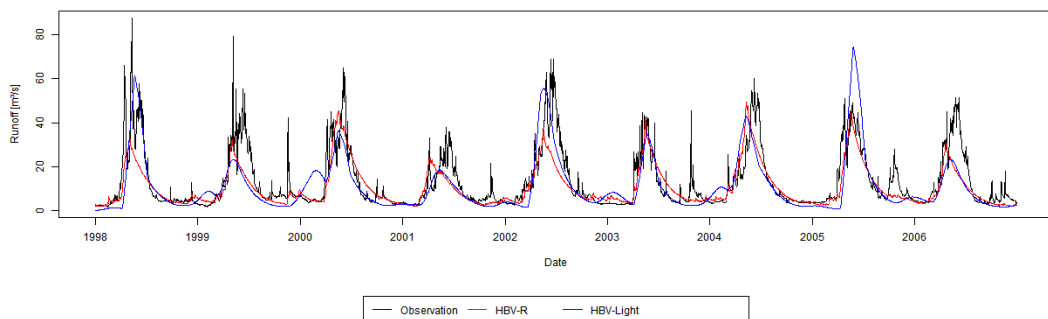
E23A034Sub-Basin Validation Period with Daily TRMM 3B42 Dataset



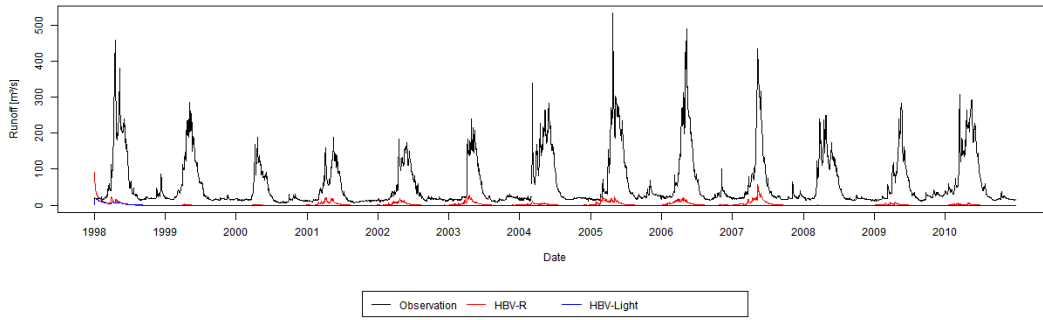
E23A035Sub-Basin Validation Period with Daily TRMM 3B42 Dataset



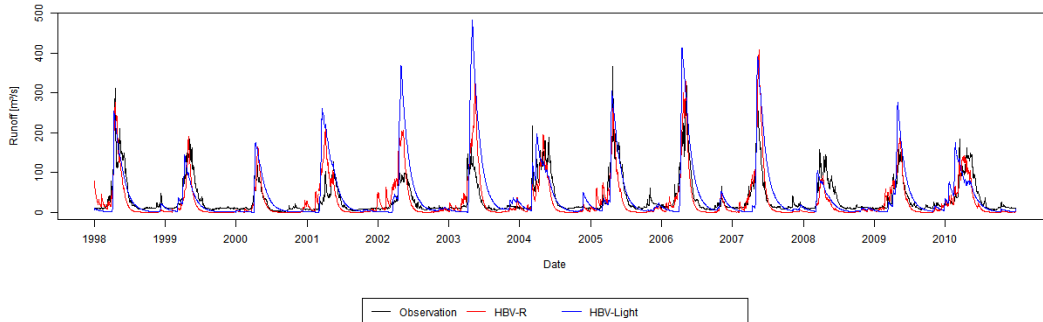
E23A036Sub-Basin Validation Period with Daily TRMM 3B42 Dataset



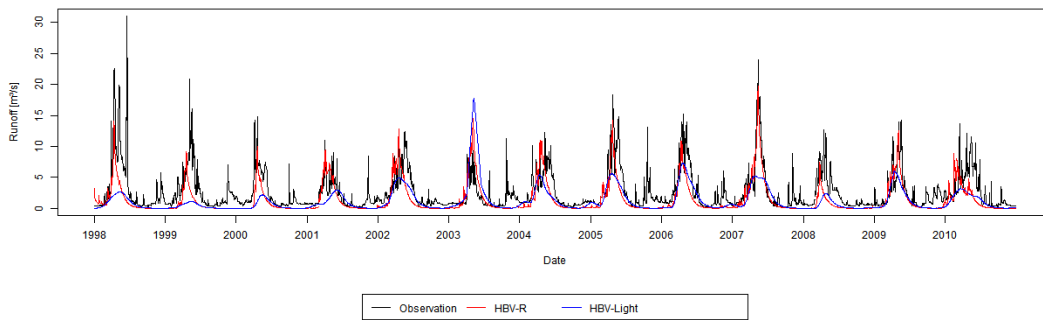
E23A037 Sub-Basin Validation Period with Daily TRMM 3B42 Dataset



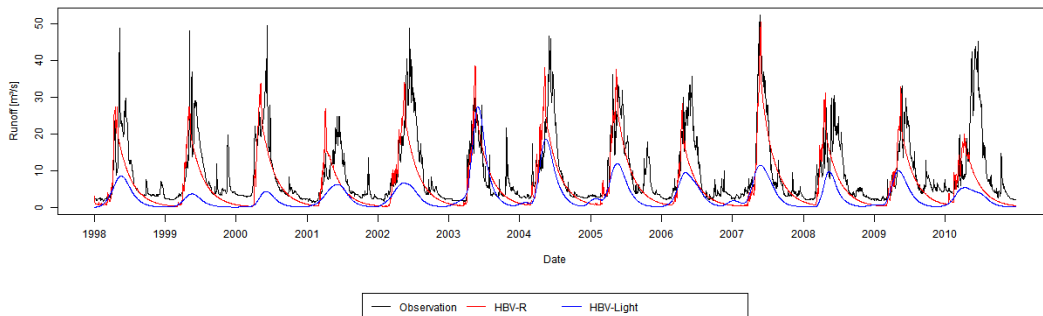
E23A038 Sub-Basin Validation Period with Daily TRMM 3B42 Dataset



E23A040 Sub-Basin Validation Period with Daily TRMM 3B42 Dataset



E23A042 Sub-Basin Validation Period with Daily TRMM 3B42 Dataset



E. GCM Annual Future Graphs

